Master’s Degree in Mechanical Engineering

Master’s Thesis

Finite Element Analysis of the DTT Cryostat Thermal Shield Support System: Structural Assessment of Support Configurations

Supervisor:

Prof. Giorgio Zavarise

Co-Supervisors:

Prof. Roberto Bonifetto

Prof. Giulio Ventura

Candidate:

Mohammad Bagheri 302098

A.Y. 2025-2026

Abstract

This thesis presents a finite element assessment of support configurations for the Divertor Tokamak Test (DTT) cryostat thermal shield system. The study focuses on the global structural response of the cylindrical, dome, and top-cover thermal shields and their G10-CR support members under gravity loading, prescribed thermal loading, and combined gravity and thermal loading. The cryostat body and thermal shields were represented using shell elements, while the support members were represented using beam elements. Bonded, joint-based, and no-separation interface definitions were adopted to represent the main load-transfer and displacement-compatibility conditions of the support system. The insulation gap between the cryostat body and the thermal shields was assessed by comparing initial and deformed gap-result fields.

A geometry-informed reference configuration with 80 support members of 20 mm diameter was first analyzed. The support layout was derived from the available CAD-based support paths and refined through iterative finite element assessment, rather than by assuming a uniformly spaced support distribution. The results showed that gravity loading governed the support-member combined stresses, while thermal loading mainly influenced the overall deformation field. The maximum support-member combined stress occurred under combined gravity and thermal loading, with a value of 236.49 MPa. The maximum shell stress occurred in the dome thermal shield under gravity loading, with a value of 99.496 MPa. These values were below the selected reference strength values adopted for the stress comparison. The vertical deformation in gravity loading remained below the 10 mm deformation check for all thermal shield regions. The gap assessment did not indicate a critical reduction of insulation clearance. The first relevant positive eigenvalue buckling multiplier of the gravity-prestressed reference configuration was 5.2172, corresponding to an estimated total buckling load state of approximately 6.22 times the reference gravity load under the nonlinear-based perturbation interpretation. Supplementary thermal-perturbation checks also indicated that thermal-induced elastic buckling was not close to the operating condition.

A mixed-diameter support configuration was then evaluated as a sensitivity case. In this configuration, 15 support members were kept at 20 mm diameter and 65 support members were reduced to 10 mm diameter, reducing the total support-member cross-sectional area by 60.94%. The mixed-diameter configuration produced deformation, support-member combined-stress, gap,

and buckling results comparable to those of the reference configuration. Within the analyzed loading cases and the assumptions of the global shell-and-beam model, the mixed-diameter configuration can therefore be considered a structurally promising alternative for further detailed assessment.

Keywords: DTT, cryostat thermal shield, finite element analysis, support system, G10-CR, shell elements, beam elements, thermal contraction, insulation gap, eigenvalue buckling

Acknowledgements

I would like to express my sincere gratitude to my supervisor, Professor Giorgio Zavarise, for his guidance, support, and valuable academic advice throughout the development of this thesis. His expertise and feedback were essential in shaping the direction of the work and improving its technical quality.

I am also grateful to my co-supervisors, Prof. Roberto Bonifetto and Prof. Giulio Ventura for their support, comments, and contributions during the thesis work.

I am also sincerely thankful to Professor Mauro Corrado for his valuable help, suggestions, and technical discussions, which contributed significantly to the progress of this work.

I would like to give special thanks to Danilo Acquesta Nunes, PhD candidate, for his continuous and thorough mentoring during this project. His careful explanations, detailed feedback, and constant availability were extremely helpful in the development of the finite element model and the interpretation of the results.

Finally, I would like to thank my family and friends for their continuous support, patience, and encouragement throughout my studies.

Contents

List of Tables

List of Figures

Chapter 1

Introduction

1.1 General Background

Magnetically confined fusion seeks to produce sustainable power by heating a deuterium–tritium plasma to several hundred million kelvins [1]. To confine this plasma, large superconducting coils, maintained at cryogenic temperature within the cryostat, generate the strong magnetic fields required for plasma confinement [2]. The vacuum vessel, first wall, and divertor, located close to the plasma, reach several hundred degrees Celsius during operation and baking. The coexistence of hot plasma-facing components and cryogenic superconducting systems within the same tokamak assembly creates large thermal gradients and strong differential-expansion constraints on intermediate structures.

A thermal shield is installed between hot components and the cold superconducting coils to intercept most of the radiative heat load before it reaches the cryogenic systems. It is cooled by helium gas circulating at 70–100 K and composed of stainless steel panels with welded cooling tubes and reflective coatings to lower emissivity. In general, thermal shield supports must withstand mechanical loads associated with gravity, thermal contraction, seismic events, and electromagnetic transients, while minimizing heat conduction to the cold mass [3], [4].

In large fusion devices such as ITER, KSTAR, EAST, JT-60SA, and Wendelstein 7-X, thermal shield design studies have addressed panel segmentation, cooling layout, material selection, and support attachment strategies [5–7]. These studies show that the support system is a critical design feature because it governs load transfer, displacement compatibility, and solid conduction paths.

The Divertor Tokamak Test (DTT) facility, currently under design in Italy, investigates advanced power-exhaust solutions for future DEMO-class reactors [8]. Its cryostat and magnet system adopt a thermal shield architecture comparable in function to those used in large superconducting tokamaks such as ITER, while being adapted to the size, layout, and loading conditions of DTT. In DTT, the thermal shield is located between warm structures, such as the vacuum vessel, ports, and cryostat, and the superconducting magnets operating at approximately 4.5 K. It is divided into three main subassemblies: the Vacuum Vessel Thermal Shield (VVTS), the Port Thermal Shield (PTS), and the Cryostat Thermal Shield (CTS), each subjected to different thermal and geometric boundary conditions. The system operates with the vacuum vessel reaching up to 110 °C during baking, while the thermal shields operate at 80–110 K [3]. The vacuum vessel encloses the plasma region and represents one of the main warm boundaries for the thermal shield system. The cryostat forms the external vacuum boundary of the system, enclosing the superconducting magnets and thermal shields.

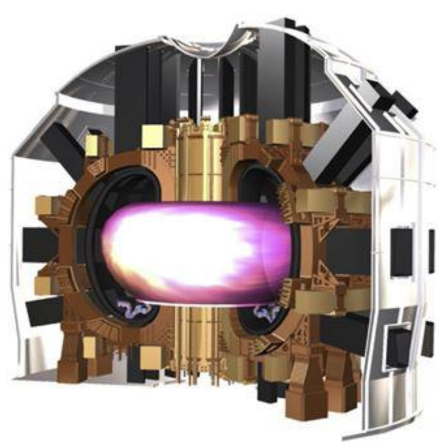

Figure 1.1 Sectional view of DTT facility [8].

The DTT thermal shields are composed of modular stainless steel panels with integrated cooling tubes and toroidal segmentation. The panels are connected to surrounding structures through insulated support interfaces, whose arrangement affects the load-transfer mechanism, displacement compatibility, and thermal-bridge area of the shield system [3], [9].

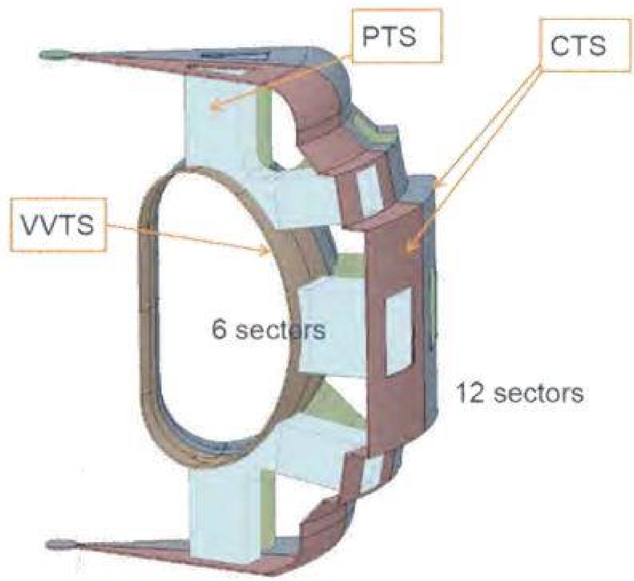

Figure 1.2 Schematic view of the DTT thermal shields [10].

Since DTT is still in its engineering-design phase, the number, geometry, and arrangement of the supports require structural assessment because they directly affect the stiffness, deformation pattern, and clearance control of the shield system. Within this broader context, the present work focuses specifically on the cryostat thermal shield support system. Other thermal shield components, such as the vacuum vessel and port shields, are not included in the present analysis.

1.2 Objectives and Motivation

The mechanical assessment of thermal shield supports in superconducting fusion devices requires a balance between stiffness, load-carrying capacity, and thermal-contraction accommodation. The support system must carry the shield weight, preserve the insulation gap, and allow relative displacement between the cryostat and the cooled shield without causing excessive stress or deformation.

Previous studies on superconducting fusion devices show that thermal shield support systems are strongly influenced by support geometry, material selection, kinematic constraints, and local load-transfer conditions. In particular, reducing the support cross-section may decrease the available thermal-bridge area, but it can also increase stress and deformation. Therefore, the structural effect of support configuration changes must be assessed before such modifications can be considered acceptable.

The present work is limited to a global structural assessment of the cryostat thermal shield support system and does not attempt to provide a detailed local verification of bolted attachments or complete thermal design. Instead, it develops a global finite element model to evaluate the structural response of the shield system under gravity loading, prescribed thermal loading, and combined gravity and thermal loading. The prescribed temperature fields are used to represent the structural effect of differential thermal contraction, without performing a separate heat-transfer analysis. In addition to the reference support configuration, a mixed-diameter configuration is considered to examine the structural consequence of reducing selected support-member diameters.

The specific objectives of the thesis are:

1. To develop a finite element model of the DTT cryostat thermal shield support system, including shell representations of the cryostat and thermal shields and beam representations of the support members.
2. To define support-interface conditions using contact and joint constraints to represent the main load-transfer and displacement-compatibility features of the support system.
3. To evaluate the deformation, shell stress, support-member stress, and insulation-gap response under gravity, prescribed thermal, and combined loading cases.
4. To perform a preliminary linear eigenvalue buckling assessment of the reference configuration, including the gravity-prestressed case and supplementary thermal-perturbation checks.
5. To compare a reference support configuration with a mixed-diameter configuration in order to assess the structural effect of reducing selected support-member diameters.

The results provide a global structural assessment of the analyzed support configurations within the assumptions of the finite element model. They also identify the main governing response quantities and the limitations that should be addressed in future detailed design and verification work.

1.3 Thesis Structure and Scope

The thesis is organized into five chapters.

Chapter 1 introduces the general background of magnetic-confinement fusion and the role of thermal shields in superconducting tokamaks. The motivation, objectives, and scope of the present work are defined with reference to the DTT cryostat thermal shield support system.

Chapter 2 reviews previous work on thermal shield design and support systems in major superconducting fusion devices, including ITER, DEMO, JT-60SA, EAST, KSTAR, Wendelstein 7-X, and DTT. The review focuses on support conduction, kinematic constraint strategies, local stress concentration, temperature-dependent material behavior, manufacturing tolerance effects, and secondary design drivers such as electromagnetic isolation and assembly feasibility.

Chapter 3 describes the finite element methodology adopted in this work. It presents the geometrical idealization, material definitions, element types, support-interface modeling strategy, boundary conditions, loading cases, meshing strategy, insulation-gap assessment procedure, structural assessment quantities, and eigenvalue buckling approach.

Chapter 4 presents the finite element results for the reference and mixed-diameter support configurations. The reference configuration is evaluated under gravity loading, prescribed thermal loading, and combined gravity and thermal loading. The chapter also presents the insulation-gap assessment, eigenvalue buckling results, and the sensitivity assessment of the mixed-diameter configuration.

Chapter 5 summarizes the main conclusions of the work and outlines possible future developments. The limitations of the modeling approach are discussed, including the global beam-and-shell idealization, the absence of detailed attachment modeling, the simplified G10-CR material representation, and the use of prescribed temperature fields.

The scope of the thesis is limited to the global structural assessment of the DTT cryostat thermal shield support system. The analyses are performed under static structural conditions with prescribed temperature fields. Detailed heat-transfer analysis, transient thermal response, electromagnetic loading, seismic loading, fatigue, irradiation effects, manufacturing deviations, and detailed local verification of support attachments are outside the scope of the present model.

Chapter 2

State of the Art

The design of thermal shield support systems is a critical aspect of superconducting fusion devices because the supports influence both the structural reliability of the shield and the conductive paths toward the cryogenic system. Thermal shield supports must carry mechanical loads, accommodate differential thermal contraction, preserve clearances, and limit heat transfer through solid connections. These requirements are strongly coupled, because increasing support stiffness or support count can improve mechanical stability but may also increase the available conductive cross-section.

This chapter reviews previous experimental and numerical studies concerning thermal shields and support systems in major fusion devices, including ITER, DEMO, JT-60SA, EAST, KSTAR, Wendelstein 7-X, and DTT. The review is used to identify the engineering issues that are most relevant to the present structural assessment of the DTT cryostat thermal shield support system.

The discussion is organized around six main topics: conduction minimization in supports, kinematic design and contact mechanics, local stress concentration and sub-modeling, temperature-dependent material behavior, manufacturing and tolerance effects, and secondary drivers such as electromagnetic isolation, assembly feasibility, and cryogenic efficiency. The purpose of the review is not to reproduce the complete design process of each machine, but to extract the support system principles that motivate the modeling choices and assessment quantities used in the following chapters.

2.1 Conduction Minimization in Supports

The transfer of heat through mechanical supports is one of the important sources of parasitic heat load in superconducting fusion devices. After radiative exchange is reduced by coatings or multilayer insulation, conduction through structural supports can become a major component of the steady heat flux toward cryogenic systems. The number of supports, their length, cross-sectional area, and the thermal conductivity of the materials used determine the total heat leak. The designs implemented in existing machines provide essential references for the assessment of the DTT thermal shield supports. In the present work, conductive heat transfer is not directly computed but is considered indirectly through the geometric characteristics of the support system.

In ITER, conduction was significantly reduced by replacing plate-type supports with axially oriented rods and by introducing G10 insulation blocks in the load path. The analyses were performed under steady thermal conditions with static load combinations representing dead weight, seismic, and electromagnetic cases. The articulated rods transmit only axial forces, allowing the metallic section to be minimized without bending. The insulation blocks interrupt both thermal and electrical continuity, thereby preventing eddy currents and limiting conductive heat flow. This configuration achieved an approximately five-fold reduction in conduction compared with the earlier plate design [4], [11], [12].

The DEMO studies demonstrate that conduction through gravity and structural supports dominates the thermal load to the 4 K magnets, even when radiation constitutes more than 80% of the total heat input at higher temperature levels. Increasing the operating temperature of the thermal shield slightly decreases radiative exchange but increases conduction more rapidly, leading to higher refrigeration power demand. These results confirm that reducing the number and cross-section of conductive paths is more effective than adjusting the shield temperature [13], [14]. These simulations were steady-state, combining analytical radiation estimates with FEM-based conduction models.

The actively cooled divertor of JT-60SA employs sliding attachments that allow differential movement and minimize clamping pressure on the bolts. This configuration limits the metallic contact area and consequently reduces parasitic conduction from the divertor target to the cooled structure [15]. Although not directly a thermal shield component, the same mechanical principle is applicable to cryogenic supports.

In EAST, multi-plate stainless steel supports insulated by 10 mm G10 layers and isolated bolts were adopted. The calculated conductive heat flow was approximately 326 W under the 300 K operating condition and remained nearly constant for higher vacuum-vessel baking temperatures, indicating that the insulation thickness and support number are the main variables controlling conduction [5], [16].

The KSTAR thermal shield uses epoxy–glass composite supports of fixed and sliding types to reduce conduction while allowing thermal contraction. Experimental results during the first cool-down revealed local temperature peaks of up to 160 K near zones of high support density. Uniform spatial distribution of supports is required to prevent localized heat accumulation [7].

In Wendelstein 7-X, Torlon polymer pins and cylinders, with a thermal conductivity of about 0.1 W m^{-1} K^{-1} at 70 K, are used as supports. Each support conducts approximately 0.2–0.5 W, and the cumulative effect of roughly 1400 supports results in an overall conduction of about 410 W. This outcome demonstrates that the total number of supports can be as influential as the material properties in determining the total conductive load [6].

For the DTT thermal shield system, analyses in the literature show that G10-CR fiberglass bolts constitute the principal thermal paths between the vacuum vessel and both the inner and outer shields. Their low conductivity and small diameter limit the heat transfer through each path, while the total number of bolts defines the overall conduction level. Previous ANSYS thermal analyses were performed in steady state to establish temperature distributions, while RELAP5-3D transient simulations resolved the helium coolant dynamics. The results also indicate that, once radiation is suppressed by surface coatings or multilayer insulation, conduction through these supports becomes the dominant source of cryogenic load. The same studies confirm that the careful selection of bolt geometry, spacing, and contact interfaces is important for maintaining the shield temperature within design limits [3], [10], [17]. In contrast, the present work isolates the cryostat thermal shield support system and evaluates its structural response independently.

The reviewed devices show that heat conduction through supports is commonly reduced by using low-conductivity materials such as G10 or Torlon, limiting metallic cross-section, and minimizing the number of conductive paths. For DTT, these findings suggest that the support configuration is an important factor in the thermal-shield performance, because the support members contribute to the available conductive paths between warm and cold structures. Reducing the conductive cross-section of well-insulated supports can reduce the available heat-transfer path, provided that deformation, stress levels, and gap preservation remain acceptable. Conduction control alone is not sufficient, because the support system must also accommodate thermal contraction without excessive restraint.

2.2 Kinematic Design and Contact Mechanics

Thermal shields are installed within narrow gaps between the vacuum vessel and the surrounding superconducting magnets. During operation and bake-out, large temperature differences between these structures cause differential thermal expansion and contraction, leading to relative movements that can reach several tens of millimeters. The support system must therefore allow controlled motion while maintaining the mechanical integrity of the shield and preserving clearance margins. Kinematic design principles are applied to avoid over-constraint and to minimize secondary stresses generated by restraint of thermal deformation. Contact mechanics considerations are therefore needed to evaluate whether the supports can accommodate these relative displacements without excessive local reactions, stress concentrations, or permanent deformation.

In the ITER design, the kinematic function of the supports is ensured by the combination of articulated rods and flexible strips. The outboard supports incorporate double spherical caps that provide rotation in two planes and transfer only axial forces, preventing bending in the rods during cool-down or electromagnetic transients. The spherical-cap system allows a swing of approximately three degrees, corresponding to about 48 mm of displacement, which satisfies the predicted thermal movement between the vacuum vessel and the magnets. During operation and thermal cycles, articulation must remain effective to avoid excessive stress at the interfaces. The inboard supports consist of prestressed Inconel 718 strips that follow the contour of the toroidal field coils and permit radial and toroidal motion while fixing the vertical load. This configuration maintains alignment while preventing excessive stress due to constrained expansion [4], [11], [12].

Experimental validation of this system confirmed that the assembly tolerances and tightening sequences did not impede the intended articulation of the supports. The 5 mm clearance at the cup interface ensured unrestricted rotation under the combined mechanical and thermal loads. The mechanical behavior observed in prototype testing verified the adequacy of the kinematic design in avoiding contact or interference between adjacent structures [18].

The KSTAR thermal shield adopts a different yet conceptually similar approach. Its support system combines fixed supports, which sustain gravitational loads, and sliding supports, which compensate for thermal contraction of the panels. The use of sliding supports prevents loss of preload and suppresses the build-up of bending stresses during cool-down. During operation, measured displacements of 6–12 mm confirmed that the sliding function performed as intended. The results indicate that precise control of friction and contact surface finish is necessary to ensure consistent sliding without stick–slip effects that could generate localized stress or noise [7].

In EAST, kinematic decoupling is achieved through the boundary conditions of the support system. The supports allow poloidal movement while restricting toroidal drift, thereby controlling the shield position while accommodating the differential expansion between the vessel and magnets. The self-centering behavior of the shield prevents cumulative misalignment during thermal cycling. The analysis also indicates that the combination of gravity and thermal loads is the main factor influencing deformation, whereas electromagnetic loading has a limited impact on kinematic response [5].

The Wendelstein 7-X thermal shield operates within extremely constrained geometric tolerances. The Torlon support pins and cylinders provide limited compliance but sufficient elasticity to absorb small differential displacements during thermal cycles. Although the kinematic freedom is less pronounced than in tokamaks, the design demonstrates that low-conductivity polymer supports can accommodate small motions without mechanical degradation [6].

The analyses conducted for DTT consider both thermal contraction and assembly deformation between the vacuum vessel and the two thermal shield layers. The finite-element evaluation represented steady equilibrium states at the two extreme temperature conditions (room temperature and cryogenic operation) to capture differential contraction effects. The bolted support system is modeled using beam elements and is classified into three categories of fixed, hinged, and non-hinged bolts, to reproduce the necessary degrees of freedom. Hinged and non-hinged bolts enable controlled sliding and rotation, ensuring that large differential movements are absorbed without overstressing the bolts. The calculated displacements reach up to 42 mm at the inner shield and 21 mm at the outer shield. Despite these large movements, the minimum gap between the structures remains greater than 8 mm, confirming that the intended clearances are maintained. The analysis further indicates that the bellows length of the vacuum vessel has a negligible effect on relative motion, confirming that the kinematic response of the shield is governed primarily by bolt configuration and contact stiffness [17].

The comparative evaluation of all machines shows that an effective kinematic design requires a controlled hierarchy of constraints: the directions needed for load carrying and positioning must be restrained, while other directions should provide sufficient freedom to accommodate thermal expansion or contraction. Articulated joints, sliding interfaces, and flexible elements have proven successful in eliminating bending loads and avoiding loss of preload. In the previous DTT studies, mixed-type bolts with controlled rotational and translational freedom were used to accommodate thermal movements and limit excessive stresses or contact between the vacuum vessel, shields, and magnets. The combination of mechanical stability and compliant motion established in these earlier machines provides the reference framework for the assessment of the DTT thermal shield support system. Even with proper kinematic freedom, local stress concentrations can arise at supports and joints. These effects are discussed in the following section.

2.3 Stress Concentration and Sub-Modeling Validation

The presence of complex geometries, such as bolted joints, welded cooling tubes, and support attachments, generates local stress concentrations that are not captured adequately by global finite-element (FE) models. Detailed sub-modeling is therefore required when the objective is to evaluate local stress fields and compare them with design-code limits. In the present thesis, this level of local verification is not performed because the model is intended for global support-system assessment. The literature shows that the main locations of stress concentration in thermal shields are at the supports, joints, and weld interfaces, where abrupt changes in stiffness and load direction occur. Understanding these local phenomena is crucial for defining reliable safety margins and fatigue life in the DTT design.

In ITER, several studies have addressed the importance of sub-modeling for the thermal shield supports. The final design verification presented in [19] demonstrates that the global stress values are within acceptable limits but that local peaks arise in the spherical bushings and bolted joints. The verification was based on static structural analysis using temperature fields derived from steady thermal simulations. The maximum stress in the outboard support reached approximately 959 MPa in the spherical bush, corresponding to a margin of about 22% below the allowable limit. The same analysis identifies the joints and fasteners as the most critical components, requiring local verification against fatigue and ratcheting. Earlier work in [20] and [12] reveals high stresses near weld brackets and port attachments, where combined membrane and bending stresses approach 240 MPa under the most severe load combinations. These regions were reinforced, and the welding sequences were optimized to mitigate local overstress.

The role of geometric accuracy on local stress fields is examined in [18]. This study introduces measured manufacturing deviations into the finite-element mesh and shows that such imperfections significantly modify the stress distribution at contact points and supports. The results confirm that design verification must include geometric uncertainties to avoid underestimating local stress levels.

In KSTAR, the structural integrity of the thermal shield supports and joints is discussed in [7]. The analysis indicates that the combined loading of gravity, cool-down shrinkage, and electromagnetic forces produces maximum stresses below the allowable limit of 380 MPa, with the highest local stresses occurring near support attachment welds and cooling-tube interfaces. The fabrication process was identified as a major influence on stress concentration; in particular, welding distortion was minimized by optimizing the assembly sequence and inspection methods.

The EAST machine exhibits similar behavior. As reported in [5], the maximum stress occurs at the junction between the vacuum-vessel and port thermal shields under the combined gravity, thermal, and electromagnetic loads. These results originate from static coupled thermal–structural simulations under steady operating conditions. The peak stress value of approximately 402 MPa remains within the allowable range, and additional rib reinforcement was introduced in these regions to control stress localization. The analysis also confirms that electromagnetic loads contribute less to local stress than thermal and mechanical effects, emphasizing the dominance of thermally induced deformation.

The Wendelstein 7-X design demonstrates the importance of material selection in controlling stress concentration. According to [6], replacing copper panels with brass significantly reduced eddy-current-induced stresses during fast magnet discharge. The maximum structural stress in the brass configuration remains below 100 MPa, well within the yield limit at 80 K. The study concludes that electrical isolation and the use of low-conductivity alloys are effective in limiting both electromagnetic and mechanical stress levels in shield components.

For the DTT configuration, the mechanical response of the supports, cooling pipes, and bolted joints has been evaluated in detail. The study in [17] identifies the bolts and cooling pipes as the most critical elements. The calculated stresses in the cooling pipes range from 150 to 260 MPa, while the bolts experience 108 to 183 MPa depending on the thermal scenario. Although these values remain below the allowable limits, they highlight the need for refined local modeling to capture the true stress distribution in areas where beam or shell elements are insufficient. The same study indicates that beam formulations can represent the global stiffness and load transfer of the support system, but they do not account for the detailed local stress field at contact interfaces.

The reviewed studies show that sub-modeling is important for obtaining accurate local stress predictions near supports, joints, and attachment regions. Global analyses define the overall deformation pattern and load transfer, while local solid models provide the necessary resolution for evaluating peak stresses, fatigue usage, and contact pressures. For the DTT design, detailed sub-models should be applied to the bolts, cooling-tube welds, and support attachment regions to ensure that design limits are respected under relevant thermal and mechanical load conditions, while electromagnetic effects may also be considered in comprehensive design analyses. This approach would support a more detailed verification of local structural integrity and fatigue margins within the narrow tolerances required for cryogenic operation.

2.4 Temperature-Dependent Material Behavior

The thermal shield operates across wide temperature gradients, ranging from several hundred degrees Celsius at the vacuum-vessel surface during baking to around 80–100 K at the shield and

4 K at the magnet system. These gradients cause substantial thermal strains and variations in material properties that directly influence stiffness, stress distribution, and preload stability in bolted joints. Accurate representation of temperature-dependent mechanical and thermal properties is therefore essential for reliable structural assessment and for ensuring the long-term performance of the DTT supports.

In ITER, all principal analyses incorporate temperature-dependent data for stainless steel 316L(N) and Inconel 718. The corresponding finite-element analyses were static but incorporated temperature-dependent material data to reproduce the mechanical effects of cool-down. According to [4], [19], cool-down is the dominant source of relative displacement between the vessel and the shield, producing maximum movements of approximately 18 mm without exceeding stress limits. Material hardening at cryogenic temperature increases the allowable stress margin, while the reduction in thermal expansion prevents over-tightening of the joints. Bolt pretension is applied at room temperature so that a sufficient clamping force is maintained after contraction to 80 K. This temperature-dependent preload strategy ensures that the shield remains mechanically stable throughout thermal cycling. The analyses also confirm that electromagnetic and seismic loads are secondary compared with the thermally induced deformations.

Among ITER analyses, the study [21] included a time-dependent simulation of the ten-day cool-down from 273 K to 80 K, limited to thermal transients without structural coupling.

The KSTAR experiments reported in [7] further demonstrate the influence of temperature distribution on structural performance. During baking, local temperatures of up to 160 K were recorded near support regions, while the overall panel temperature remained within 60–80 K. This non-uniform field modifies the preload of nearby fasteners and slightly redistributes loads among supports. Although no loss of mechanical integrity was observed, the study indicates that maintaining temperature uniformity around critical supports is important for consistent stress and preload conditions. The data were collected during operational transients of the machine, though numerical simulations remained steady-state.

The EAST analyses presented in [5] confirm that thermally induced loads dominate the mechanical response of the shield. Under combined gravity and thermal effects, the maximum stress reached approximately 220 MPa, increasing to about 402 MPa when electromagnetic forces were superimposed. The maximum displacement, approximately 5 mm, resulted primarily from thermal contraction. These findings confirm that structural performance is governed mainly by the temperature field and by the coefficient of thermal expansion of the materials used.

The Wendelstein 7-X studies in [6] emphasize the connection between thermal and electromagnetic behavior. Average shield temperatures were maintained between 75 K and 93 K, while maximum port-region temperatures approached 110 K. Brass was selected for the shield panels because of its stable mechanical properties at low temperature and its lower electrical conductivity compared with copper. This choice reduced both eddy-current heating and thermally induced stress, illustrating how appropriate material selection can address coupled thermal and electromagnetic requirements.

For DEMO, [13] and [14] show that the shield operating temperature affects not only the mechanical response but also the cryogenic efficiency. An optimal range of 100–125 K was identified, balancing reduced radiation and acceptable conduction. Operating outside this range leads to increased refrigeration power demand or higher material stress, confirming that mechanical and thermodynamic optimization must be carried out concurrently.

The temperature-dependent response of the DTT shield is examined in [17]. The material properties of stainless steel 316LN and G10-CR were defined as temperature-dependent in the finite-element model. This analysis considered temperature-dependent properties under steady equilibrium conditions. Predicted displacements reach up to 42 mm at the inner shield and 21 mm at the outer shield, values consistent with those of comparable large tokamaks. The highest stresses occur in the cooling pipes and bolts, at 150–260 MPa and 108–183 MPa respectively, still within allowable limits. These results indicate that the structural design can accommodate the expected thermal gradients. Complementary analyses in [3] and [10] reported shield temperatures below 100 K during plasma operation and below 130 K during baking. These studies were steady-state thermal evaluations and provided operating temperature fields that could be used as input for subsequent mechanical assessment.

Overall, the reviewed studies demonstrate that reliable design of shield supports depends strongly on temperature-dependent material characterization and on accurate modeling of preload variation during cool-down. At cryogenic temperature, stainless steels gain strength while thermal expansion coefficients decrease, reducing the risk of overstress but altering joint clamping forces. For DTT, the implementation of temperature-dependent data for all structural and insulating materials, combined with verification of preload stability throughout the operational cycle, will be essential to achieve both mechanical reliability and cryogenic efficiency.

2.5 Manufacturing and Tolerance Effects

Thermal shields are positioned within confined spaces between the vacuum vessel and the superconducting magnet structures, where available clearances are often less than a few tens of millimeters. Under such geometric restrictions, even small deviations introduced during manufacturing or assembly can significantly influence the mechanical and thermal performance of the system. The accuracy of welded joints, the alignment of support locations, and the cumulative tolerances of segmented panels must therefore be controlled carefully. These factors directly affect the achievable clearance, the preload of bolted joints, and the alignment of cooling circuits. The experience gained from existing machines provides valuable information for defining manufacturing and assembly tolerances in the DTT design.

The ITER program provides the most comprehensive documentation of tolerance management for large-scale cryogenic shields. According to [4] and [12], mock-up fabrication and assembly tests were used to validate feasible alignment sequences and to determine the tolerances achievable in industrial production. The outboard panel manufacturing process was limited by welding distortion of the cooling tubes and by spring-back of thin plates. The resulting tolerances were ±15 mm radially for the outboard panels and ±10 mm for the inboard panels, with linear and angular misalignments up to ±5 mm and ±2°, respectively. [18] demonstrates that these geometric deviations can modify contact reactions and local stress patterns. The morphing approach introduced measured deformations into the finite-element model, showing that misalignment increases stress near supports and joints, thereby confirming the necessity of incorporating manufacturing uncertainty in structural verification. The morphing-based deformation validation was performed under static mechanical loading with geometry modified from measured distortions.

Assembly aspects were also addressed in [11] and [22]. The introduction of rod-type supports, in place of the earlier plate configuration, simplified assembly and reduced envelope occupancy, while also improving access for inspection and tightening. Factory pre-assembly of 40° sectors was adopted to minimize on-site alignment operations and to ensure repeatable geometry during installation. The bolting sequence and joint closure procedures were verified experimentally to prevent accumulation of tolerances along the toroidal direction.

The Wendelstein 7-X shield was constrained by extremely tight spatial envelopes, requiring very precise alignment of panels and supports. As reported in [6], the adoption of brass and Torlon elements facilitated machining accuracy and reduced assembly complexity compared with copper. However, the high number of supports, approximately 1 400 including ports, increased the sensitivity of the system to positioning errors. The study highlights that uniform distribution of supports and precise control of pin length were necessary to prevent unintended mechanical loading of adjacent structures.

The KSTAR thermal shield system, described in [7], also experienced manufacturing challenges associated with welding distortion of the cooling tubes. The sequence of tube attachment and panel forming was optimized to limit residual stresses and to maintain geometric fidelity. Installation records note that one 45° sector of the vacuum-vessel thermal shield had to be installed after the placement of toroidal field magnets, demonstrating the need for flexible assembly planning. The leak-detection campaign, lasting approximately three months, further illustrates the importance of fabrication quality and inspection for cryogenic components.

In EAST, fabrication tolerances are managed through the modular segmentation of the thermal shield. The shield consists of multiple panels joined by bolted connections that allow minor alignment adjustment during assembly. As discussed in [5], ribs were added to maintain panel rigidity and to limit distortion during welding and cool-down. The analysis indicates that these stiffeners not only enhance mechanical strength but also improve geometric stability under thermal gradients.

The DTT analyses confirm that manufacturing and alignment accuracy are crucial due to the very limited clearances available. [17] reports that the minimum gaps between the vacuum vessel, the inner shield, and the outer shield are in the range of 8–13 mm. These margins can be consumed easily by small fabrication or assembly deviations. The same study identifies the top-inboard region as the most sensitive area, where the gap approaches the minimum limit during thermal contraction. The beam-element simulations suggest that geometric tolerances at bolt locations and panel edges should be controlled within a few millimeters to maintain operational clearances. The related thermal analyses in [3] and [10] highlight that panel flatness and tube placement accuracy also affect the uniformity of the temperature field, which in turn influences local stresses and heat flux distribution.

The reviewed studies indicate that tight tolerance control is not only a geometric requirement but also a functional necessity for maintaining structural integrity and thermal performance. The accumulation of small deviations during fabrication and assembly can lead to stress concentration, uneven contact forces, and reduced clearance. For the DTT thermal shield, the establishment of strict dimensional control procedures, early verification through mock-up testing, and integration of measured geometry into numerical models are recommended to ensure consistent performance under both static and thermal loads.

2.6 Secondary Drivers: Electromagnetic Isolation, Assembly, and Cryogenic Efficiency

In addition to mechanical and thermal performance, thermal shield design must also satisfy several secondary requirements that strongly influence its overall feasibility. These include electromagnetic (EM) isolation to suppress eddy-current forces, maintainability and assembly accessibility for inspection and leak testing, and cryogenic efficiency to minimize the total refrigeration power demand. Although these aspects are often considered secondary, experience from existing devices demonstrates that they govern the long-term operability and maintainability of the shield system. These aspects are therefore relevant to the assessment and further development of the DTT thermal shield system.

Electromagnetic isolation plays a central role in limiting the induced currents and transient forces generated during plasma disruptions or fast magnet discharges. In ITER, EM control is achieved through the use of bolted electrical breaks distributed toroidally and poloidally across the shield. Thirty-six toroidal and two poloidal insulation joints were implemented, preventing the formation of continuous conductive loops. G10 insulation blocks placed within the supports further increase electrical resistance and reduce both eddy currents and conductive heat flow [12], [20]. The effectiveness of this strategy was confirmed during structural verification, which showed that electromagnetic loads were not the governing design constraint. The same concept of electrically insulated joints was incorporated into the cryostat and magnet interfaces to maintain continuity of EM isolation [4].

A similar design philosophy was applied in KSTAR. The supports and connection bolts were electrically insulated by epoxy-glass composites and insulated fasteners to interrupt current paths. The study reported in [7] notes that this configuration successfully prevented large eddy-current loops and avoided any observed electromagnetic interference with the magnet system. The same paper emphasizes that the inclusion of electrical insulation did not compromise the mechanical or thermal performance of the supports, confirming that EM isolation can be integrated effectively within the structural design.

In Wendelstein 7-X, electromagnetic effects were particularly important due to the complex geometry of the stellarator and the rapid current decay of the superconducting coils. As documented in [6], initial copper panels induced large eddy currents that generated support forces up to 49.5 kN. Replacing copper with brass and adding electrical isolation between the upper and lower shell halves reduced the maximum force to less than 1 kN. The same configuration limited structural stresses to below 100 MPa, well within the yield strength of brass at 80 K. This case demonstrates the effectiveness of electrical segmentation and the use of low-conductivity alloys in reducing electromagnetic loads.

For EAST, electromagnetic isolation was achieved using insulated dowels and poloidal electrical breaks between shield segments. These design features are described in [5], which reports that the adopted segmentation minimized induced currents during transient events. The inclusion of insulation layers in the gravity supports simultaneously reduced conduction and prevented electrical coupling between adjacent panels.

Assembly and maintainability requirements are also decisive for shield feasibility. The large size and intricate geometry of the ITER shield demanded factory pre-assembly of 40° sectors, followed by in-situ bolting and alignment. This procedure ensured repeatable geometry while reducing on-site welding and handling risks [22]. Mock-up trials confirmed that the assembly process maintained the required clearances without excessive accumulation of tolerances. The adoption of rod-type supports instead of plate structures simplified installation and improved access for inspection. Similarly, [7] reports that installation sequencing was adjusted to accommodate the simultaneous presence of the toroidal-field magnets. Leak detection and pressure testing were essential parts of the quality-assurance process, demonstrating that maintainability considerations strongly influence design details such as weld routing and connector accessibility.

The cryogenic efficiency of the shield system depends on both the total heat load and the distribution of thermal stages within the refrigerator. For DEMO, [13] and [14] identify the shield temperature as a key parameter governing overall refrigeration power. The optimal operating temperature of approximately 100–125 K minimizes combined radiation and conduction losses, thereby reducing required refrigerator power by nearly 35% compared with the baseline case. The studies also show that multilayer insulation (MLI) on the vacuum-vessel shield yields the largest improvement in cryogenic performance, while separate cooling of the vacuum-vessel and cryostat shields provides limited benefit. The DEMO investigations were performed under steady-state radiative and conductive conditions, establishing static heat-load balances without transient coupling.

The same thermal-efficiency principles are confirmed for DTT. According to [3], which used steady-state ANSYS radiation analyses combined with transient RELAP5-3D thermal-hydraulic modeling of the coolant loop, the total heat load on the shield under plasma operation is approximately 30 kW, and the application of MLI to the cryostat thermal shield reduces this to about 19 kW. The CTS, identified as the primary access path for radiation to the magnets, exhibits the greatest potential for improvement through local insulation. Further analysis in [10] shows that optimization of tube routing and panel rib spacing enhances temperature uniformity and decreases pumping power. These results confirm that cryogenic efficiency can be improved substantially through localized thermal design adjustments without altering the overall mechanical configuration.

The reviewed studies indicate that electromagnetic isolation, assembly strategy, and cryogenic efficiency are interdependent factors that strongly influence shield design. Electrical insulation must be incorporated into both supports and joints to limit eddy-current forces, while assembly procedures must allow repeatable alignment and accessibility for inspection. At the system level, cryogenic performance depends on temperature optimization, insulation placement, and the integration of cooling circuits. For DTT, G10-CR insulation in the bolted supports, segmented electrically isolated panels, and MLI in the cryostat shield region contribute to balancing electromagnetic isolation, assembly feasibility, and cryogenic efficiency.

2.7 Summary and Implications for the Present Study

The reviewed studies show that thermal shield support systems are governed by coupled structural, thermal, and integration requirements. For the present work, the most relevant aspects are the support cross-section as a geometric indicator of conductive path availability, the need for controlled constraint definitions to accommodate thermal contraction, the distinction between global support-level modeling and detailed local attachment verification, and the preservation of clearance between adjacent structures.

These points define the basis of the finite element methodology developed in Chapter 3. In this thesis, conductive heat transfer is not solved directly, but the support-member cross-sectional area is used as a geometric indicator of the available conductive path when comparing the reference and mixed-diameter configurations. Thermal contraction is represented through prescribed structural temperature fields, and insulation-gap preservation is assessed by comparing initial and deformed gap-result fields.

Chapter 3

Finite Element Modeling Methodology

3.1 DTT Cryostat and Thermal Shield System

The DTT cryostat constitutes the external vacuum boundary of the machine and provides the structural enclosure for the superconducting magnet system together with the associated cryogenic components. Within this environment, the thermal shield system is positioned between the relatively warm cryostat vessel and the low-temperature internal structures in order to reduce the heat load transmitted toward the cryogenic region.

The present work focuses on the support configuration connecting the cryostat thermal shields to the cryostat body. These supports form an important thermo-mechanical interface because they must simultaneously provide adequate structural stiffness while limiting conductive heat transfer between components operating at substantially different temperatures. Consequently, the support system must sustain the weight of the thermal shields, accommodate differential thermal contraction, maintain acceptable stress levels, and preserve the required separation between the thermal shields and the cryostat body during operation.

The investigated system consists of a cryostat body and a corresponding thermal shield assembly arranged concentrically with respect to one another. The thermal shield assembly can be divided into three principal regions: the cylindrical thermal shield, the dome thermal shield, and the top-cover thermal shield, which follow the general geometry of the enclosing cryostat structure. The cylindrical thermal shield consists of two cylindrical portions connected through an inclined transition section. Above the cylindrical region, the structure transitions into the dome thermal shield, which provides the geometrical connection to the central top-cover region.

Several openings are present within both the cryostat body and the thermal shields in order to accommodate ports and auxiliary systems.

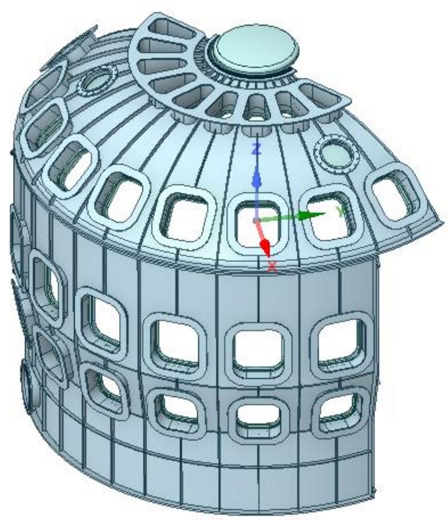

Figure 3.1 Overall geometry of the DTT cryostat body and thermal shield system, showing the cylindrical region, dome region, top-cover region, and main openings.

The principal dimensions of the investigated cryostat and thermal shield geometry are summarized in Table 3.1. These dimensions define the global scale of the finite element model and the characteristic size of the shell regions considered in the structural analyses.

Table 3.1 Principal dimensions of the investigated cryostat and thermal shield geometry.

Geometrical quantity	Value
Upper cylindrical/dome diameter	10800 mm
Lower cylindrical diameter	10500 mm
Cylindrical body height	6950 mm
Dome height	2170 mm

Top-cover diameter	2160 mm
Top-cover height	720 mm
Average cryostat–thermal shield gap	147.5 mm

The average distance between the cryostat body and the thermal shields is approximately 147.5 mm. This separation defines the insulation gap and also corresponds approximately to the length of the support members connecting the thermal shields to the cryostat structure. Preservation of this gap is one of the principal functional requirements of the support system, since excessive deformation could lead to local interference between the cryostat body and the thermal shields.

The thermal shield masses considered in the finite element model are summarized in Table 3.2. These masses provide the reference self-weight values associated with the thermal shield regions and are also used in the preliminary support-sizing calculation discussed in a later section.

Table 3.2 Masses of the cryostat thermal shield components considered in the finite element model.

Thermal shield component	**Mass**
Cylindrical thermal shield	1392.7 kg
Dome thermal shield	937.6 kg
Top-cover thermal shield	45.7 kg

The following section describes the geometrical idealization procedure adopted to transform the physical configuration into a finite element model suitable for structural analysis under mechanical and thermal loading.

3.2 Geometrical Modeling and Idealization

The original CAD geometry was simplified prior to finite element discretization in order to obtain a computationally efficient model suitable for global structural analysis under mechanical and thermal loading. The geometric processing was performed in ANSYS SpaceClaim, where midsurfaces were extracted from the three-dimensional bodies using the middle-offset option. This approach is particularly suitable for the cryostat and thermal shield structures because their characteristic thicknesses are small compared with their overall dimensions, allowing the dominant membrane and bending behavior to be represented efficiently through shell elements.

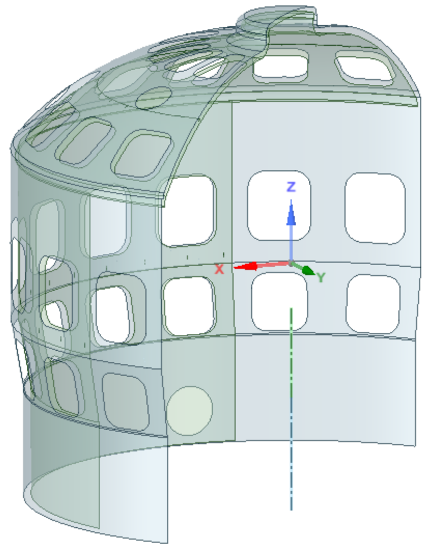

Figure 3.2 Midsurface representation of the cryostat body and thermal shields after geometrical simplification in ANSYS SpaceClaim.

The cryostat body was represented as a single shell structure comprising the cylindrical region, the dome region, and the top-cover region. In contrast, the thermal shields were maintained as separate shell bodies in order to allow explicit modeling of their interaction with the cryostat body through the support system.

Several local geometrical features, including ribs, secondary flanges, and small structural details, were omitted during the idealization process. Since the objective of the present study is the evaluation of the global structural behavior of the support configuration, the simplified geometry was adopted to capture the overall deformation, load-transfer, and stress response of the cryostat and thermal shield system. Local verification of omitted attachment details was outside the scope of the present model.

To reduce computational cost while preserving the dominant structural behavior, sector models were adopted for the different regions of the assembly. The cylindrical thermal shield and the corresponding cryostat region were represented over a 120° sector, whereas the dome thermal shield and the associated cryostat region were represented over a 180° sector. The top-cover thermal shield was initially modeled as a complete circular component and subsequently reduced to a half model to permit the application of symmetry conditions.

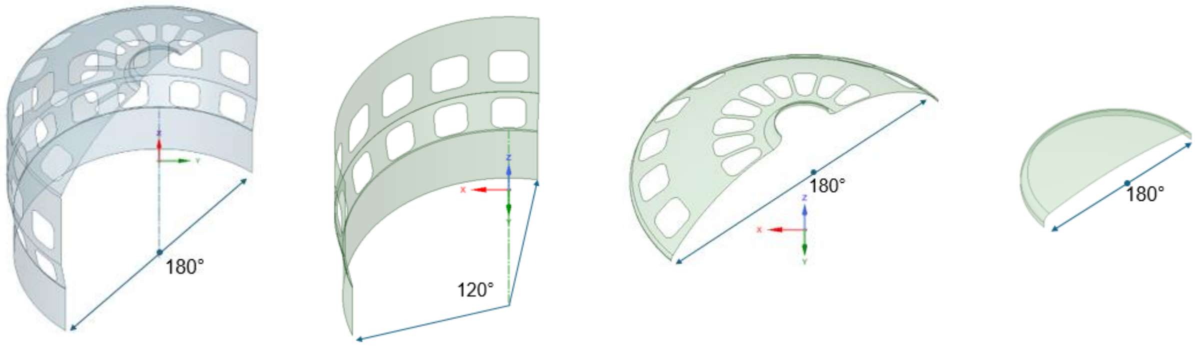

Figure 3.3 Sector representation adopted for the cylindrical, dome, and top-cover thermal shield regions.

For the dome region, the adjacent cylindrical portions of the cryostat body were extended to the same 180° angular extent as the dome model. This modification was introduced to avoid unrealistic unsupported regions near the sector boundaries and to allow the reduced angular model to better reproduce the structural behavior of the complete assembly.

The extracted midsurfaces were assigned equivalent shell thicknesses corresponding to the physical structures. The adopted shell thicknesses are summarized in Table 3.3.

Table 3.3 Equivalent shell thicknesses adopted in the finite element model.

Component	Shell thickness (mm)
Cryostat body	20
Thermal shields	3

The support members were generated from construction lines connecting the thermal shields to the cryostat body across the insulation gap. These lines were created normal to the corresponding shell surfaces and subsequently converted into beam elements. In the cylindrical region, this direction is essentially radial, whereas in the dome region the support orientation varies according to the local geometry of the shell surface.

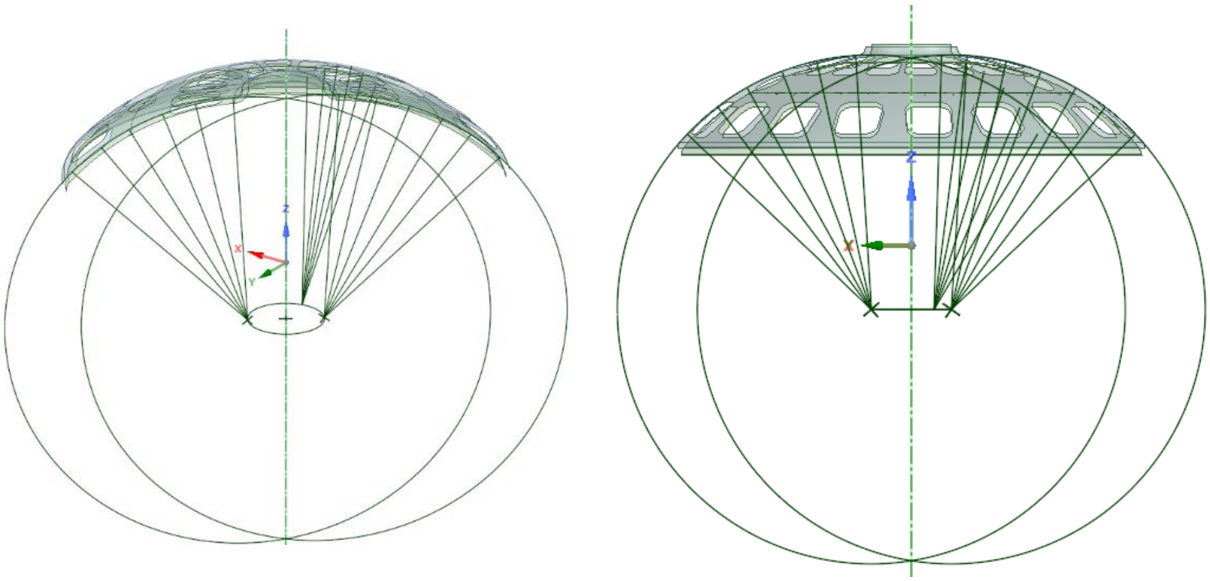

Figure 3.4 Example of construction lines used to generate the support members between the cryostat body and the thermal shields.

The support members were represented using beam elements with circular cross-sections. This idealization was adopted to reproduce the dominant stiffness and load-transfer behavior of the supports while maintaining a computationally efficient numerical model. The beam representation captures the global force, moment, and deformation response of the support system, but it does not include detailed local effects associated with bolt heads, washers, attachment pads, local contact footprints, assembly tolerances, or manufacturing imperfections. The implications of the idealized beam-to-shell interface definitions are discussed in the contact and joint modeling section.

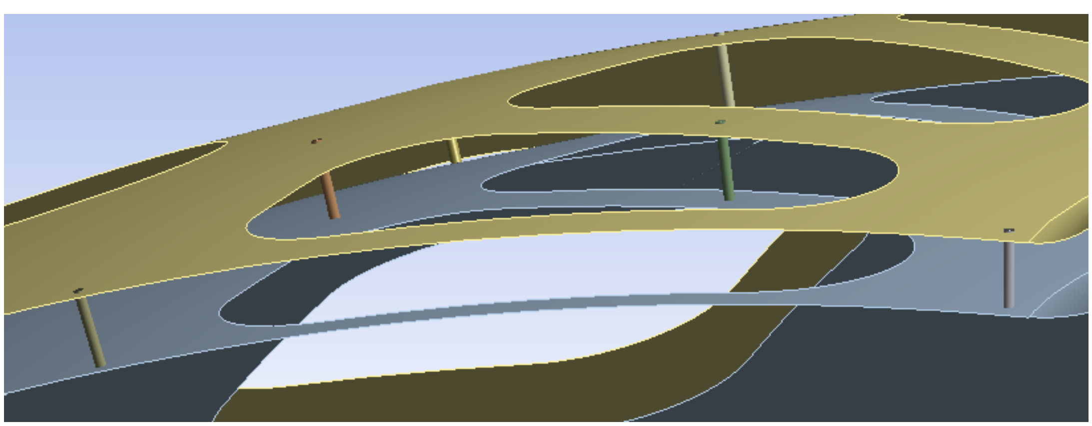

Figure 3.5 Beam-element representation of a thermal shield support member.

3.3 Material Properties

The finite element model requires material definitions for the cryostat body, thermal shields, and support members. Since the objective of the present work is the evaluation of the global structural response of the support system under mechanical and thermal loading, linear elastic material behavior was assumed throughout the analyses.

The cryostat body and thermal shields were assigned stainless steel 316LN properties representative of cryogenic structural applications. The support members were assigned G10-CR fiberglass epoxy material properties. G10-CR is commonly used in cryogenic structural-insulating applications because it combines relatively low thermal conductivity with sufficient mechanical strength. Experimental characterization of G-10CR glass-cloth/epoxy laminates between room temperature and 4 K [23] shows that their mechanical properties depend on fiber direction, manufacturer, and temperature, and that strength generally increases at cryogenic temperature.

Since the support members were represented using BEAM188 elements, the full orthotropic behavior of G10-CR was not represented explicitly. Instead, an equivalent linear elastic material definition was adopted for the beam model. The lengthwise Young's modulus from the adopted G10-CR material data was used as the equivalent Young's modulus, while the crosswise Poisson's ratio was used as the Poisson's ratio input. No explicit laminate orientation or material-direction assignment was introduced for the beam elements. Therefore, the calculated support stresses were interpreted as beam-level stress quantities for the global support model rather than as detailed laminate-level stresses.

Temperature-dependent material properties were assigned in order to account for the influence of temperature on elastic stiffness and thermal expansion. The material properties adopted for stainless steel 316LN [24–27] and G10-CR fiberglass-epoxy [28], [23] are summarized in Tables 3.4 and 3.5, respectively.

Table 3.4 Temperature-dependent material properties adopted for stainless steel 316LN.

Temperature [°C]	Density [kg/m³]	Young's modulus [GPa]	Poisson's ratio	Coefficient of thermal expansion [μm/m°C]
-193	8000	210	0.3	13.3
23	8000	200	0.3	16.5
60	8000	193	0.3	16.3
200	8000	183	0.3	16.8

Table 3.5 Temperature-dependent material properties adopted for G10-CR fiberglass-epoxy.

Temperature [°C]	Density [kg/m³]	Young's modulus [GPa]	Poisson's ratio	Coefficient of thermal expansion [μm/m°C]
-269	1800	35.9	0.210	3.06
-196	1800	33.7	0.183	20.64
22	1800	28	0.144	20.62

The values listed in Tables 3.4 and 3.5 correspond to the material data implemented in the ANSYS Engineering Data module. These properties were used consistently in the gravity, thermal, combined, and eigenvalue buckling analyses presented in the following sections.

3.4 Finite Element Formulation

The cryostat body, thermal shields, and support members were represented using finite element formulations selected according to their dominant structural behavior. Shell elements were adopted for the thin-walled cryostat and thermal shield structures, while beam elements were used for the discrete support members. This modeling strategy provides an efficient representation of the global structural response under gravity loading and imposed thermal loading.

3.4.1 Shell Element Formulation

The cryostat body and thermal shields were discretized using SHELL181 finite elements. SHELL181 is a four-node shell element suitable for thin and moderately thick shell structures and accounts for membrane deformation, bending deformation, and transverse shear deformation [29].

Each shell node possesses six degrees of freedom: translations along the global x, y, and z directions, and rotations about the x, y, and z axes. This formulation is appropriate for the present model because the cryostat body and thermal shields are represented as midsurface shell structures, where both membrane and bending effects contribute to the global response.

The SHELL181 formulation is based on first-order shear deformation shell theory, commonly referred to as Reissner–Mindlin shell theory. This formulation includes transverse shear deformation and is therefore suitable for the global structural analysis of the thin-walled components considered in this work. In this type of shell idealization, the three-dimensional structural behavior is represented through quantities defined on the midsurface of the shell. The response is therefore described in terms of membrane action, bending action, and transverse-shear contribution, which is appropriate for the global modeling of the cryostat body and thermal shield panels adopted in this thesis [30].

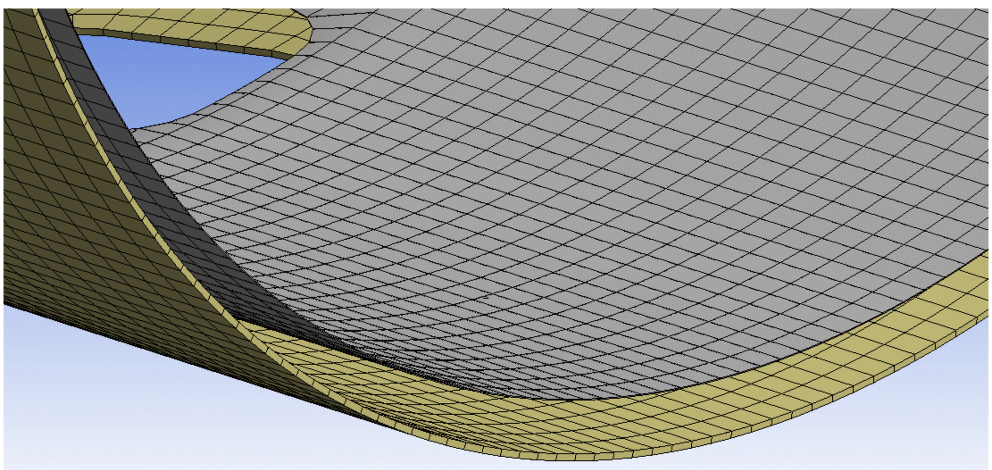

Figure 3.6 Shell finite element representation adopted for the cryostat body and thermal shield structures.

3.4.2 Beam Element Formulation

The support members connecting the thermal shields to the cryostat body were discretized using BEAM188 finite elements. BEAM188 is a three-dimensional beam element suitable for slender to moderately thick beam structures. The element includes axial deformation, bending deformation, torsional deformation, and transverse shear deformation [31].

Each beam node possesses six degrees of freedom: translations along the x, y, and z directions and rotations about the x, y, and z axes. The support members were assigned circular cross-sections corresponding to the selected support diameters. The beam formulation was adopted because the support members act as discrete one-dimensional load-transfer elements between the thermal shield and cryostat shell structures, and the main quantities of interest are the support forces, bending moments, deformations, and beam-level stresses.

The beam formulation provides an efficient representation of the global load-transfer behavior of the support system. The use of a beam formulation including transverse shear deformation is relevant for the present support members. In Euler–Bernoulli beam theory, cross-sections remain plane and orthogonal to the beam axis and transverse shear deformation is neglected. In Timoshenko beam theory, cross-sections remain plane but are not required to remain orthogonal to the deformed beam axis, so transverse shear deformation is included [30]. This distinction is important for the present supports, especially for the 20 mm members, whose approximate length-to-diameter ratio is 147.5/20 = 7.4. Therefore, the support-member results were interpreted in terms of member-level axial force, shear force, bending moment, direct stress, and combined beam stress. Detailed local features such as bolt heads, washers, attachment pads, weld regions, and local contact footprints were not represented by the beam elements. These modeling assumptions are discussed in the support interface and connection modeling section.

3.5 Support System Configuration and Constraint Modeling Strategy

This section describes the support configuration used in the finite element model and the constraint definitions assigned to the support interfaces. These definitions control how the support members transfer reactions to the cryostat and thermal shield shells, and how relative motion is treated during thermal contraction.

The support configuration was developed based on the available geometry of the cryostat and thermal shields, preliminary sizing, and finite element assessment. The initial support positions were selected along the main structural paths of the cylindrical and dome thermal shields, especially in regions between openings where load transfer to the cryostat could be achieved. For the cylindrical thermal shield, the main vertical load-carrying supports were selected with the aid of the preliminary hand calculation reported in Appendix A. In this calculation, the cylindrical thermal shield weight was distributed among candidate vertical support locations, and each support member was idealized as a cantilever-type member subjected to the corresponding transverse load.

The preliminary calculation was used only to guide the initial support selection before the finite element analysis. The finite element model was then used to assess the deformation, stress level, contact-gap behavior, and overall response of the structure. In Chapter 4, the displacement estimated from the hand calculation is also compared with the finite element gravity-deformation result as an analytical cross-check of the predicted deformation magnitude. The final reaction forces, support stresses, deformation fields, and gap behavior were obtained from the finite element model. The details of the preliminary calculation are reported in Appendix A.

During the support-definition process, physical support members and contact/interface definitions were treated as different modeling entities. The support members represent structural members with finite stiffness and stress response, while the contact/interface definitions describe how selected surfaces interact in the model. Therefore, the final configuration should be understood as an engineering-refined support arrangement based on geometry, preliminary sizing, and finite element assessment. It was not a uniformly spaced layout and was not obtained through a formal mathematical optimization procedure.

In the reference configuration, all support members were assigned a circular cross-section with a diameter of 20 mm. This configuration was used as the baseline finite element model for the gravity, thermal, combined loading, and buckling analyses. The later mixed-diameter configuration is discussed separately in the sensitivity assessment section.

The cryostat-side endpoints of the support members were connected to the cryostat shell using bonded contact. This choice was made to transfer the reactions from the support members into the cryostat body and to prevent relative displacement at the cryostat-side attachment.

At the thermal-shield side, bonded contact, joint-based constraints, and no-separation contact were assigned according to the required behavior at each support location. These definitions were used to provide the required structural restraint while avoiding excessive constraint of thermal contraction. The adopted interface definitions are summarized in Table 3.6.

Table 3.6 Interface definitions adopted for the support members and gap-verification contacts.

Interface definition	Location in the model	Function in the finite element model
Bonded contact	Cryostat-side endpoint of all support members	Enforces displacement compatibility between each support endpoint and the cryostat shell and transfers support reactions into the cryostat body
Bonded contact	One thermal-shield-side support endpoint at a near central location on each thermal shield	Enforces displacement compatibility between the selected support endpoint and the thermal shield shell; prevents separation and sliding at that interface
Joint-based constraint	13 support locations on the cylindrical thermal shield and one support location on the dome thermal shield	Applies selected translational constraints in local coordinates while releasing rotations and selected displacement directions
No-separation contact	Remaining thermal-shield-side support endpoints not assigned bonded contact or joint-based constraints	Prevents separation in the local contact-normal direction while allowing tangential sliding
Frictionless contact	Facing surfaces between the cryostat body and the thermal shields	Detects possible local closure of the insulation gap during deformation

Mechanically, these interface definitions impose different constraints on the relative displacement of the paired regions. Bonded contact constrains relative motion at the connected interface, no-separation contact prevents separation in the local contact-normal direction while allowing tangential sliding, and frictionless contact can transmit a normal reaction only if the monitored surfaces tend to close. These contact-type definitions are consistent with the general treatment of contact problems as constrained mechanical problems in which normal gap, penetration, and contact-status conditions must be enforced through an appropriate numerical formulation [32]. Therefore, the selected interface definitions control both load transfer and displacement compatibility in the global support model.

The distribution of the thermal-shield-side support-interface definitions is shown in Figure 3.7. This figure identifies which support locations were modeled using bonded contact, no-separation contact, and joint-based constraints.

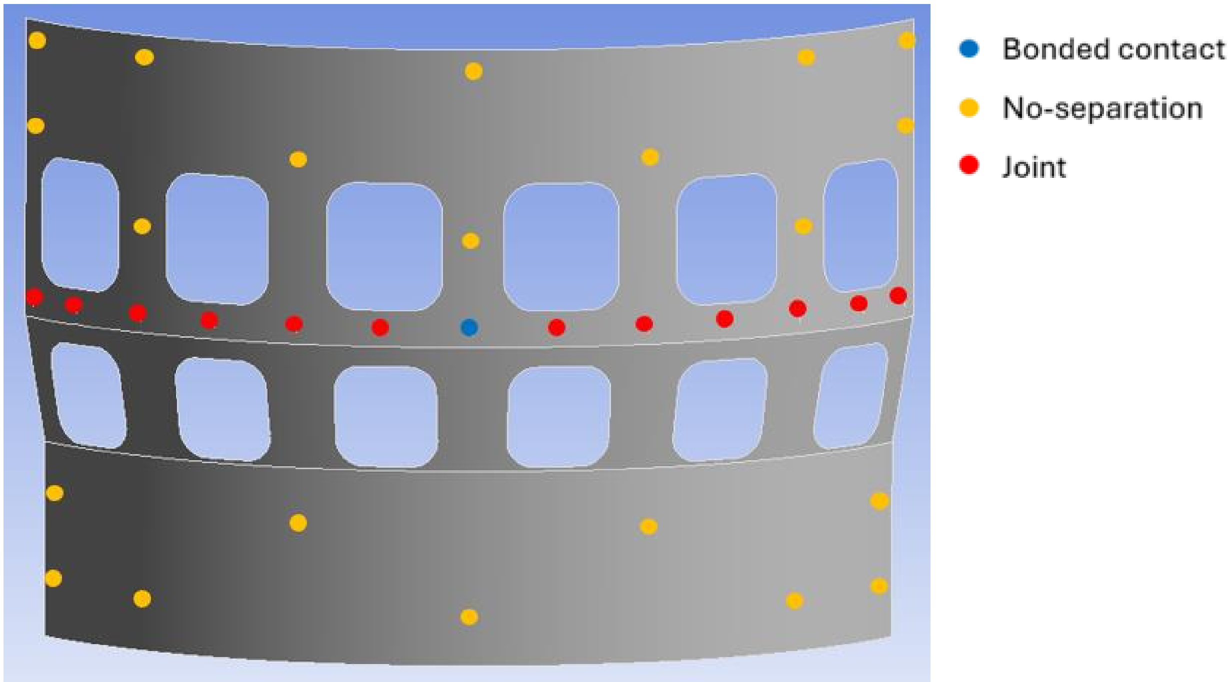
Bonded contact
No-separation
Joint

(a)

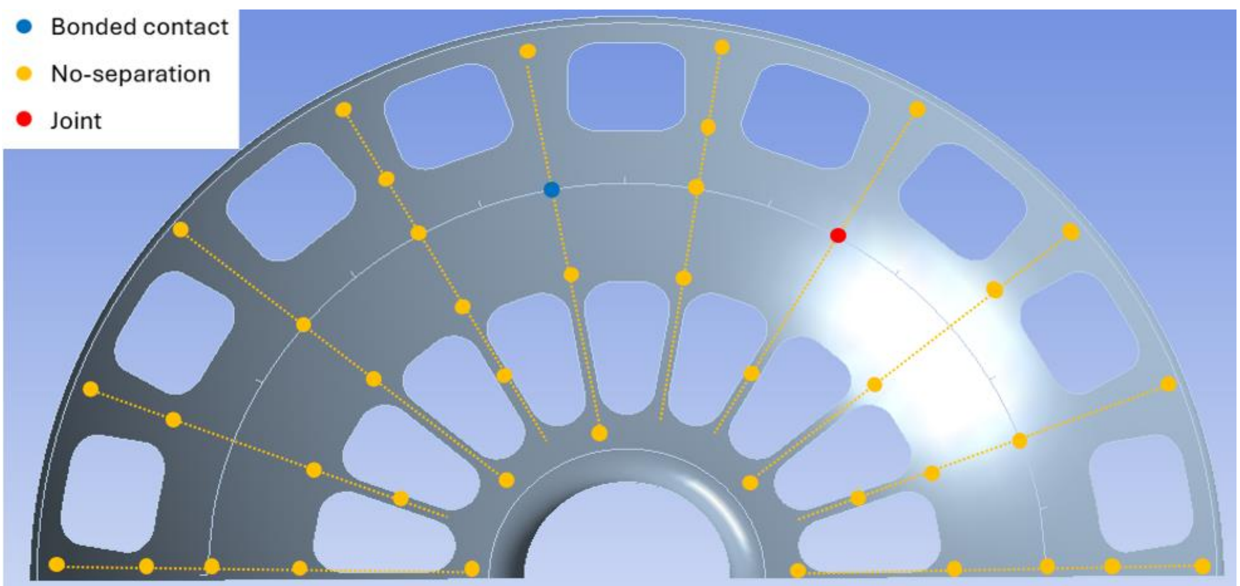
Bonded contact
No-separation
Joint

(b)

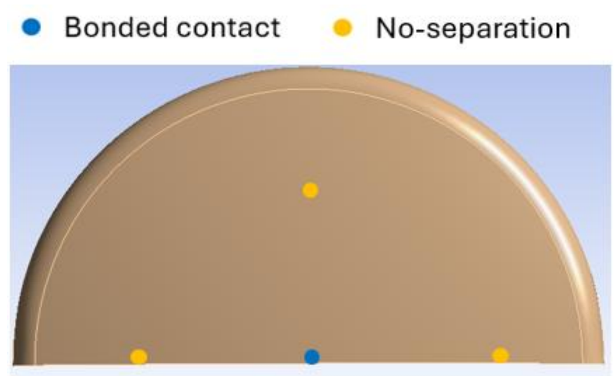

(c)

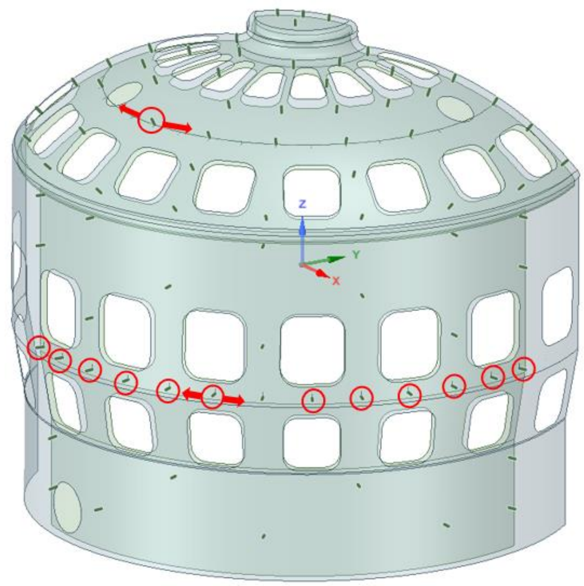

(d)

Figure 3.7 Distribution of thermal-shield-side support-interface definitions adopted in the finite element model: (a) cylindrical thermal shield; (b) dome thermal shield; (c) top-cover thermal shield; (d) global 3D view of the support arrangement.

The support-to-shell interfaces were idealized as beam-endpoint-to-shell connections, with each beam endpoint connected directly to the shell surface. Bolt heads, washers, attachment pads, weld regions, and imprinted contact footprints were not modeled. Accordingly, this representation was used to evaluate global support behavior and load transfer, not the detailed stress field of the real attachments.

Bonded contact was used to represent tied interfaces in the finite element model. In this definition, relative displacement between the connected regions is constrained. As a result, separation and tangential sliding are not permitted at the bonded interface. On the thermal-shield side, bonded contact was assigned to one near-central support endpoint for each thermal shield region. These bonded locations provide fixed displacement compatibility between the selected support endpoint and the corresponding thermal shield shell.

Joint-based constraints were used where the constrained and released directions had to be defined explicitly. In total, 13 joint-based supports were defined on the cylindrical thermal shield and one joint-based support was defined on the dome thermal shield. A dedicated local coordinate system was defined for each joint-based support, so that the constrained directions could be assigned according to the local support orientation.

For the cylindrical thermal shield, the local coordinate system of each joint was defined so that the support direction, vertical direction, and circumferential direction could be treated separately. The vertical translational constraint was retained to provide vertical support reaction, while circumferential motion was released to allow thermal contraction of the cylindrical shell. The rotational degrees of freedom were released so that the joint-based supports did not impose the same rotational restraint as bonded supports.

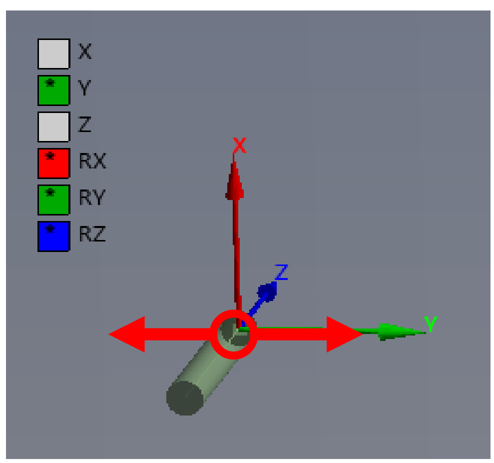

Figure 3.8 Local coordinate systems adopted for cylindrical support-joint definitions and the allowed DOFs.

For the dome thermal shield, one joint-based support was used. A dedicated local coordinate system was also defined for this joint, so that the constraint directions were assigned according to the local support orientation rather than a global coordinate axis. The gravitational load transfer in the dome model was governed by the complete support arrangement, not by the joint-based support alone.

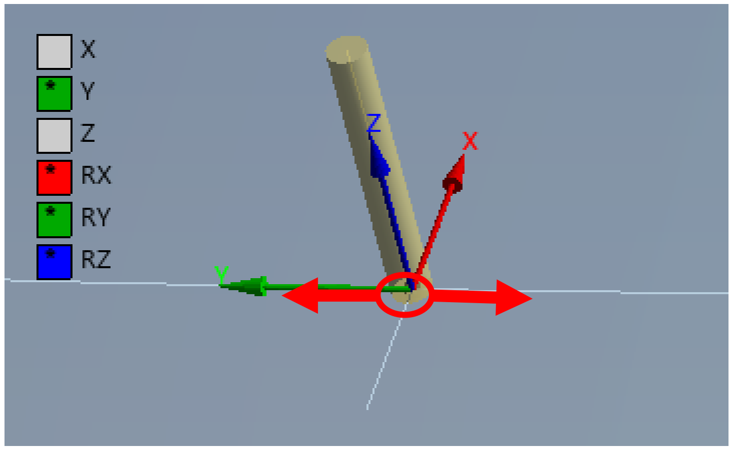

Figure 3.9 Local coordinate systems adopted for dome support-joint definitions and the allowed DOFs.

No-separation contact was used at the remaining thermal-shield-side support endpoints. This definition prevents separation in the local contact-normal direction but allows sliding in the tangential directions. This distinction is relevant under thermal loading, because the thermal shields contract relative to the cryostat body.

Frictionless contact interfaces were also defined between the facing cryostat and thermal-shield surfaces. These interfaces were not part of the support load path while the structures remained separated. They were introduced to monitor the insulation gap during deformation by providing gap-result fields between the cryostat body and the thermal shields. The interpretation of these gap results is described separately in the insulation-gap assessment section.

3.6 Nonlinear Solution Strategy

The structural analyses were performed using linear elastic material properties and small-deformation kinematics. However, the presence of contact interfaces required a nonlinear solution procedure because the contact definitions may introduce displacement-dependent constraint conditions, even when the final monitored gap contacts remain open. This nonlinearity was associated mainly with the contact definitions used at the support interfaces and with the frictionless contacts introduced for insulation-gap monitoring, because the active contact constraints and their associated stiffness terms depend on the current displacement field [32].

During the solution, the contact status may change depending on the deformation of the connected bodies. In particular, the frictionless contacts between the cryostat body and the thermal shields may remain open or become active if the insulation gap is locally reduced. When a contact condition becomes active, the corresponding constraint modifies the stiffness and residual contributions of the finite element system. Equilibrium was therefore obtained through the iterative nonlinear solution procedure available in ANSYS Mechanical.

The analyses were solved using the Newton–Raphson method implemented in the ANSYS Mechanical solver. In this procedure, the displacement field is updated iteratively until the force and displacement convergence criteria are satisfied [33].

The nonlinear behavior considered in this work was therefore limited to contact interactions. Material nonlinearity, plastic deformation, creep, and large-deformation geometric effects were not included in the model.

3.7 Boundary Conditions and Loading Cases

This section describes the external constraints and loading cases applied in the finite element analyses.

Symmetry boundary conditions were applied to the reduced sector models in order to represent the continuation of the structure outside the modeled angular domain. These conditions restrain displacement normal to the symmetry plane and the rotations associated with deformation out of that plane, while allowing in-plane deformation of the modeled sector.

Two symmetry conditions were defined on the corresponding symmetry surfaces of the model. Except for these symmetry constraints, no additional constraints were applied directly to the free edges of the thermal shields. This allowed the deformation of the thermal shields to be governed by the support system and the applied loads.

The lower edge of the cryostat body was assigned the ANSYS simply supported boundary condition, which restrains translational motion at the selected edge while leaving rotations free. This suppressed rigid-body motion without imposing a fully fixed boundary condition.

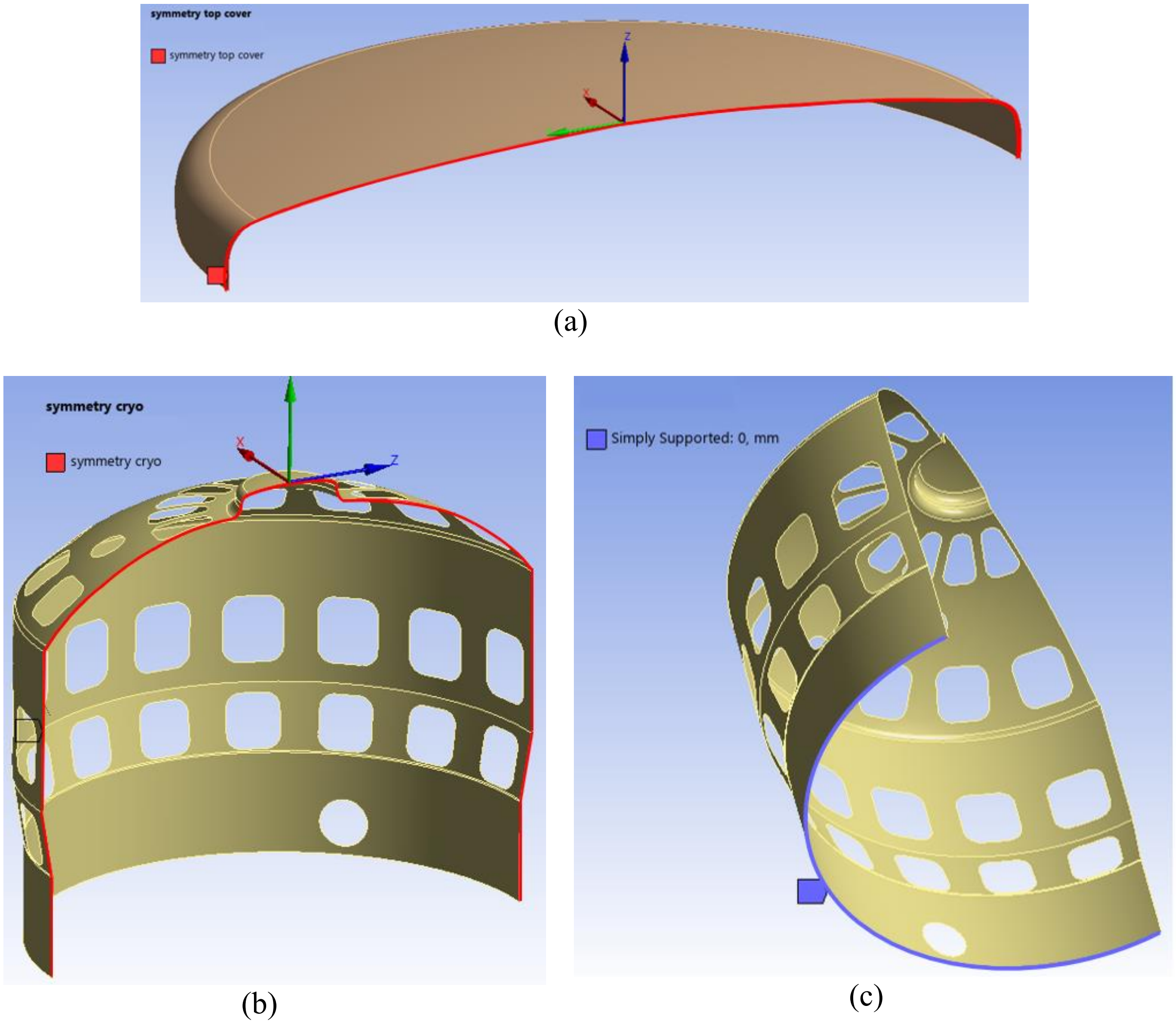

Figure 3.10 Boundary conditions adopted in the finite element model: (a) first symmetry boundary condition, (b) second symmetry boundary condition, and (c) simply supported boundary condition at the lower edge of the cryostat body.

The structural response of the thermal shield system was evaluated under three loading cases: gravity loading, thermal loading, and combined gravity and thermal loading. These cases were defined in order to separate the contribution of self-weight from the contribution of differential thermal contraction, and then to evaluate their combined effect.

In the gravity loading case, gravitational acceleration was applied to the complete model. This load case represents the structural response produced by the self-weight of the thermal shields and support members. It was used to evaluate the gravity-induced deformation of the shields, the reaction forces transmitted through the support system, and the corresponding stress distribution.

In the thermal loading case, uniform temperatures were prescribed directly in the structural model. The cryostat body was assigned a temperature of 23 °C, while the thermal shields were assigned a temperature of −166 °C. No steady-state or transient thermal analysis was performed. The applied temperatures were therefore used as prescribed structural temperature fields, rather than as the result of a heat-transfer calculation.

Table 3.7 Prescribed temperatures adopted for the structural analyses.

Component	Temperature
Cryostat body	23 °C
Thermal shields	−166 °C

The imposed temperature difference causes the thermal shields to contract relative to the cryostat body. Since the two structures are connected through the support system, this free contraction is partially restrained and produces both deformation and thermally induced stresses.

Thermal strain was evaluated relative to the reference temperature of 22 °C defined in the model. For a temperature-dependent coefficient of thermal expansion, the thermal strain may be written as:

$$\varepsilon_{th} = \int_{T_{ref}}^{T} \alpha(T)dT \tag{3.1}$$

where ε_{th} is the thermal strain, $\alpha(T)$ is the temperature-dependent coefficient of thermal expansion, T is the applied temperature, and T_{ref} is the reference temperature.

If a mean coefficient of thermal expansion is considered over the temperature interval, the free deformation of an unconstrained length can be approximated by

$$\Delta L = \alpha L \Delta T \tag{3.2}$$

where ΔL is the free thermal deformation, α is the mean coefficient of thermal expansion, L is the characteristic length, and ΔT is the temperature change relative to the reference temperature.

The combined loading case includes gravitational acceleration and the prescribed temperature field in the same analysis. This case represents the condition in which the support system is subjected simultaneously to self-weight and differential thermal contraction.

The loading cases investigated in the present work are summarized in Table 3.8.

Table 3.8 Structural loading cases investigated in the finite element analyses.

Load case	Gravity loading	Thermal loading	Purpose
Gravity	Yes	No	Evaluation of gravity-induced deformation, support reactions, and stresses
Thermal	No	Yes	Evaluation of thermal-contraction deformation and thermally induced stresses
Combined	Yes	Yes	Evaluation of the combined response under self-weight and differential thermal contraction

3.8 Meshing Strategy

The finite element mesh was generated in ANSYS Mechanical according to the element types assigned to each structural component. The cryostat body and the thermal shields were discretized using SHELL181 elements, while the support members were discretized using BEAM188 elements.

The shell mesh was generated on the midsurface representation of the cryostat body and thermal shields. A quad-dominant meshing approach was used where the geometry allowed it, while triangular elements were also present in regions with openings, curved boundaries, and local geometrical transitions. This mesh strategy was adopted to represent the global membrane and bending response of the shell structures while keeping the model size suitable for the nonlinear contact analyses.

The support members were meshed as beam elements along the construction lines connecting the cryostat body to the thermal shields. In the final model, each support member was represented by one BEAM188 element between its cryostat-side and thermal-shield-side endpoints. This discretization was adopted because the supports were straight members with uniform circular sections and the objective was member-level load transfer rather than detailed stress gradients along the support length, one beam element per support was considered sufficient for the global comparison performed in this study.

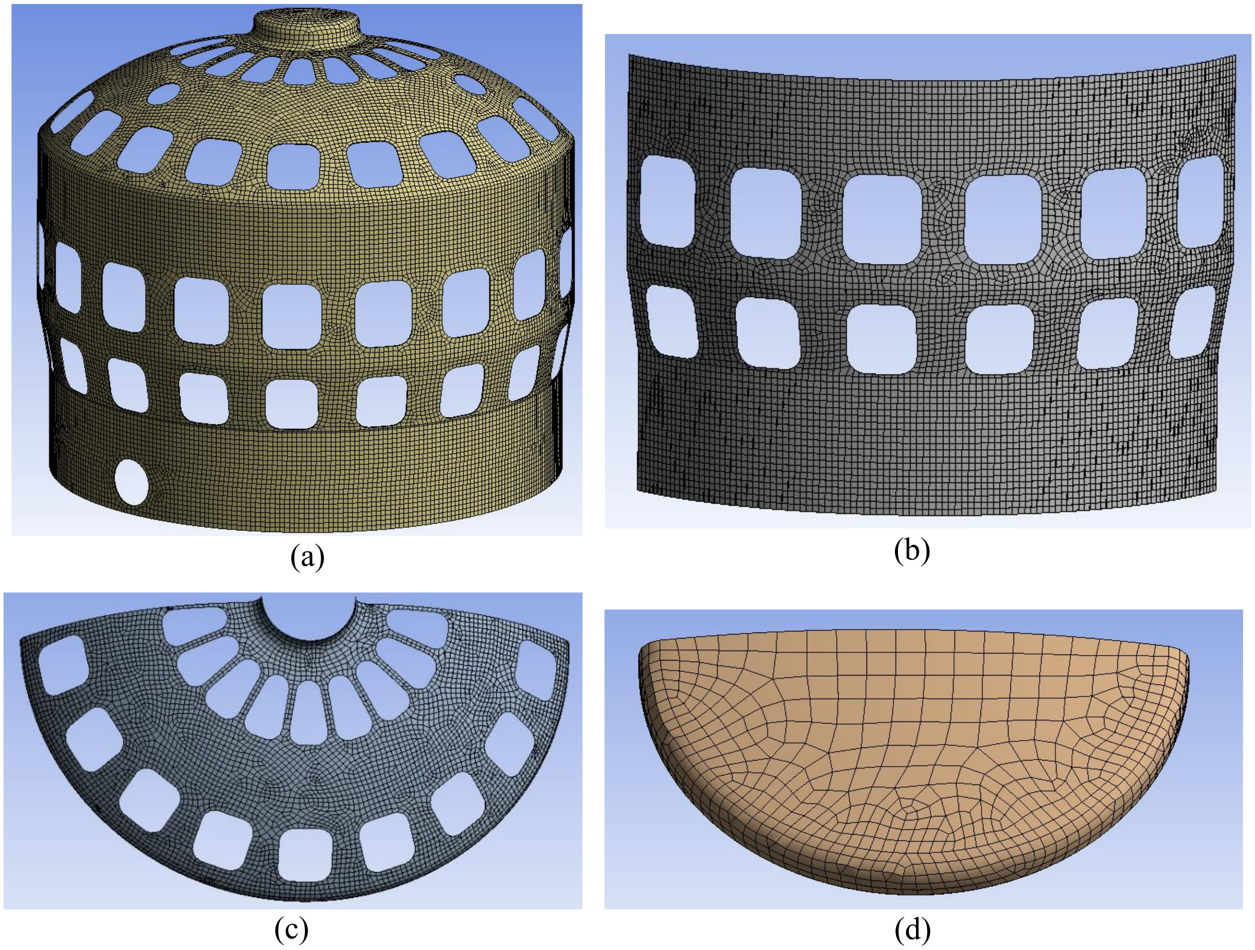

Figure 3.11 Finite element mesh adopted for: (a) cryostat body, (b) cylindrical thermal shield, (c) dome thermal shield, and (d) top-cover thermal shield.

The final mesh definition was used consistently for the gravity, thermal, combined loading, and eigenvalue buckling analyses of the reference configuration.

3.9 Insulation-Gap Preservation Assessment

Preservation of the insulation gap between the cryostat body and the thermal shields is one of the functional requirements of the support system. This gap provides the clearance between the warm cryostat structure and the thermal shields and may be reduced by deformation caused by gravity loading, thermal contraction, or their combined effect.

The insulation gap was evaluated using gap results obtained from the frictionless contact interfaces defined between the facing cryostat and thermal-shield surfaces. These interfaces were not introduced as structural support paths. They were used to monitor the relative separation between the cryostat body and the thermal shields during the analyses.

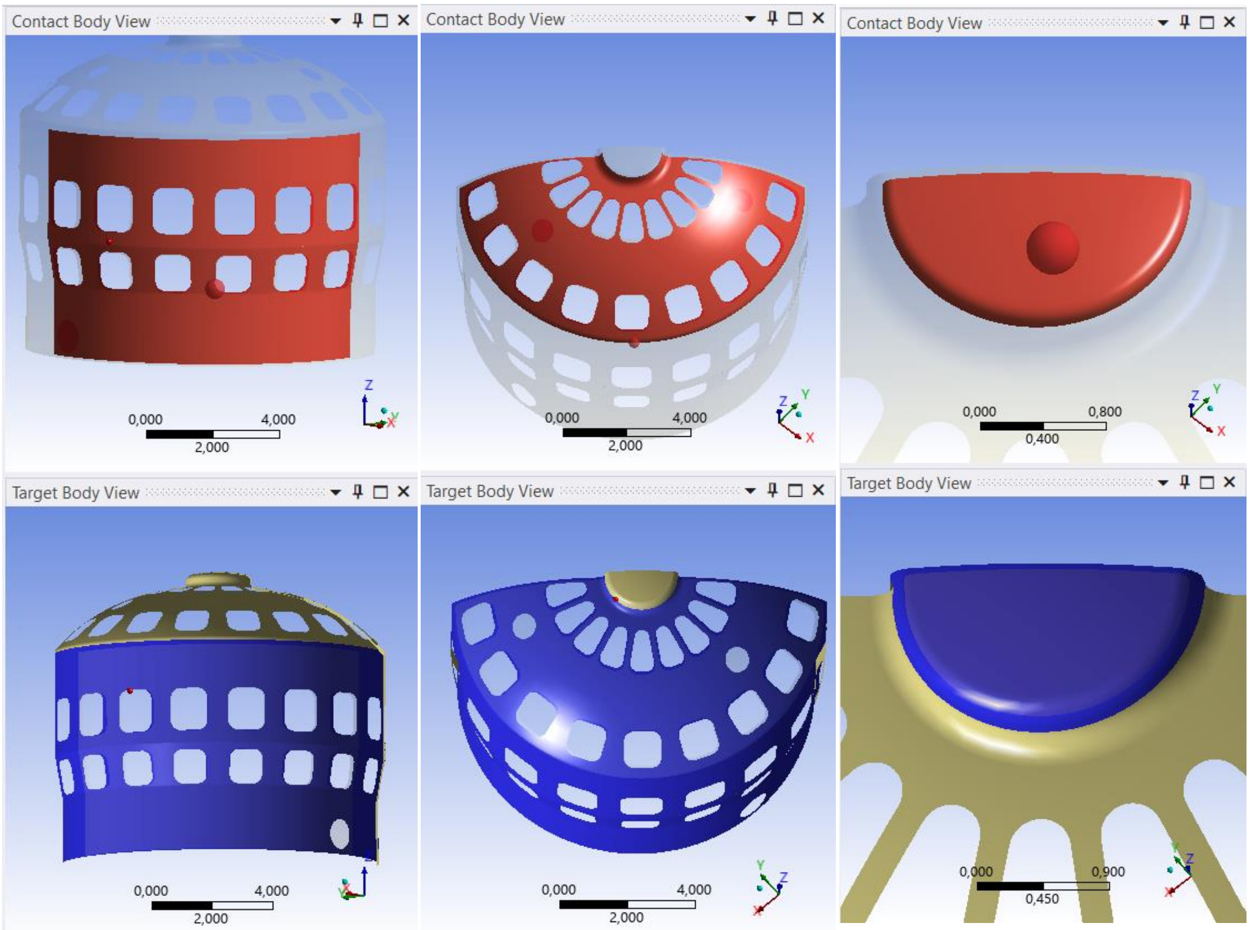

(a) (b) (c)

Figure 3.12 Frictionless contact interfaces used to monitor the insulation gap between cryostat body and (a) cylindrical thermal shield, (b) dome thermal shield, and (c) top-cover thermal shield.

Before applying the structural loads, the initial gap field was extracted for each thermal shield region. These initial fields were used as reference distributions for the cylindrical, dome, and top-cover thermal shields. The gap assessment was then performed by comparing the deformed gap field from each loading case with the corresponding initial gap field. In this way, the evaluation was based on the change in available clearance rather than on a single average gap value. The initial gap fields used for this comparison are reported in Appendix B.

3.10 Structural Assessment Quantities

The structural response of the thermal shield support system was evaluated using quantities extracted from the finite element analyses. The evaluation focused on shell stresses, support-member stresses, support-member forces and moments, deformation of the thermal shields, and preservation of the insulation gap between the cryostat body and the thermal shields.

For the cryostat and thermal shield shells, equivalent von Mises stress distributions were used to identify the most highly loaded regions and to compare the response under the different loading cases. The equivalent von Mises stress combines the normal and shear stress components into a single scalar quantity [33], written as:

$$\sigma_{VM} = \sqrt{\frac{1}{2}[(\sigma_x - \sigma_y)^2 + (\sigma_y - \sigma_z)^2 + (\sigma_z - \sigma_x)^2] + 3(\tau_{xy}^2 + \tau_{yz}^2 + \tau_{zx}^2)} \qquad (3.3)$$

where σ_{VM} is the equivalent von Mises stress, σ_x, σ_y, and σ_z are the normal stress components, and τ_{xy}, τ_{yz}, and τ_{zx} are the shear stress components.

For the G10-CR support members, the stress evaluation was based on beam stress results. Direct stress was used to evaluate the axial-stress contribution, while combined stress was used as the main beam-level stress quantity because it includes both axial and bending contributions.

For a beam member, the combined normal stress may be interpreted as the superposition of axial and bending stresses [30], written as:

$$\sigma_{comb} = \frac{N}{A} \pm \frac{M_y c_z}{I_y} \pm \frac{M_z c_y}{I_z} \qquad (3.4)$$

where σ_{comb} is the combined normal stress, N is the axial force, A is the cross-sectional area, M_y and M_z are the bending moments about the local beam axes, I_y and I_z are the corresponding second moments of area, and c_y and c_z are the distances from the neutral axis to the evaluated section point.

Since the support members have circular cross-sections, the bending contribution may also be interpreted in simplified form as:

$$\sigma_{comb} = \frac{N}{A} \pm \frac{M_b c}{I} \tag{3.5}$$

where M_b is the resultant bending moment, c is the outer-fiber distance, and I is the second moment of area of the circular section.

For the stainless steel 316LN shell structures, the equivalent von Mises stresses were compared with a selected reference strength of 280 MPa taken from the ITER material design limit data [24]. This comparison was used as a first-level stress check for the shell structures and was not treated as a formal code-compliance verification.

For the support-member strength check, the calculated combined beam stresses were compared with a selected G10-CR reference flexural strength of 345 MPa [34]. This value corresponds to the lower crosswise flexural strength reported in the adopted G10-CR product data. It was selected instead of higher direction-dependent cryogenic strength values because the present beam model does not include laminate orientation or composite failure criteria. The comparison was therefore limited to a support-level strength check and was not treated as a formal composite-material failure verification.

Axial force, shear force, and bending moment were also monitored for the support members. These quantities were not used as acceptance criteria. They were used to interpret how loads were transferred through the support system and to identify whether the support response was governed mainly by axial loading, transverse shear, or bending.

The deformation response was evaluated using directional and total displacement quantities. In the gravity loading case, vertical displacement was used to assess sagging of the thermal shields under self-weight. A practical deformation check was adopted for the gravity-loading case, with the objective of keeping the vertical deformation below 10 mm in the absence of thermal loading. This value was used only for the gravity loading case and was not applied to the thermal or combined loading cases.

For the thermal and combined loading cases, total deformation was considered in order to describe the overall displacement field associated with differential thermal contraction. The total deformation was calculated from the displacement components as:

$$u_{tot} = \sqrt{u_x^2 + u_y^2 + u_z^2} \tag{3.6}$$

where u_{tot} is the total deformation, and u_x, u_y, and u_z are the displacement components along the global coordinate directions.

Insulation-gap preservation was evaluated from the gap results of the frictionless contact interfaces. The gap fields were interpreted relative to their initial distributions, because the sign of the reported gap depends on the contact-normal direction and contact definition. The purpose was to check whether the monitored clearance moved toward local closure during the analyzed loading cases. The principal response quantities used in the present study are summarized in Table 3.9.

Table 3.9 Structural response quantities used in the present study.

Response quantity	Purpose
Equivalent shell stress	Evaluation of structural stress levels within the thermal shields
Direct stress in support members	Evaluation of the axial-stress contribution in the support members
Combined stress in support members	Beam-level stress evaluation including axial and bending contributions
Axial force in support members	Monitoring of load transfer along the support-member axis
Shear force in support members	Monitoring of transverse load transfer through the support members
Bending moment in support members	Monitoring of flexural demand in the support members
Vertical displacement under gravity loading	Evaluation of gravitational sagging behavior
Total deformation	Evaluation of the overall deformation field under thermal and combined loading
Insulation gap	Assessment of gap preservation by comparing initial and deformed gap-result fields.

3.11 Eigenvalue Buckling Analysis

A linear eigenvalue buckling analysis was performed to obtain a first-level estimate of the stability behavior of the thermal shield. This check was included because the thermal shields are thin shell components supported by discrete support members, and local or global instability may occur before the stress level alone becomes critical.

In ANSYS Mechanical, eigenvalue buckling analysis is performed through a linear perturbation procedure linked to a preceding Static Structural analysis. The preceding static solution provides the prestressed restart state of the structure, while the buckling step evaluates the load multipliers and corresponding mode shapes associated with the linearized stability problem.

In the present model, the prestress environment was classified by ANSYS as nonlinear-based. Therefore, the calculated eigenvalue multiplier does not directly represent the total buckling load divided by the upstream static load. Instead, the total buckling load state is interpreted as the restart load state plus the eigenvalue multiplier multiplied by the perturbation load [35]:

$$F_{buckling} = F_{restart} + \lambda F_{perturb} \tag{3.7}$$

where $F_{restart}$ is the load state at the prestressed restart point, $F_{perturb}$ is the perturbation load used in the buckling step, and λ is the eigenvalue buckling load multiplier.

For the gravity-prestressed buckling analysis, the restart state corresponded to the reference gravity load, and the retained perturbation load pattern also corresponded to the gravity load. Therefore, the total buckling load state was interpreted as 1+λ times the reference gravity load.

Supplementary thermal-perturbation buckling checks were also performed from the thermal-only and combined gravity–thermal restart states. In these checks, a unit thermal perturbation was applied in the buckling branch by changing the thermal-shield temperature from −166°C to −167°C, while keeping the cryostat temperature at 23°C. Since the prestress environment was nonlinear-based, the resulting eigenvalue multipliers scale this additional thermal perturbation and not the full operating thermal field or the complete combined gravity–thermal loading state.

Thermal loading is treated as a non-mechanical load in the ANSYS linear perturbation procedure. For linear perturbation eigenvalue buckling, thermal loads may be applied in the buckling phase by specifying a new temperature; for nonlinear-based analyses, the thermal perturbation is interpreted relative to the restart temperature state [36]. This interpretation was used for the supplementary thermal-only and combined gravity–thermal buckling checks.

In all buckling checks, only the first relevant positive load multiplier was used for the stability assessment. Negative load multipliers were not used as governing indicators because they correspond to instability modes associated with the opposite sense of the applied perturbation load pattern. The associated mode shapes were used only to identify the spatial pattern of the instability mode, not to evaluate physical displacement amplitudes, because eigenmode amplitudes are arbitrary and do not represent actual deformation magnitudes.

The calculated buckling results were interpreted only as preliminary elastic stability estimates. Geometric imperfections, contact-status changes, material nonlinearity, and nonlinear post-buckling behavior were not captured by this analysis [35].

3.12 Chapter Summary

This chapter described the finite element methodology used to evaluate the DTT cryostat thermal shield support system. The cryostat body and thermal shields were represented using shell elements, while the support members were represented using beam elements. The support configuration, contact definitions, joint constraints, boundary conditions, loading cases, meshing strategy, gap assessment method, and eigenvalue buckling procedure were defined.

The methodology was developed to evaluate the global structural behavior of the support system under gravity loading, prescribed thermal loading, and combined gravity and thermal loading. The response quantities defined in this chapter provide the basis for the result interpretation and structural assessment presented in Chapter 4.

Chapter 4

Results and Discussion

4.1 Overview of the Analyses

This chapter presents the finite element results obtained for the cryostat thermal shield support system. The first part of the chapter focuses on the reference configuration defined in Chapter 3, in which all support members were assigned a diameter of 20 mm. The response of this configuration is evaluated under gravity loading, prescribed thermal loading, and combined gravity and thermal loading.

The results are discussed using the response quantities introduced in Section 3.10. For the shell structures, the discussion is based on deformation fields and equivalent stress distributions. For the support members, the interpretation is based on beam-level stresses and monitored internal resultants, including axial force, shear force, and bending moment. The insulation gap between the cryostat body and the thermal shields is assessed by comparing the deformed gap results with the corresponding initial gap fields.

After the reference configuration has been assessed, a mixed-diameter support configuration is considered as a sensitivity study. The comparison with the mixed-diameter configuration is presented after the reference-configuration results.

4.2 Gravity Loading Results for the Reference Configuration

The gravity loading case was analyzed first in order to evaluate the structural response of the reference configuration under self-weight only. No thermal contraction was applied in this load case. The results therefore describe the gravity-induced deformation of the thermal shields, the support reactions and beam stresses, and the corresponding shell stress distributions.

4.2.1 Vertical Deformation

The vertical deformation fields under gravity loading are shown in Figure 4.1.

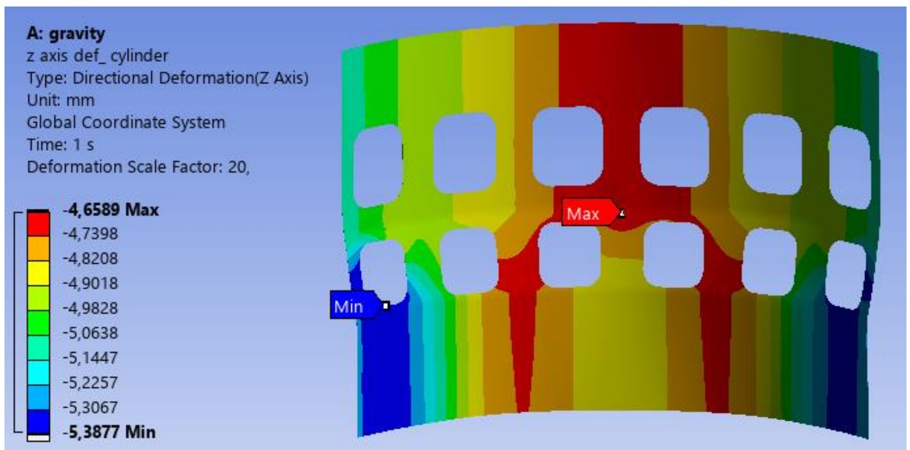

(a)

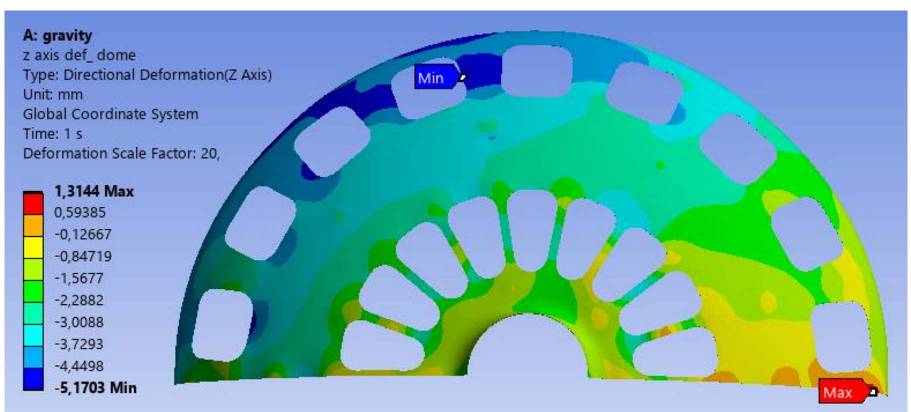

(b)

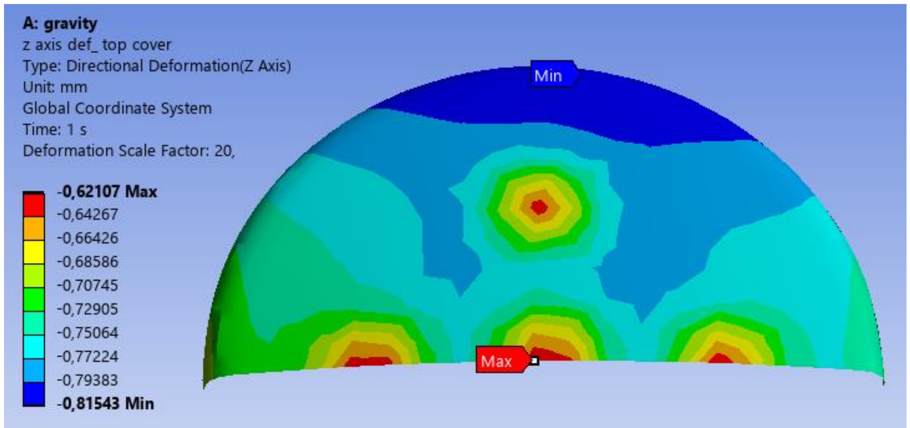

(c)

Figure 4.1 Vertical deformation under gravity loading for the reference configuration: (a) cylindrical thermal shield, (b) dome thermal shield, and (c) top-cover thermal shield.

The deformation results are summarized in Table 4.1. The cylindrical and dome thermal shields showed similar maximum absolute vertical displacements, equal to 5.3877 mm and 5.1703 mm, respectively. The top-cover thermal shield showed a much smaller vertical displacement, with a maximum absolute value of 0.8154 mm. All three values were less than the adopted 10 mm gravity-only deformation check.

Table 4.1 Vertical deformation results under gravity loading for the reference configuration.

Thermal shield region	Maximum vertical displacement	Minimum vertical displacement	Maximum absolute vertical displacement
Cylindrical thermal shield	−4.6589 mm	−5.3877 mm	5.3877 mm
Dome thermal shield	+1.3144 mm	−5.1703 mm	5.1703 mm
Top-cover thermal shield	−0.6211 mm	−0.8154 mm	0.8154 mm

4.2.2 Equivalent Stress in the Shell Structures

The equivalent von Mises stress distributions under gravity loading are shown in Figure 4.2.

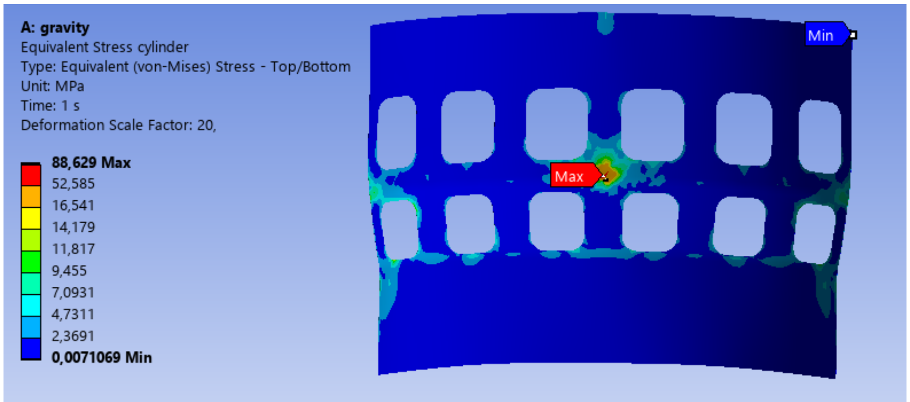

(a)

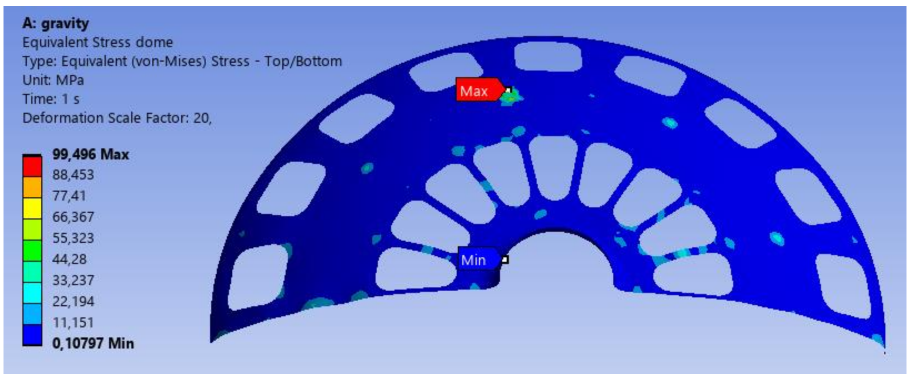

(b)

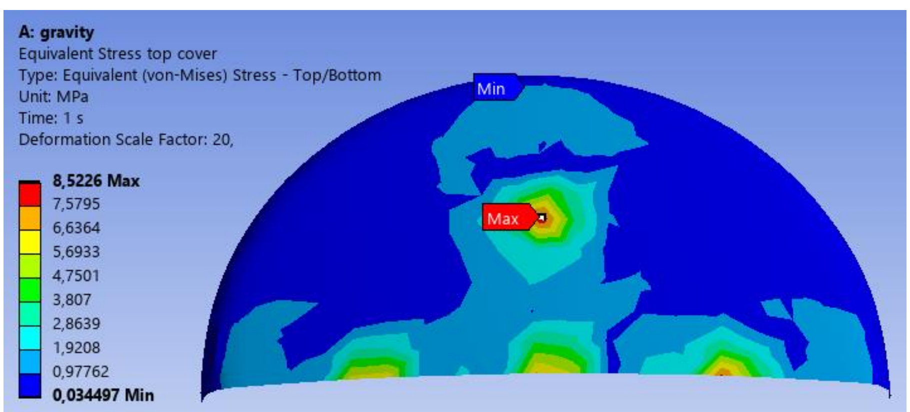

(c)

Figure 4.2 Equivalent von Mises stress under gravity loading for the reference configuration: (a) cylindrical thermal shield, (b) dome thermal shield, and (c) top-cover thermal shield.

The maximum shell stresses are summarized in Table 4.2. The cylindrical thermal shield reached a maximum equivalent stress of 88.629 MPa. The highest stress was located at the bonded support connection region on the thermal-shield side. Although the joint-based supports also contribute to carrying the weight of the cylindrical thermal shield, the bonded support imposes a stronger local restraint because it enforces displacement compatibility between the support endpoint and the shell. The joint-based supports provide selected translational constraints while releasing rotations and selected displacement directions. As a result, they can provide support reaction without imposing the same local bending restraint on the shell.

The dome thermal shield reached the highest shell stress in the gravity loading case, with a maximum value of 99.496 MPa. This maximum was also located at the bonded support connection region, where the support reaction is transferred into the thin shell through a more restrained connection. The top-cover thermal shield reached a much lower maximum stress of 8.5226 MPa, located at a no-separation support connection region. Since this value remained low compared with the cylindrical and dome stresses, the top-cover region was not governing under gravity loading.

The stress concentrations observed near bonded support connections should be interpreted in the context of the global shell-and-beam model. In the model, the support reaction is transferred from a beam endpoint directly into the shell surface, while local attachment details such as bolt heads, washers, pads, weld regions, and contact footprints are not represented. Therefore, the absolute peak stress at the immediate support interface is sensitive to the connection idealization. In the present analysis, these stress peaks are used mainly to identify the most highly loaded regions of the shell model and to compare the response of the different loading cases.

Table 4.2 Maximum equivalent von Mises stress under gravity loading for the reference configuration.

Thermal shield region	Maximum equivalent von Mises stress	Location of maximum stress
Cylindrical thermal shield	88.629 MPa	Bonded support connection region
Dome thermal shield	99.496 MPa	Bonded support connection region
Top-cover thermal shield	8.5226 MPa	No-separation support connection region

4.2.3 Support-Member Forces and Stresses

The support-member force, moment, and stress results under gravity loading are shown in Figures 4.3 and 4.4 and summarized in Table 4.3.

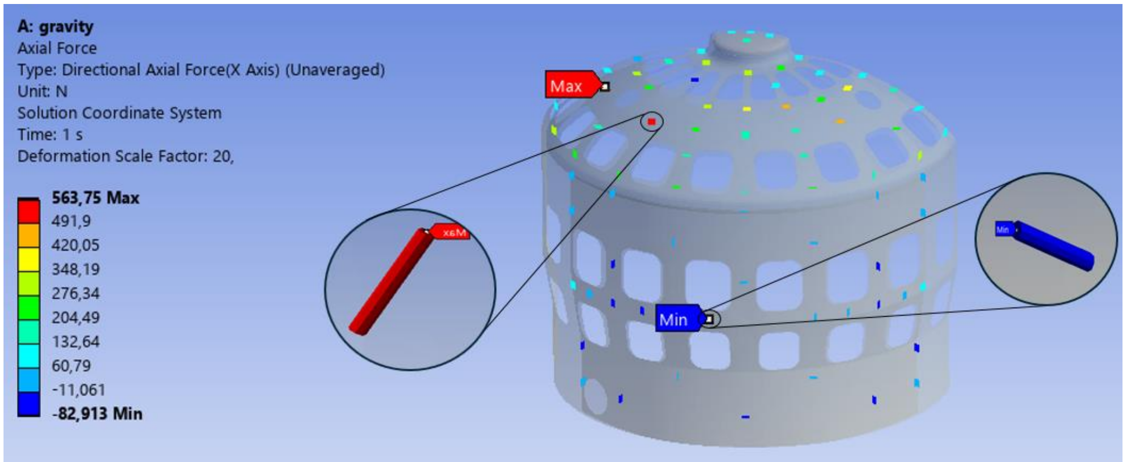

(a)

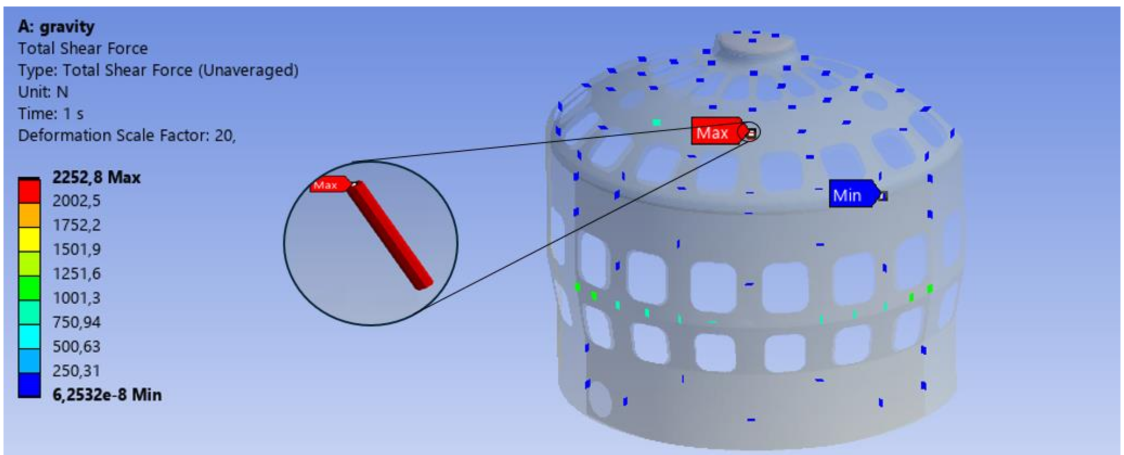

(b)

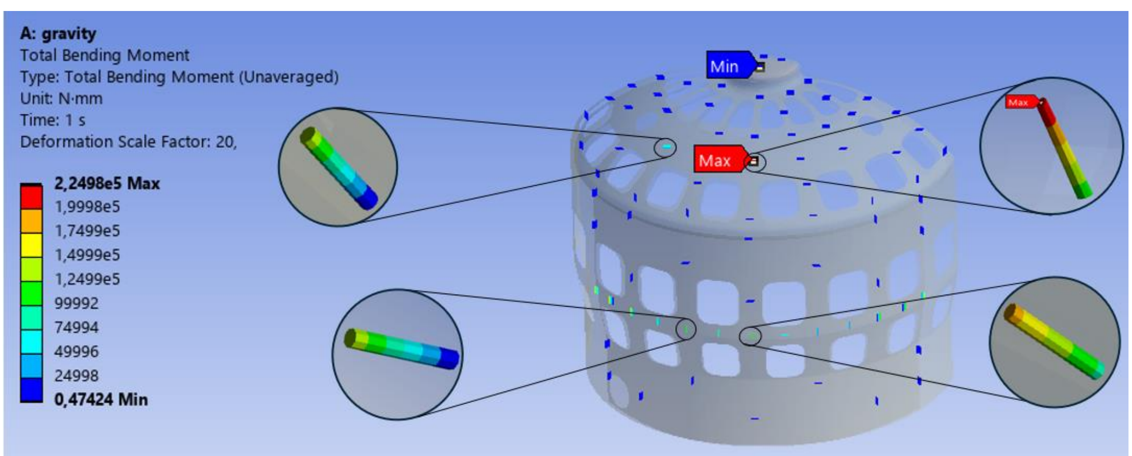

(c)

Figure 4.3 Support-member internal resultants under gravity loading for the reference configuration: (a) axial force, (b) total shear force, and (c) total bending moment.

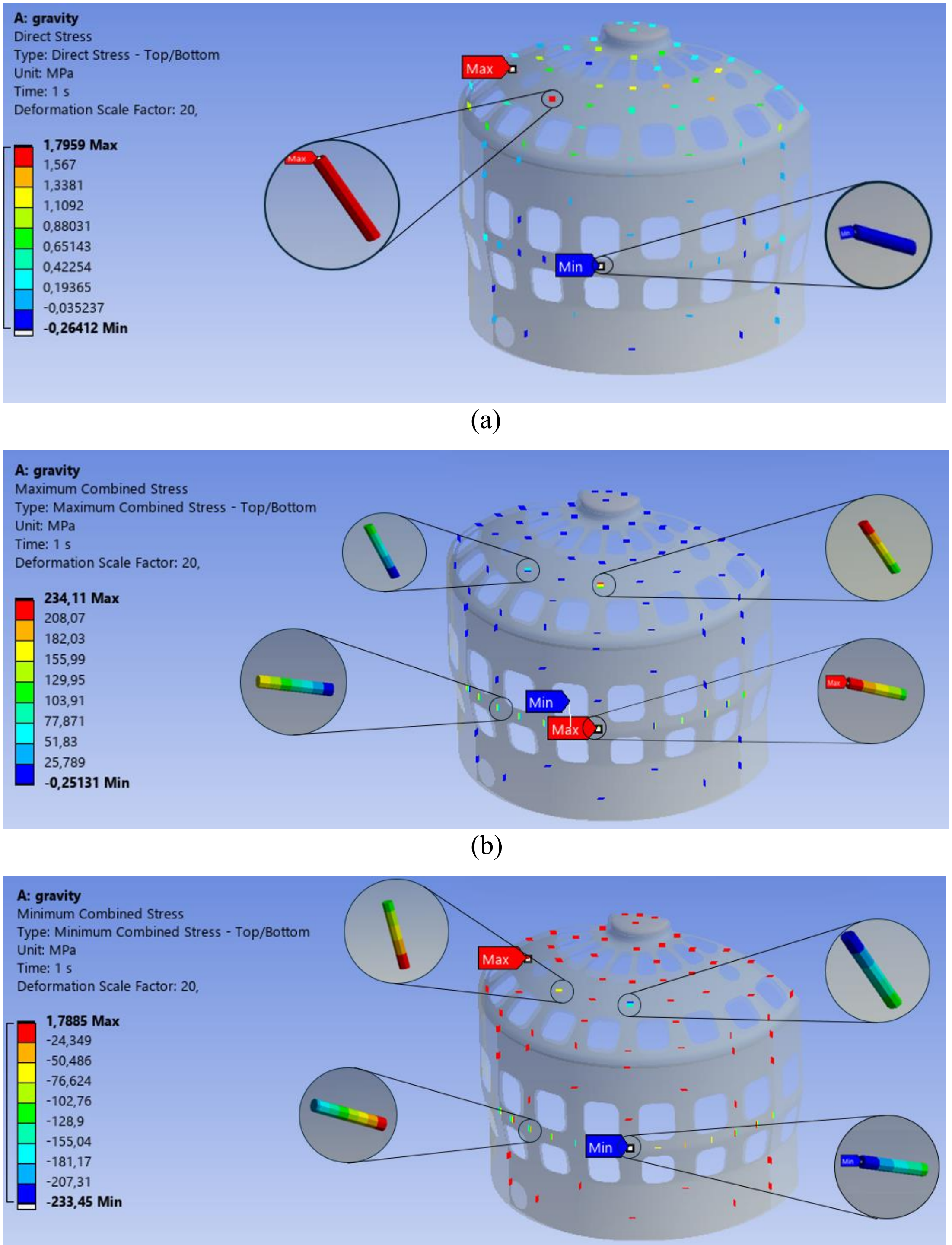

(c)

Figure 4.4 Support-member stress results under gravity loading for the reference configuration: (a) direct stress, (b) maximum combined stress, and (c) minimum combined stress.

The support-member response under gravity loading was bending-dominated. The direct stress remained small, with values between −0.2641 MPa and +1.7959 MPa, while the combined stress reached +234.11 MPa in tension and −233.45 MPa in compression. The maximum total bending moment was 2.2498×10^5 N·mm. This indicates that the governing support-member stress under gravity loading was controlled mainly by bending rather than by axial force. The largest bending moments and the corresponding maximum and minimum combined stresses were located near the support-end attachment to the cryostat surface, as highlighted in the detailed views of Figures 4.3 and 4.4. This distribution is consistent with the support members acting as short beam-like connectors between the thermal shield and the cryostat body. Under transverse reaction forces, the largest bending demand develops near the more restrained end of the member. The maximum and minimum combined stresses therefore represent tensile and compressive outer-fiber stresses generated by the same bending-dominated response, rather than independent axial-stress effects.

Table 4.3 Support-member force and stress results under gravity loading for the reference configuration.

Support-member quantity	Value
Maximum axial force	+563.75 N
Minimum axial force	−82.913 N
Maximum direct stress	+1.7959 MPa
Minimum direct stress	−0.2641 MPa
Maximum total shear force	2252.8 N
Maximum total bending moment	2.2498×10^5 N·mm
Maximum combined stress	+234.11 MPa
Minimum combined stress	−233.45 MPa

4.2.4 Insulation-Gap Result

The insulation-gap result under gravity loading was compared with the corresponding initial gap field described in Section 3.9 and reported in Appendix B. The gap fields obtained after gravity loading are shown in Figure 4.5.

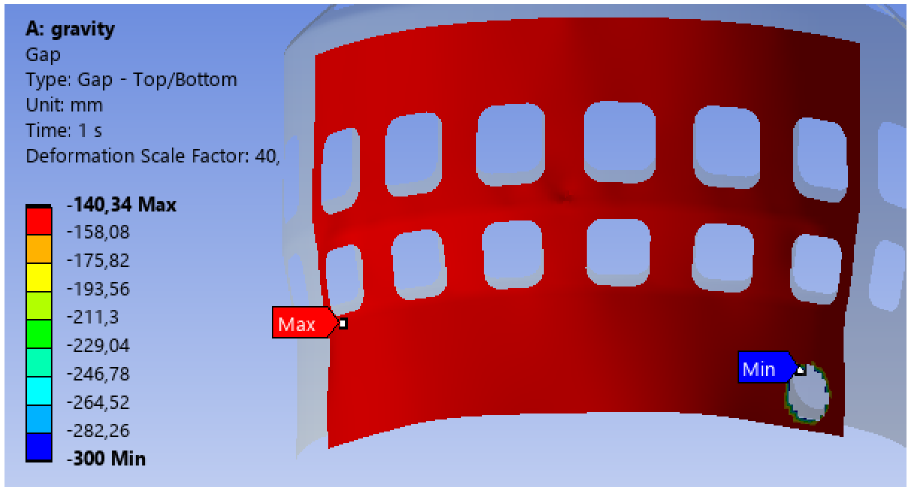

(a)

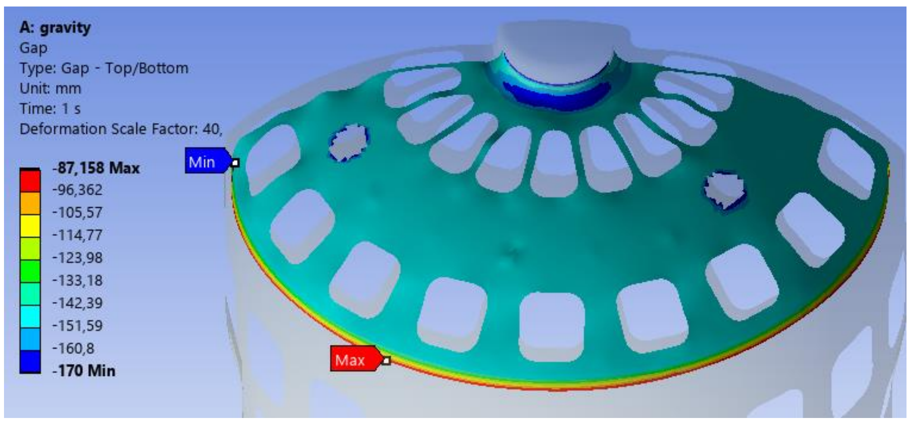

(b)

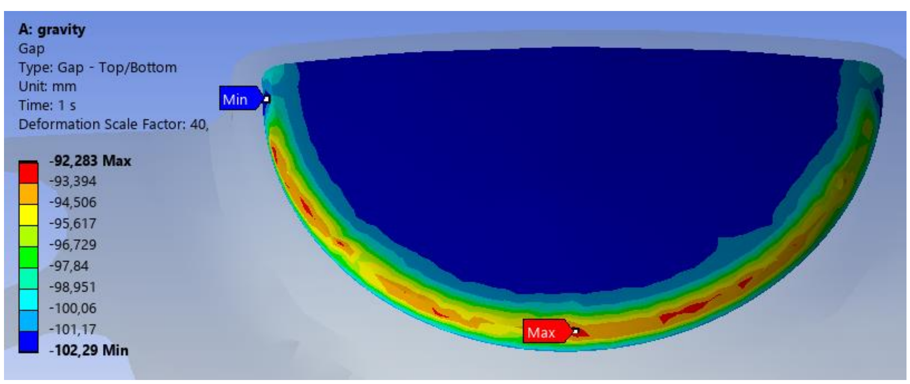

(c)

Figure 4.5 Gap results under gravity loading for the reference configuration: (a) cylindrical thermal shield, (b) dome thermal shield, and (c) top-cover thermal shield.

For the cylindrical thermal shield, the range changed from −142.58 to −300 mm in the initial configuration to −140.34 to −300 mm under gravity loading. A local region with a larger reported gap was observed near one of the lower cut-outs. This behavior was attributed to the cut-out geometry, where the facing contact surfaces and the associated contact-normal directions are less regular than in the main shell area. The feature was therefore treated as a local effect of the gap-result extraction near a geometric discontinuity. Outside this region, the deformed gap field followed the initial gap distribution closely.

For the dome and top-cover thermal shields, the deformed gap ranges also remained close to their initial fields. The gravity loading case therefore did not show local closure of the monitored insulation clearance.

In the following gap-result tables, the sign is determined by the ANSYS contact-normal convention. Therefore, the assessment is based on changes relative to the initial gap field rather than on the algebraic sign of the reported values.

Table 4.4 Comparison between initial and gravity-loading gap-result ranges for the reference configuration.

Thermal shield region	Initial gap-result range	Gap-result range under gravity loading
Cylindrical thermal shield	−142.58 to −300 mm	−140.34 to −300 mm
Dome thermal shield	−91.349 to −170 mm	−87.158 to −170 mm
Top-cover thermal shield	−92.176 to −102.27 mm	−92.283 to −102.29 mm

4.3 Thermal Loading Results for the Reference Configuration

The thermal loading case was analyzed in order to isolate the structural response produced by the prescribed temperature difference between the cryostat body and the thermal shields. Gravity loading was not applied in this case. The results therefore describe the deformation and stress response associated with differential thermal contraction only.

4.3.1 Total Deformation

The total deformation fields under thermal loading are shown in Figure 4.6.

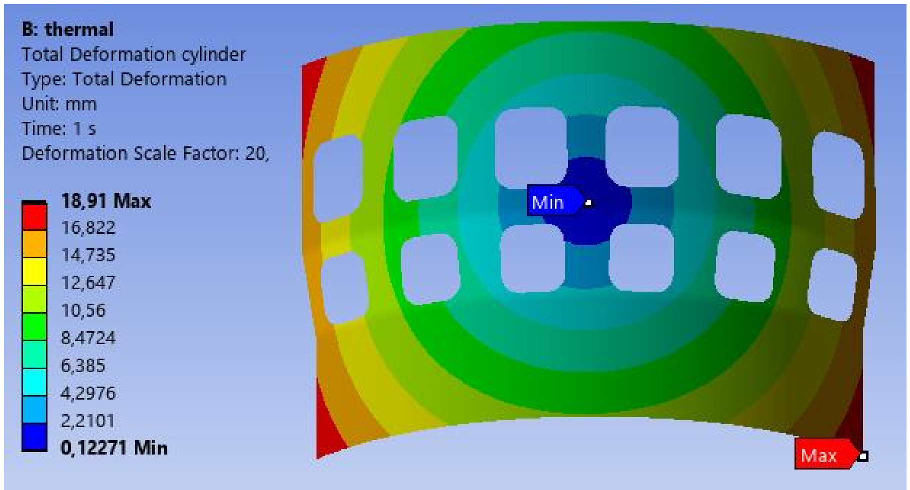

(a)

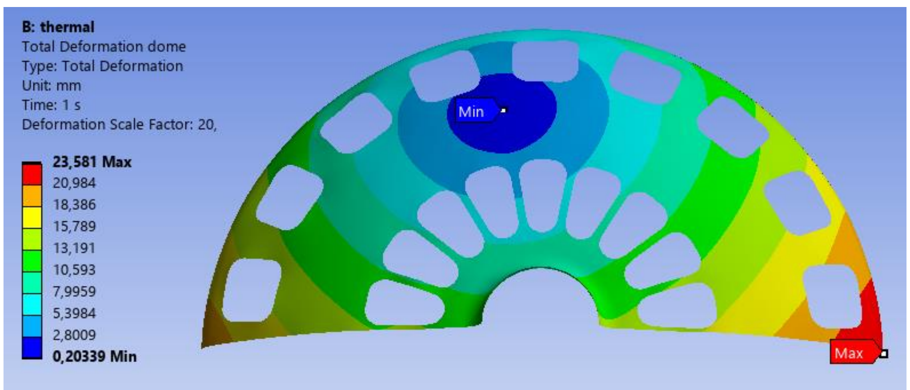

(b)

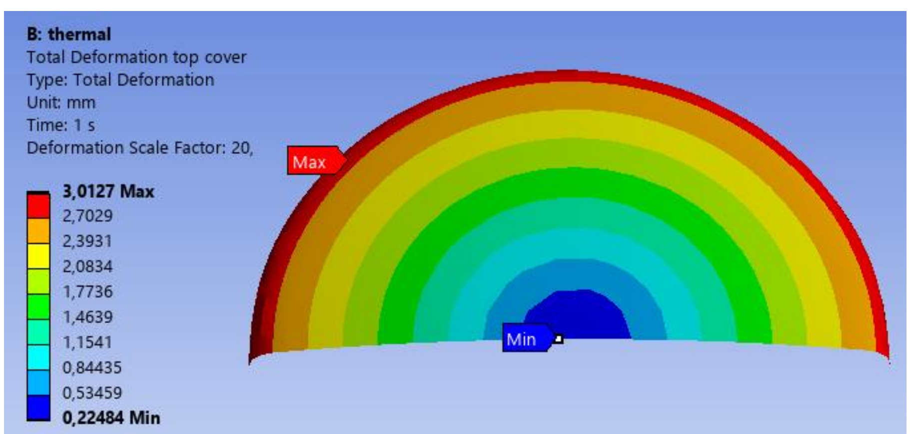

(c)

Figure 4.6 Total deformation under thermal loading for the reference configuration: (a) cylindrical thermal shield, (b) dome thermal shield, and (c) top-cover thermal shield.

The total deformation results are summarized in Table 4.5. The dome thermal shield showed the largest deformation, with a maximum value of 23.581 mm. The cylindrical thermal shield reached

18.91 mm, while the top-cover thermal shield reached 3.0127 mm. The thermal loading case therefore produced larger displacement fields than the gravity case, mainly because the imposed temperature difference caused contraction of the thermal shields relative to the cryostat body.

Table 4.5 Total deformation results under thermal loading for the reference configuration.

Thermal shield region	Minimum total deformation	Maximum total deformation
Cylindrical thermal shield	0.12271 mm	18.91 mm
Dome thermal shield	0.20339 mm	23.581 mm
Top-cover thermal shield	0.22484 mm	3.0127 mm

4.3.2 Equivalent Stress in the Shell Structures

The equivalent von Mises stress distributions under thermal loading are shown in Figure 4.7.

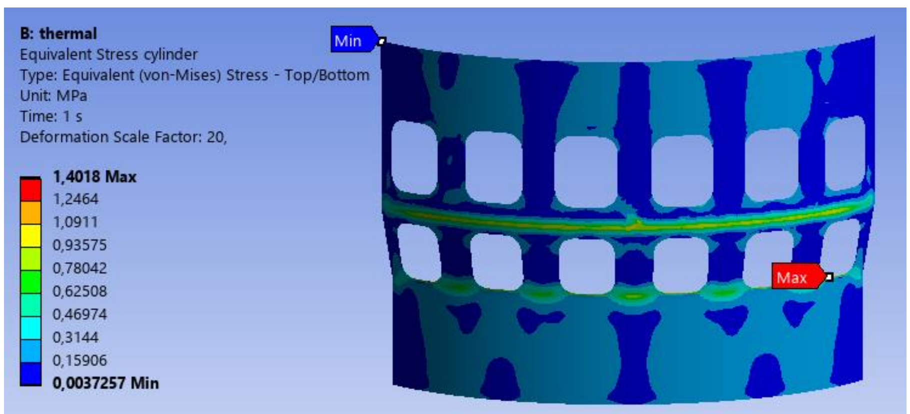

(a)

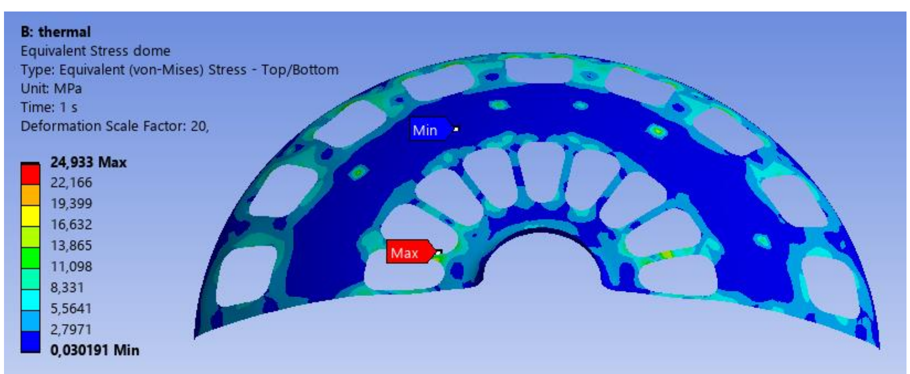

(b)

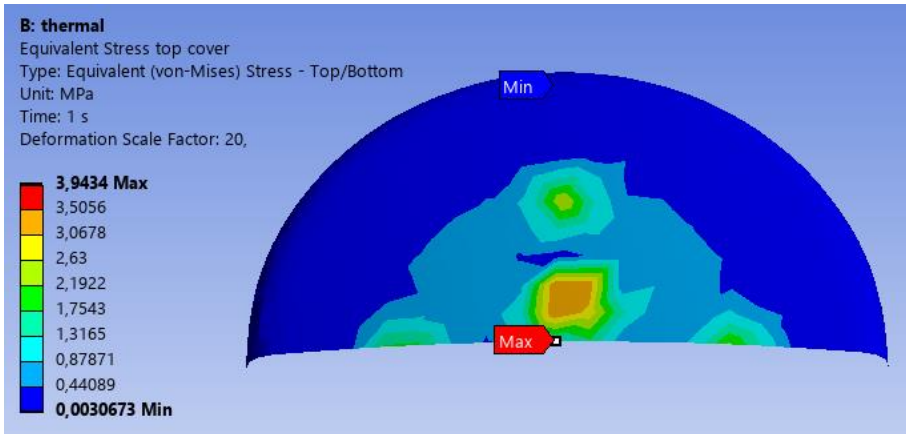

(c)

Figure 4.7 Equivalent von Mises stress under thermal loading for the reference configuration: (a) cylindrical thermal shield, (b) dome thermal shield, and (c) top-cover thermal shield.

The shell stresses under thermal loading are summarized in Table 4.6. The cylindrical thermal shield reached only 1.4018 MPa, indicating that most of the thermal contraction was accommodated without producing significant restraint stress in the cylindrical shell.

The dome thermal shield showed a maximum equivalent stress of 24.933 MPa. Although this value is higher than the thermal stresses obtained in the cylindrical and top-cover regions, it remains much lower than the dome stress obtained under gravity loading. The highest thermal stresses were localized near support connection regions and around some cut-out edges, while most of the dome shell remained at a lower stress level.

This distribution is consistent with restrained thermal contraction of a double-curved shell containing cut-outs. The prescribed temperature field tends to contract the dome shell, but this motion is partly constrained by the support connections and by the surrounding shell continuity. The cut-outs interrupt the membrane stress path and locally alter the effective membrane and bending stiffness of the shell, which is consistent with the general behavior of plates and shells containing openings or cut outs [37]. In addition, some no-separation support locations in the dome were associated with local contact reactions because tangential sliding is allowed, while separation in the local contact-normal direction is prevented. This effect was less evident in the cylindrical thermal shield, where the contraction pattern is more regular. Overall, the thermal load produced localized stress concentrations rather than a uniformly high shell-stress field.

The top-cover thermal shield reached a maximum equivalent stress of 3.9434 MPa and was not governing under thermal loading.

Table 4.6 Maximum equivalent von Mises stress under thermal loading for the reference configuration.

Thermal shield region	Maximum equivalent von Mises stress
Cylindrical thermal shield	1.4018 MPa
Dome thermal shield	24.933 MPa
Top-cover thermal shield	3.9434 MPa

4.3.3 Support-Member Forces and Stresses

The support-member force, moment, and stress results under thermal loading are shown in Figures 4.8 and 4.9 and summarized in Table 4.7.

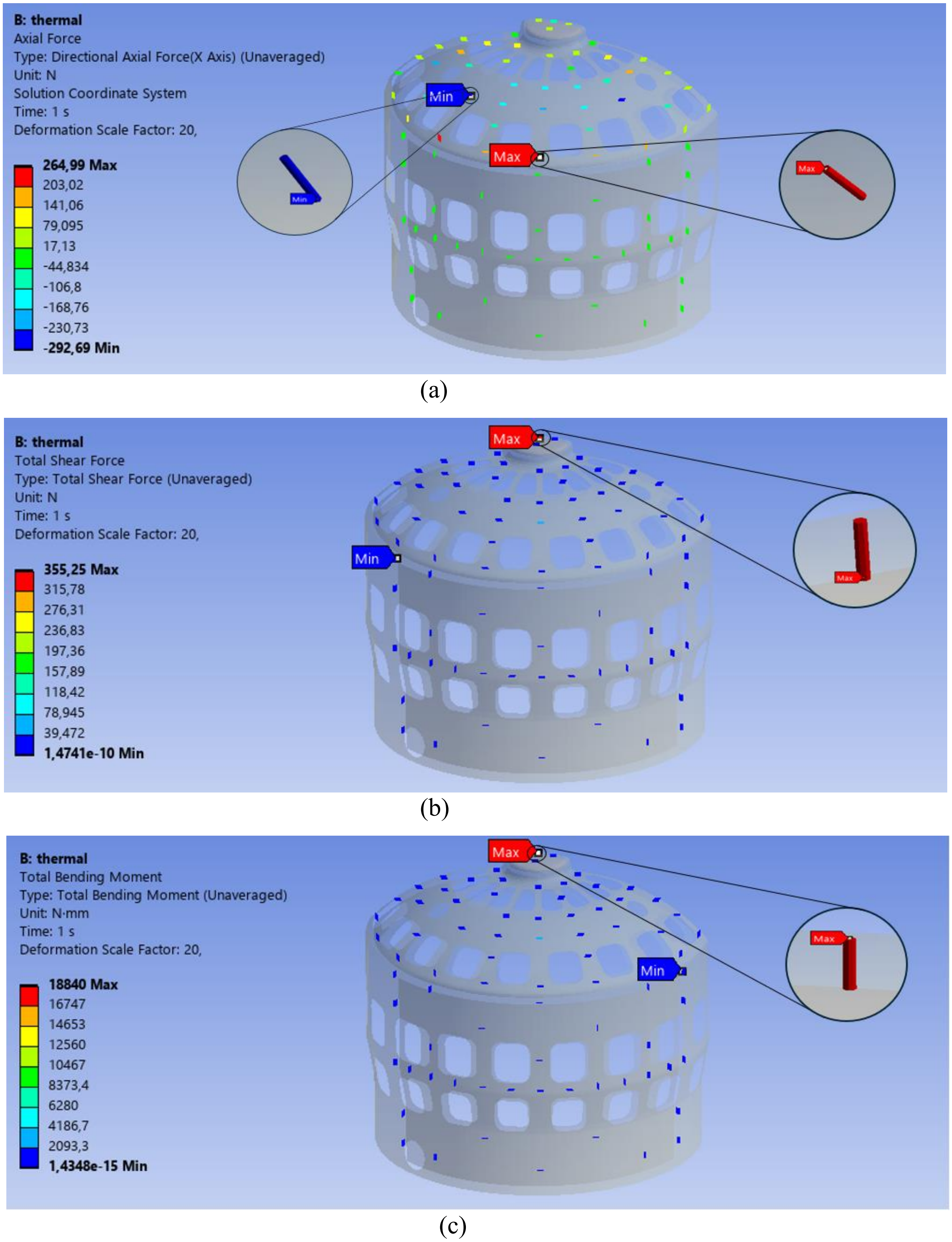

Figure 4.8 Support-member internal resultants under thermal loading for the reference configuration: (a) axial force, (b) total shear force, and (c) total bending moment.

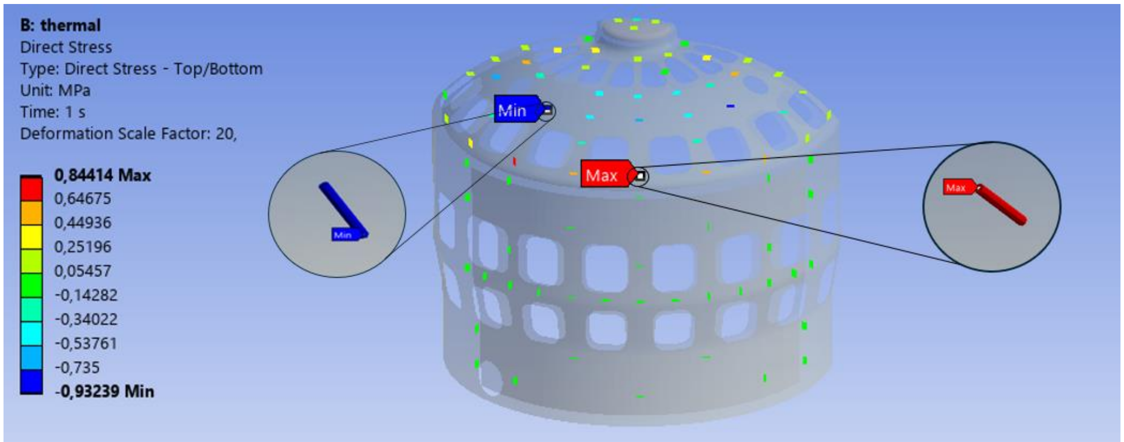

(a)

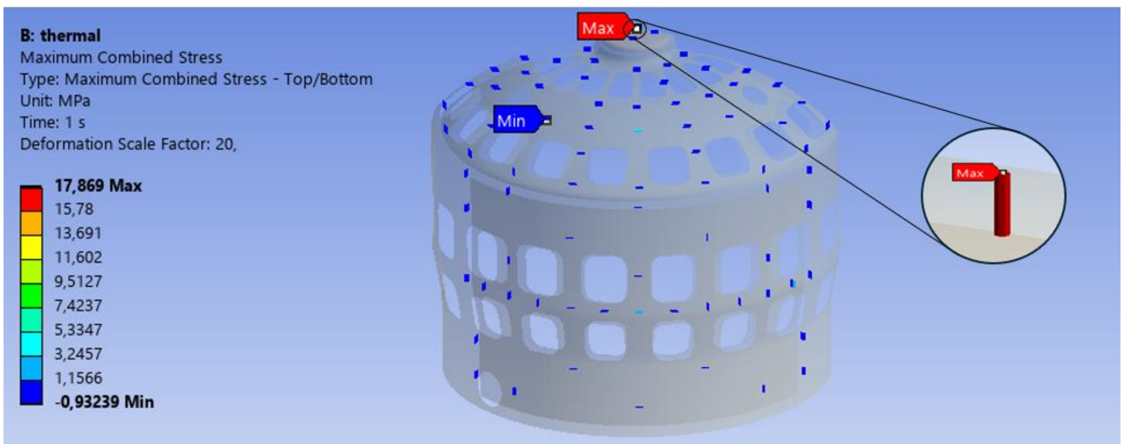

(b)

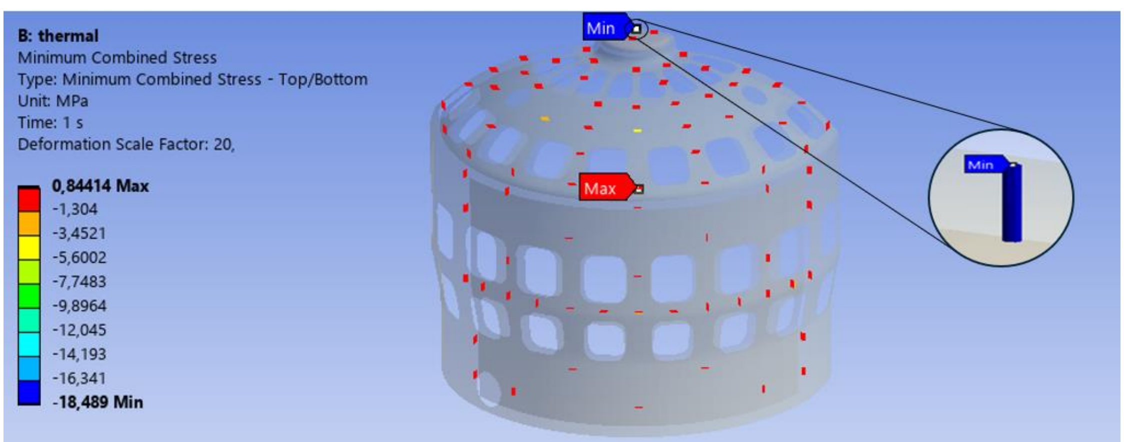

(c)

Figure 4.9 Support-member stress results under thermal loading for the reference configuration: (a) direct stress, (b) maximum combined stress, and (c) minimum combined stress.

The support-member forces and stresses under thermal loading were much lower than the corresponding gravity-loading values. The maximum total shear force was 355.25 N and the maximum bending moment was 18840 N·mm. The combined stress ranged from −18.489 MPa to +17.869 MPa. Therefore, although thermal loading produced larger global displacements of the shields, it did not govern the support-member stress response.

Table 4.7 Support-member force and stress results under thermal loading for the reference configuration.

Support-member quantity	Value
Maximum axial force	+264.99 N
Minimum axial force	−292.69 N
Maximum direct stress	+0.84414 MPa
Minimum direct stress	−0.93239 MPa
Maximum total shear force	355.25 N
Maximum total bending moment	18840 N·mm
Maximum combined stress	+17.869 MPa
Minimum combined stress	−18.489 MPa

4.3.4 Insulation-Gap Result

The gap fields obtained after thermal loading are shown in Figure 4.10 and compared with the corresponding initial gap fields in Table 4.8.

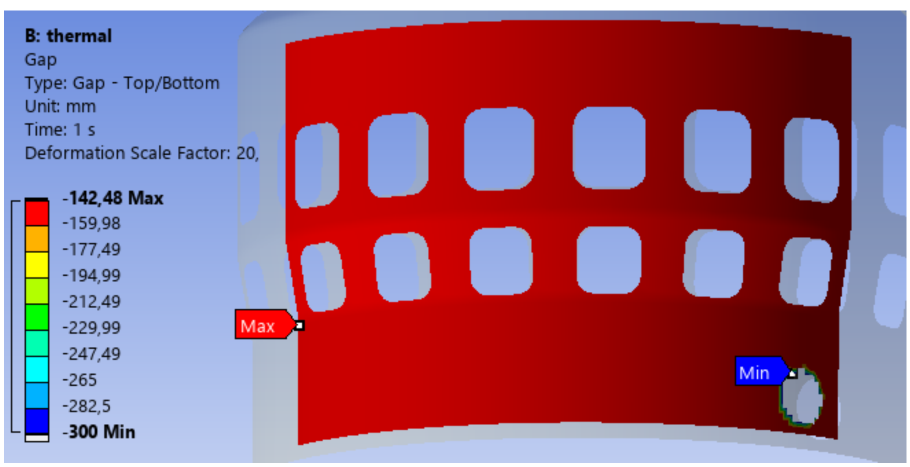

(a)

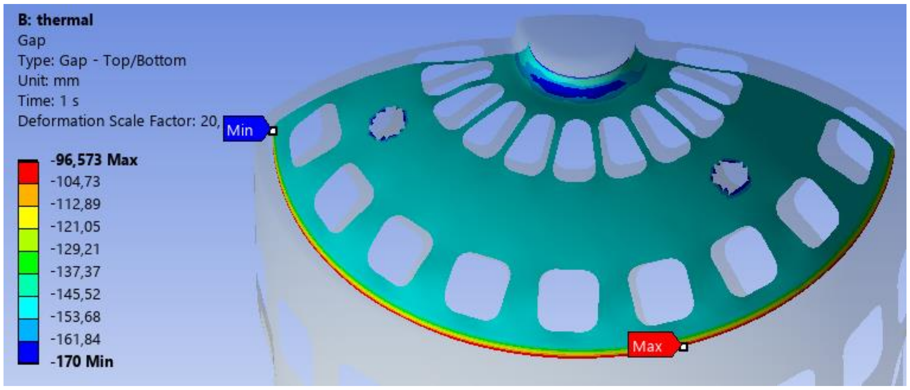

(b)

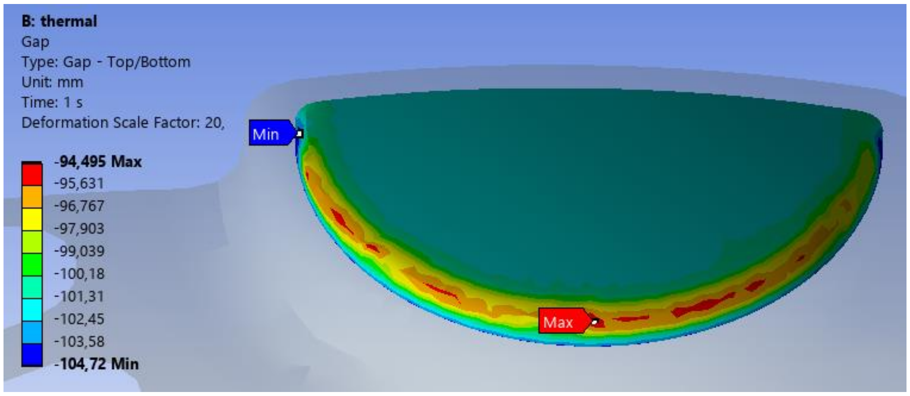

(c)

Figure 4.10 Gap results under thermal loading for the reference configuration: (a) cylindrical thermal shield, (b) dome thermal shield, and (c) top-cover thermal shield.

The cylindrical gap-result range changed only slightly, from −142.58 to −300 mm in the initial configuration to −142.48 to −300 mm under thermal loading. The lower-cut-out region showed the same local reported-gap feature described in Section 4.2.4. The dome and top-cover regions showed larger changes than the cylindrical region, but their deformed gap fields remained consistent with the corresponding initial fields. Overall, the thermal loading case did not show local closure or loss of insulation clearance.

Table 4.8 Comparison between initial and thermal-loading gap-result ranges for the reference configuration.

Thermal shield region	Initial gap-result range	Gap-result range under thermal loading
Cylindrical thermal shield	−142.58 to −300 mm	−142.48 to −300 mm
Dome thermal shield	−91.349 to −170 mm	−96.573 to −170 mm
Top-cover thermal shield	−92.176 to −102.27 mm	−94.495 to −104.72 mm

4.4 Combined Gravity and Thermal Loading Results for the Reference Configuration

The combined loading case includes gravitational acceleration and the prescribed temperature field in the same analysis. This case was used to evaluate the response of the reference configuration when self-weight and differential thermal contraction act simultaneously.

4.4.1 Total Deformation

The total deformation fields under combined gravity and thermal loading are shown in Figure 4.11.

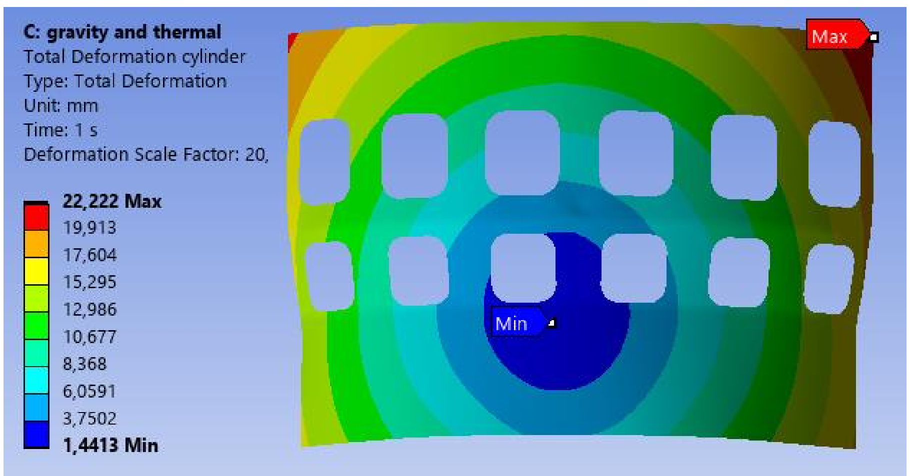

(a)

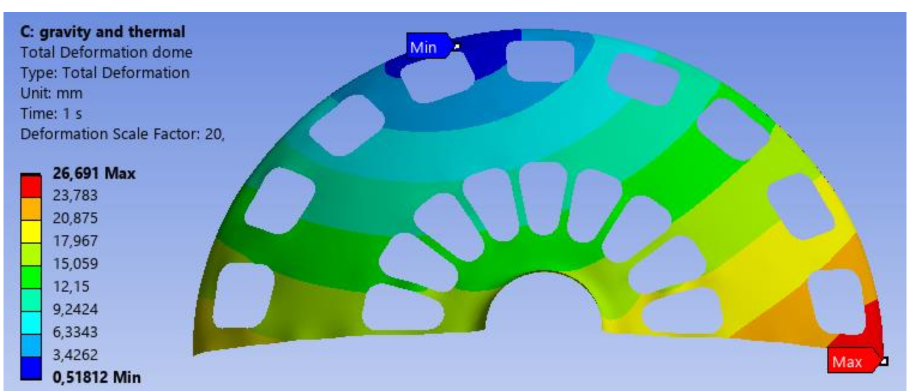

(b)

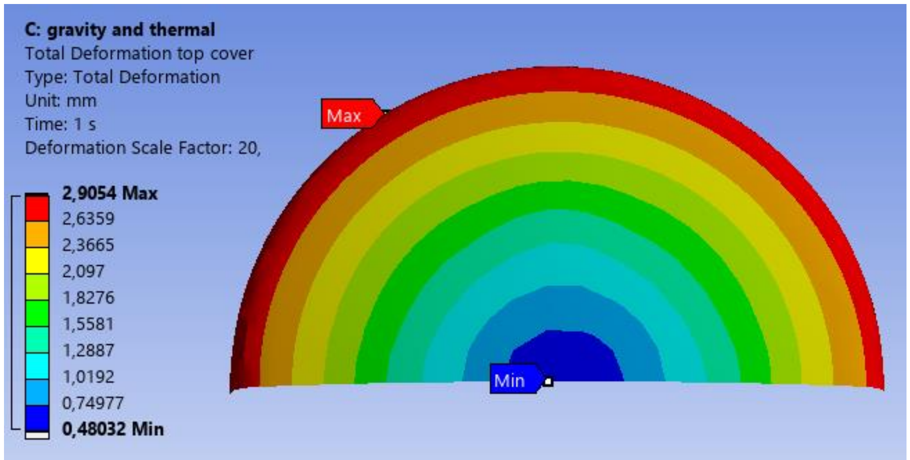

(c)

Figure 4.11 Total deformation under combined gravity and thermal loading for the reference configuration: (a) cylindrical thermal shield, (b) dome thermal shield, and (c) top-cover thermal shield.

The total deformation results are summarized in Table 4.9. The dome thermal shield again showed the largest deformation, reaching 26.691 mm. The cylindrical thermal shield reached 22.222 mm, while the top-cover thermal shield remained much lower, with a maximum total deformation of 2.9054 mm. The combined case therefore followed the same deformation trend as the thermal-only case, showing that the total deformation field was mainly influenced by thermal contraction.

Table 4.9 Total deformation results under combined gravity and thermal loading for the reference configuration.

Thermal shield region	Minimum total deformation	Maximum total deformation
Cylindrical thermal shield	1.4599 mm	22.222 mm
Dome thermal shield	0.51812 mm	26.691 mm
Top-cover thermal shield	0.48032 mm	2.9054 mm

4.4.2 Equivalent Stress in the Shell Structures

The equivalent von Mises stress distributions under combined loading are shown in Figure 4.12.

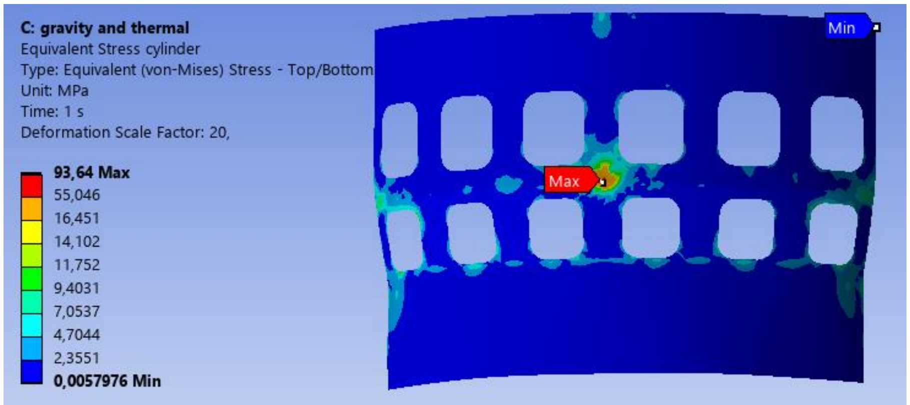

(a)

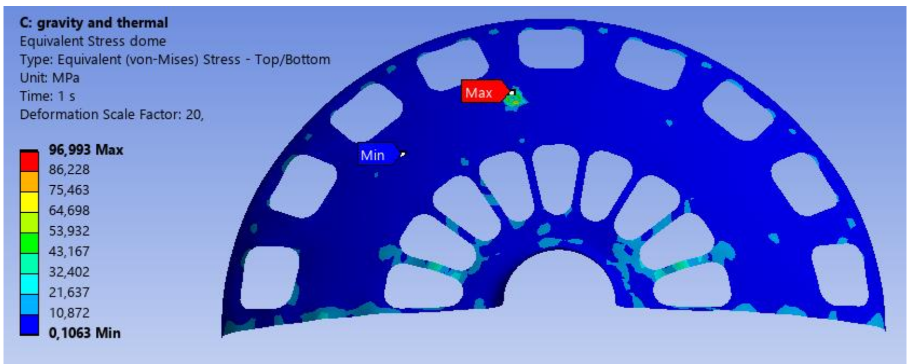

(b)

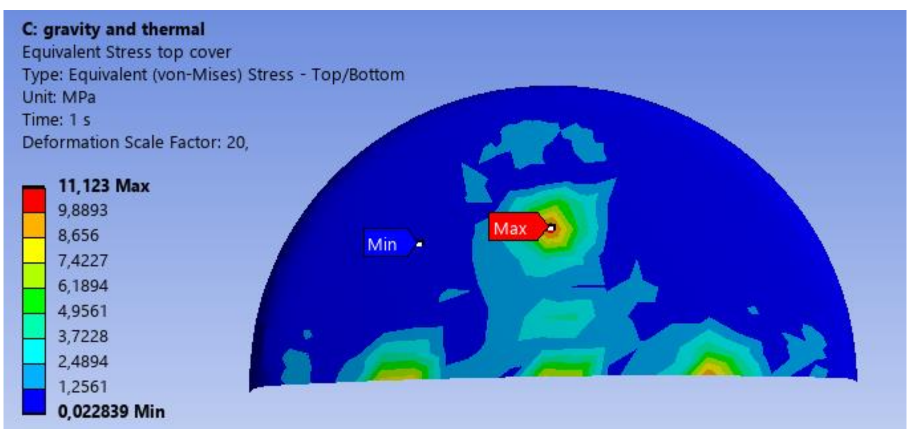

(c)

Figure 4.12 Equivalent von Mises stress under combined gravity and thermal loading for the reference configuration: (a) cylindrical thermal shield, (b) dome thermal shield, and (c) top-cover thermal shield.

The maximum shell stresses are summarized in Table 4.10. The cylindrical thermal shield reached 93.64 MPa, with the highest stress localized near the bonded support connection region. This value is slightly higher than the corresponding gravity-loading stress in the cylindrical thermal shield, indicating that thermal contraction slightly increased the local stress associated with the gravity-induced support reaction in this region.

The dome thermal shield reached 96.993 MPa, which is close to the gravity loading result and much higher than the thermal loading result. The dome shell stress in the combined case was therefore controlled mainly by gravity-induced support loading. The top-cover thermal shield reached 11.123 MPa, which remained low compared with the cylindrical and dome shell stresses.

Table 4.10 Maximum equivalent von Mises stress under combined gravity and thermal loading for the reference configuration.

Thermal shield region	Maximum equivalent von Mises stress
Cylindrical thermal shield	93.64 MPa
Dome thermal shield	96.993 MPa
Top-cover thermal shield	11.123 MPa

4.4.3 Support-Member Forces and Stresses

The support-member force, moment, and stress results under combined loading are shown in Figures 4.13 and 4.14 and summarized in Table 4.11.

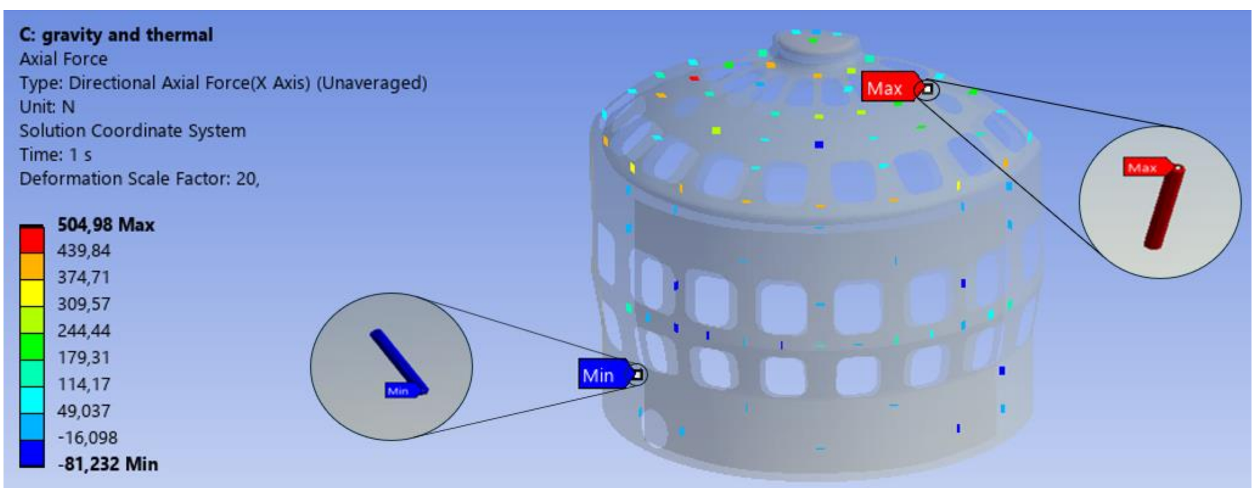

(a)

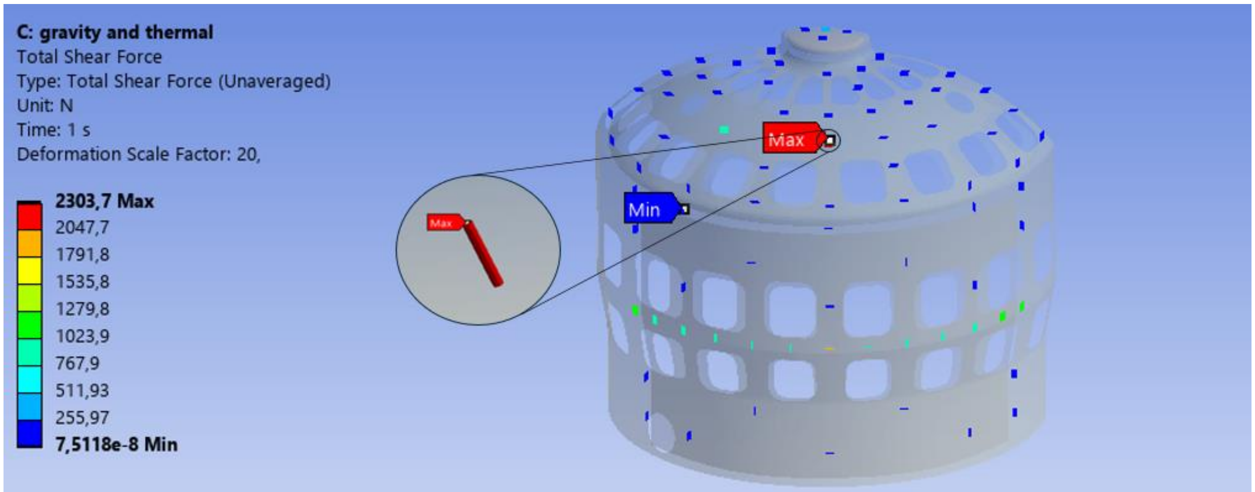

(b)

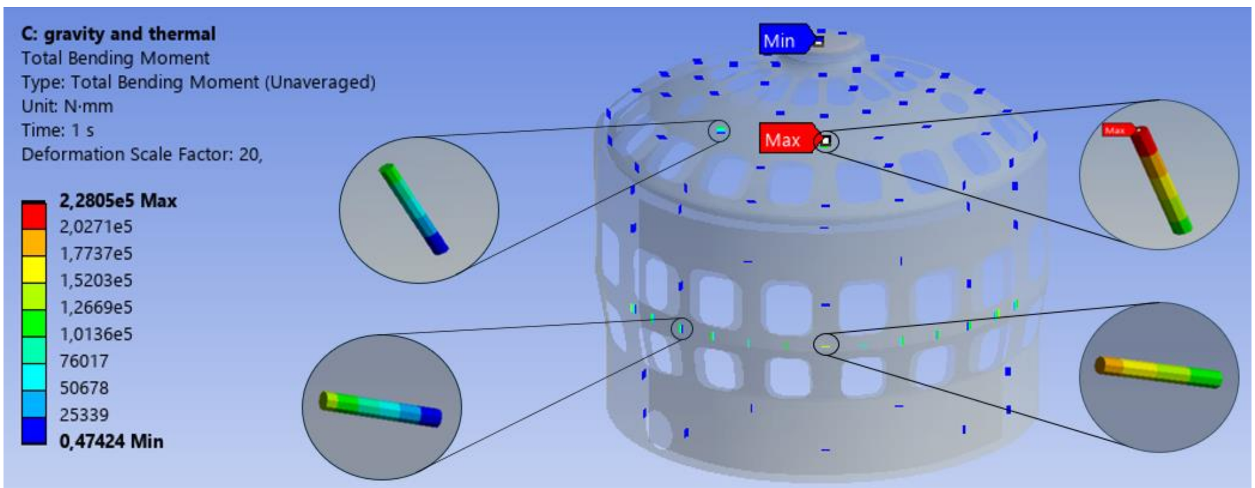

(c)

Figure 4.13 Support-member internal resultants under combined gravity and thermal loading for the reference configuration: (a) axial force, (b) total shear force, and (c) total bending moment.

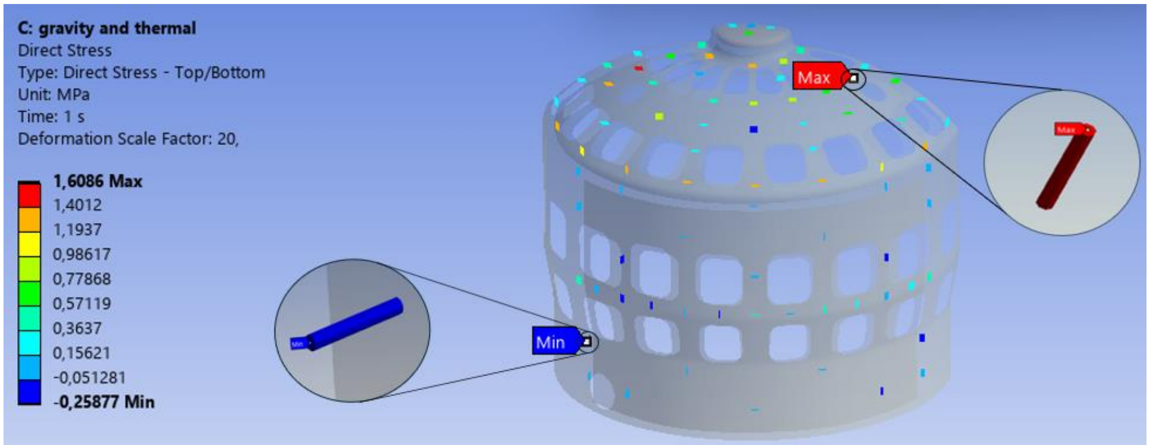

(a)

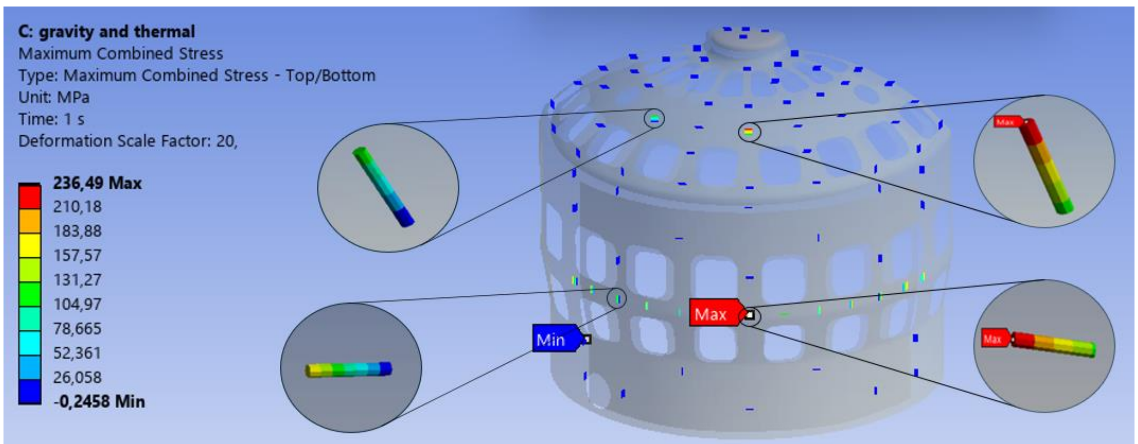

(b)

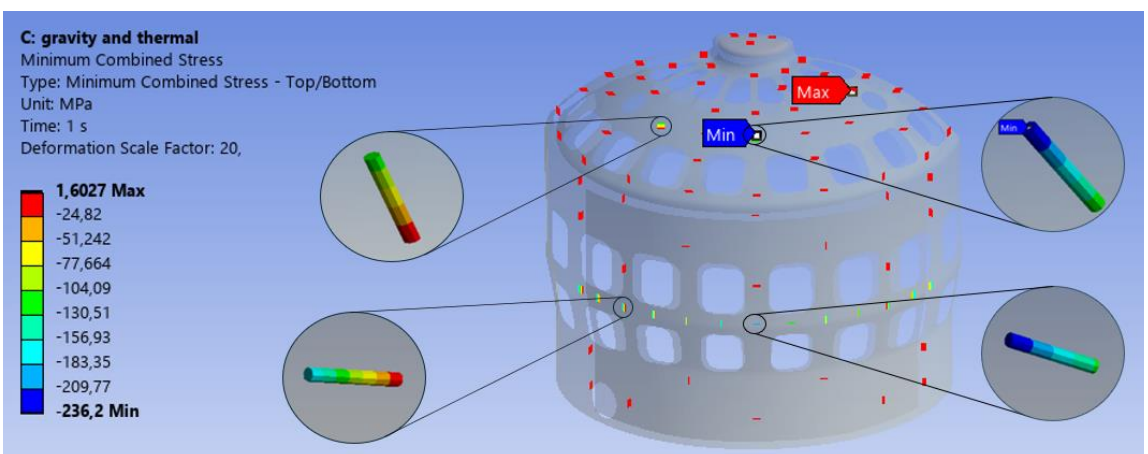

(c)

Figure 4.14 Support-member stress results under combined gravity and thermal loading for the reference configuration: (a) direct stress, (b) maximum combined stress, and (c) minimum combined stress.

The combined loading case produced the largest support-member combined stress. The maximum combined stress was +236.49 MPa and the minimum combined stress was −236.2 MPa. These values are close to the gravity loading combined stress values and much higher than the corresponding thermal values. The maximum bending moment was 2.2805×10^5 N·mm, confirming that the governing support-member stress remained bending-dominated. As in the gravity-loading case, the largest combined stresses were located near the cryostat-side attachment of the most highly loaded support members. The small difference between the gravity- and combined-loading stress values indicates that the thermal contraction slightly modified the support reactions but did not change the main bending-controlled load path of these members.

Table 4.11 Support-member force and stress results under combined gravity and thermal loading for the reference configuration.

Support-member quantity	Value
Maximum axial force	+504.98 N
Minimum axial force	−81.232 N
Maximum direct stress	+1.6086 MPa
Minimum direct stress	−0.2588 MPa
Maximum total shear force	2303.7 N
Maximum total bending moment	2.2805×10^5 N·mm
Maximum combined stress	+236.49 MPa
Minimum combined stress	−236.2 MPa

4.4.4 Insulation-Gap Result

The gap fields obtained after combined loading are shown in Figure 4.15 and compared with the corresponding initial gap fields in Table 4.12.

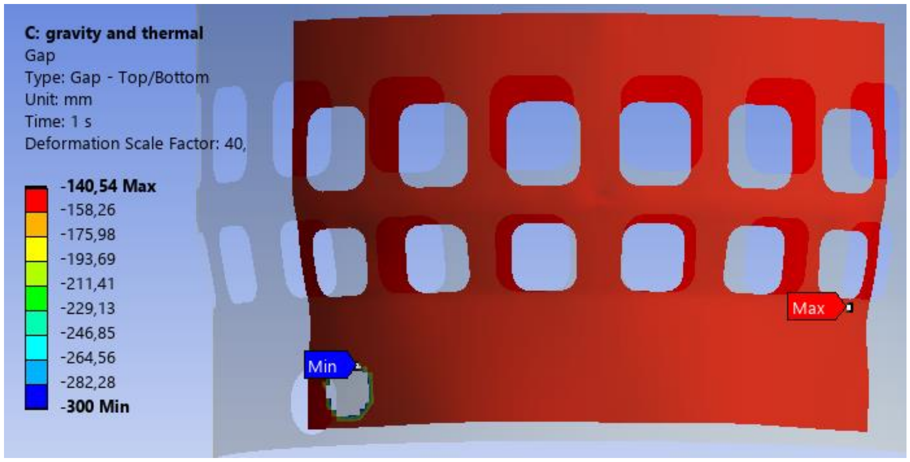

(a)

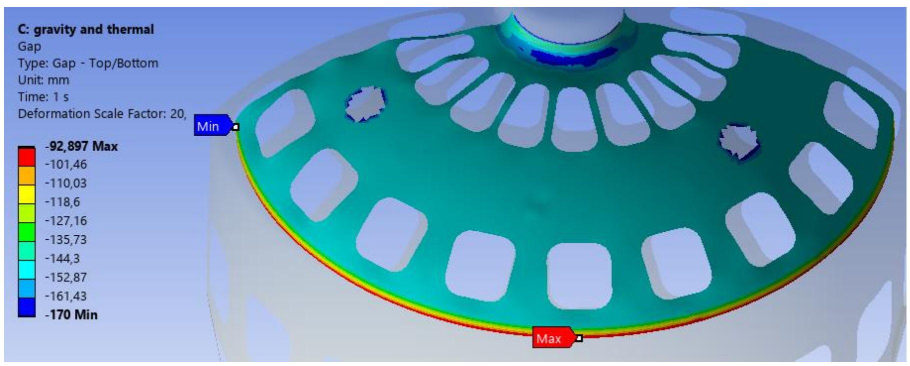

(b)

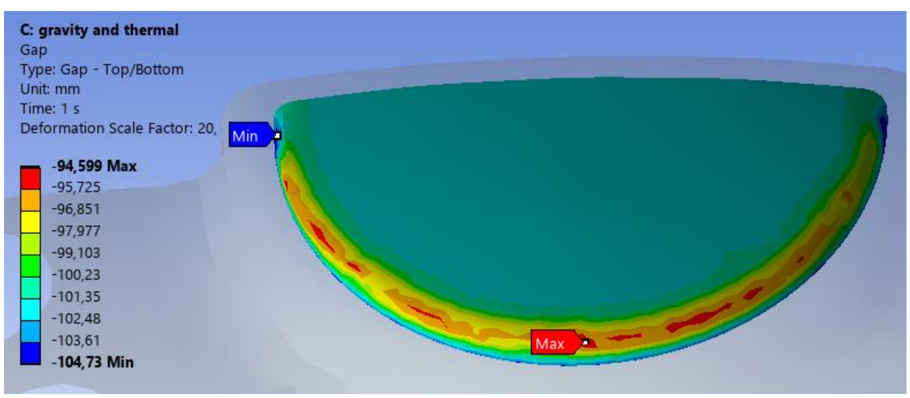

(c)

Figure 4.15 Gap results under combined gravity and thermal loading for the reference configuration: (a) cylindrical thermal shield, (b) dome thermal shield, and (c) top-cover thermal shield.

For the cylindrical thermal shield, the gap-result range changed from −142.58 to −300 mm in the initial configuration to −140.54 to −300 mm under combined loading. The lower-cut-out feature was also present in this case and followed the same interpretation discussed for the gravity-loading result. For the dome and top-cover thermal shields, the deformed gap fields remained close to the corresponding initial fields. Overall, the comparison did not show local closure or loss of insulation clearance under combined gravity and thermal loading.

Table 4.12 Comparison between initial and combined-loading gap-result ranges for the reference configuration.

Thermal shield region	Initial gap-result range	Gap-result range under combined loading
Cylindrical thermal shield	−142.58 to −300 mm	−140.54 to −300 mm
Dome thermal shield	−91.349 to −170 mm	−92.897 to −170 mm
Top-cover thermal shield	−92.176 to −102.27 mm	−94.599 to −104.73 mm

4.5 Eigenvalue Buckling Assessment

The eigenvalue buckling assessment was performed using the procedure defined in Section 3.11. The main buckling check was based on the gravity-prestressed reference configuration. Supplementary checks were also performed from the thermal-only and combined gravity–thermal restart states using a unit thermal perturbation applied to the thermal shields.

The calculated load multipliers for the gravity-prestressed case are summarized in Table 4.13. The first six modes produced negative load multipliers. These modes were not used as governing indicators for the applied gravity perturbation direction, since negative multipliers correspond to instability modes associated with the opposite sense of the perturbation load pattern. The first relevant positive load multiplier was obtained in Mode 7, with a value of 5.2172.

Table 4.13 Eigenvalue buckling load multipliers for the gravity-prestressed reference configuration.

Mode	Load multiplier
1	−7.9334
2	−7.6817
3	−6.9137
4	−6.276
5	−6.034
6	−3.9462
7	5.2172

Since the prestress environment was classified by ANSYS as nonlinear-based, the multiplier of 5.2172 was interpreted as a multiplier of the retained gravity perturbation load. The restart state corresponded to the reference gravity load, and the perturbation load pattern also corresponded to the gravity load. Therefore, the first relevant positive multiplier corresponds to an estimated total buckling load state of:

$$1 + 5.2172 = 6.2172$$

times the reference gravity load.

The first relevant positive mode shape is shown in Figure 4.16. The deformation pattern is localized in a region between the upper openings in the dome thermal shield. This indicates that the lowest positive buckling mode is associated with a local shell instability region rather than a global instability mode of the complete thermal shield system.

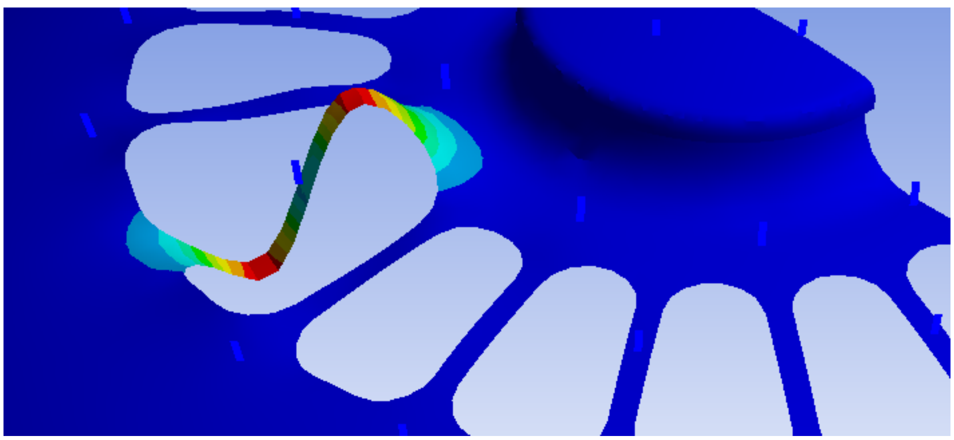

Figure 4.16 First relevant positive eigenvalue buckling mode of the gravity-prestressed reference configuration.

The supplementary thermal-perturbation checks produced first relevant positive multipliers of 2058.9 for the thermal-only restart case and 2078.8 for the combined gravity–thermal restart case. These values scale the imposed unit thermal perturbation, not the full operating thermal field or the complete combined loading state. The high positive multipliers indicate that thermal-perturbation-driven elastic buckling was far from the operating condition within the adopted linear perturbation framework. Therefore, these supplementary checks were used only as supporting evidence and were not interpreted as direct critical-temperature estimates.

Overall, the gravity-prestressed analysis and the supplementary thermal-perturbation checks indicate that elastic buckling was not the governing limitation for the reference configuration within the assumptions of the adopted linear eigenvalue buckling framework.

4.6 Structural Assessment of the Reference Configuration

The reference configuration was assessed using the response quantities defined in Section 3.10. The assessment considered shell stress levels, support-member stress levels, gravity-induced vertical deformation, insulation-gap preservation, and the eigenvalue buckling results.

4.6.1 Shell Stress Assessment

The maximum shell stresses obtained across the analyzed load cases are summarized in Table 4.14. The governing shell stress occurred in the dome thermal shield under gravity loading, with a maximum equivalent stress of 99.496 MPa. The cylindrical thermal shield reached 93.64 MPa, also under combined gravity and thermal loading. The top-cover thermal shield showed much lower stress levels, with a maximum value of 11.123 MPa under combined loading.

Table 4.14 Maximum shell stresses for the reference configuration.

Thermal shield region	Governing load case	Maximum equivalent von Mises stress
Cylindrical thermal shield	Combined	93.64 MPa
Dome thermal shield	Gravity	99.496 MPa
Top-cover thermal shield	Combined	11.123 MPa

Using a selected 316LN reference strength of 280 MPa as defined in Section 3.10, the corresponding stress utilization values remain below unity for all thermal shield regions.

Table 4.15 Shell stress utilization based on the selected 316LN reference strength.

Thermal shield region	Maximum equivalent stress	Reference strength	Utilization
Cylindrical thermal shield	93.64 MPa	280 MPa	0.334
Dome thermal shield	99.496 MPa	280 MPa	0.355
Top-cover thermal shield	11.123 MPa	280 MPa	0.040

The utilization values indicate that the shell stresses were lower than the selected 316LN reference strength for all three thermal shield regions. The highest shell stresses occurred near the support connection regions where restraint and reaction transfer were strongest, especially near the bonded connections in the cylindrical and dome regions. Together with the modeling assumptions discussed in Section 4.2.2, these results were used to evaluate the global shell-stress level of the model.

4.6.2 Support-Member Stress Assessment

The governing support-member stress values obtained across the analyzed load cases are summarized in Table 4.16. The maximum tensile and compressive combined stresses occurred under combined gravity and thermal loading.

Table 4.16 Governing support-member stresses for the reference configuration.

Quantity	Governing load case	Value
Maximum combined stress	Combined	+236.49 MPa
Minimum combined stress	Combined	−236.2 MPa
Maximum direct stress	Gravity	+1.7959 MPa
Minimum direct stress	Thermal	−0.93239 MPa

The support-member stress response was governed by combined stress rather than by direct axial stress. The direct stresses remained below 2 MPa in all load cases, while the maximum absolute combined stress reached 236.49 MPa. This confirms that the governing support-member response was controlled mainly by bending.

For the G10-CR support members, the maximum absolute combined stress was compared with the selected reference flexural strength of 345 MPa as defined in Section 3.10. The resulting utilization is summarized in Table 4.17.

Table 4.17 Support-member stress utilization based on the selected G10-CR reference strength.

Quantity	Maximum absolute stress	Reference strength	Utilization
Combined beam stress	236.49 MPa	345 MPa	0.686

The maximum support-member combined stress gave a utilization of 0.686 relative to the selected G10-CR reference strength. This comparison was used as a support-level strength check. It should not be interpreted as a complete composite-material failure verification, because the support members were represented by equivalent beam elements and detailed laminate-level failure criteria were not included.

4.6.3 Gravity-Induced Deformation Check

The vertical deformation resulting from the gravity-loading case was compared with the practical deformation check of 10 mm. The maximum absolute vertical displacement occurred in the cylindrical thermal shield and was equal to 5.3877 mm. The dome thermal shield reached 5.1703 mm, while the top-cover thermal shield reached 0.8154 mm.

Table 4.18 Gravity-only vertical deformation check for the reference configuration.

Thermal shield region	Maximum absolute vertical displacement	Gravity-only deformation check
Cylindrical thermal shield	5.3877 mm	10 mm
Dome thermal shield	5.1703 mm	10 mm
Top-cover thermal shield	0.8154 mm	10 mm

All three thermal shield regions remained below the 10 mm vertical deformation check in the gravity-loading case.

To further assess the plausibility of the cylindrical thermal shield deformation, the finite element result was compared with the simplified preliminary hand calculation reported in Appendix A. The comparison is summarized in Table 4.19.

Table 4.19 Analytical cross-check of the cylindrical thermal shield gravity-induced deformation.

Quantity	Value
Appendix A hand-calculation displacement	5.11 mm
FE maximum absolute vertical displacement, cylindrical thermal shield	5.3877 mm
Difference relative to hand calculation	5.4%

The hand calculation estimated a support-tip displacement of 5.11 mm, while the finite element model predicted a maximum absolute vertical displacement of 5.3877 mm for the cylindrical thermal shield under gravity loading. The difference between the two values is approximately 5.4%, which indicates good agreement for a simplified analytical estimate. This comparison supports the engineering plausibility of the global gravity-induced deformation predicted by the finite element model. However, it was treated only as an analytical cross-check, not as formal validation, because the hand calculation idealizes the support behavior and does not include shell flexibility, contact behavior, joint constraints, openings, local support-interface effects, or load redistribution within the complete support system.

4.6.4 Insulation-Gap Assessment

The insulation-gap assessment was based on the comparison between the initial and deformed gap fields. Across the three loading cases, the deformed fields remained close to their corresponding initial distributions. The local reported-gap feature near a lower cut-out of the cylindrical thermal shield was attributed to the cut-out geometry and the associated gap-result extraction, as discussed in Section 4.2.4.

The gap comparison did not show local closure or loss of insulation clearance in the reference configuration under gravity, thermal, or combined loading.

4.6.5 Buckling Assessment

The first relevant positive eigenvalue buckling load multiplier was 5.2172 for the gravity-prestressed reference configuration. Since the prestress environment was nonlinear-based and the retained perturbation load pattern corresponded to the reference gravity load, this multiplier corresponds to an estimated total buckling load state of approximately 6.22 times the reference gravity load.

The supplementary thermal-perturbation checks reported in Section 4.5 produced much higher positive multipliers than the gravity-prestressed case, indicating that thermal-perturbation-driven elastic buckling was not close to the operating condition. Therefore, elastic buckling was not identified as the governing limitation for the reference configuration within the adopted linear perturbation framework.

4.6.6 Summary of Reference-Configuration Assessment

The reference configuration met the stress, deformation, gap, and linear buckling checks used in this work. The support-member stresses were governed by bending and reached their maximum under combined gravity and thermal loading, while the largest deformation was mainly associated with thermal contraction. This reference case was therefore used as the baseline for the mixed-diameter comparison.

4.7 Sensitivity Assessment of the Mixed-Diameter Support Configuration

A mixed-diameter support configuration was analyzed as a sensitivity case after the assessment of the reference configuration. The support positions and connection definitions were kept unchanged. The bonded and joint-based supports of the cylindrical thermal shield were kept at 20 mm diameter, and the same criterion was applied to the dome thermal shield. The remaining supports, including the bonded support of the top-cover thermal shield, were assigned a diameter of 10 mm.

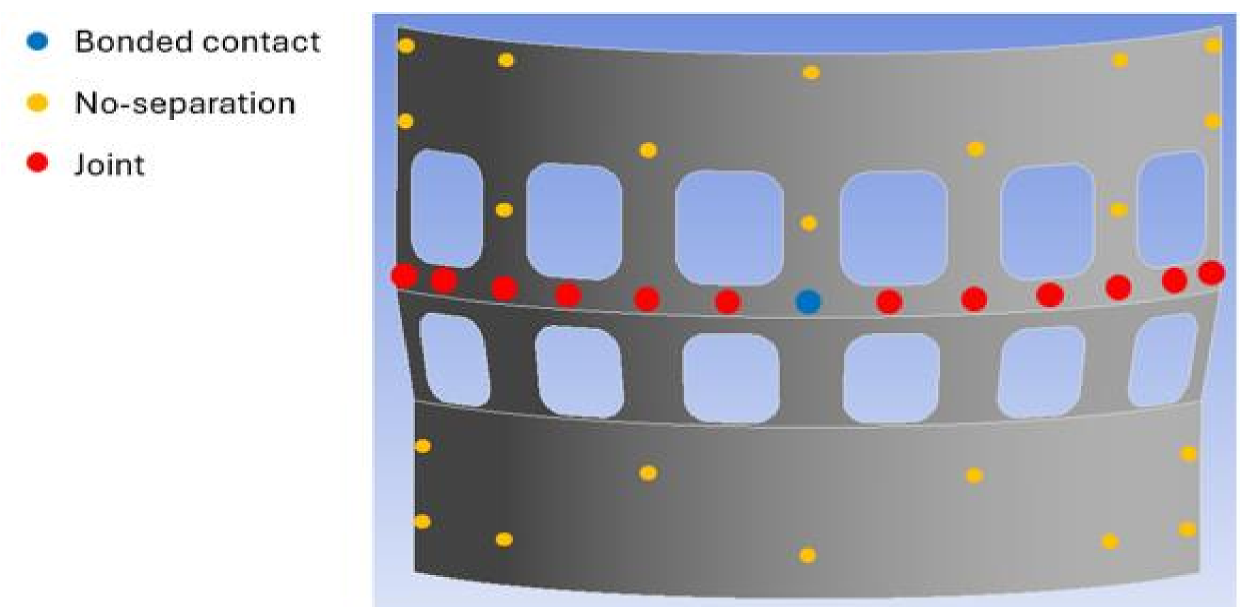

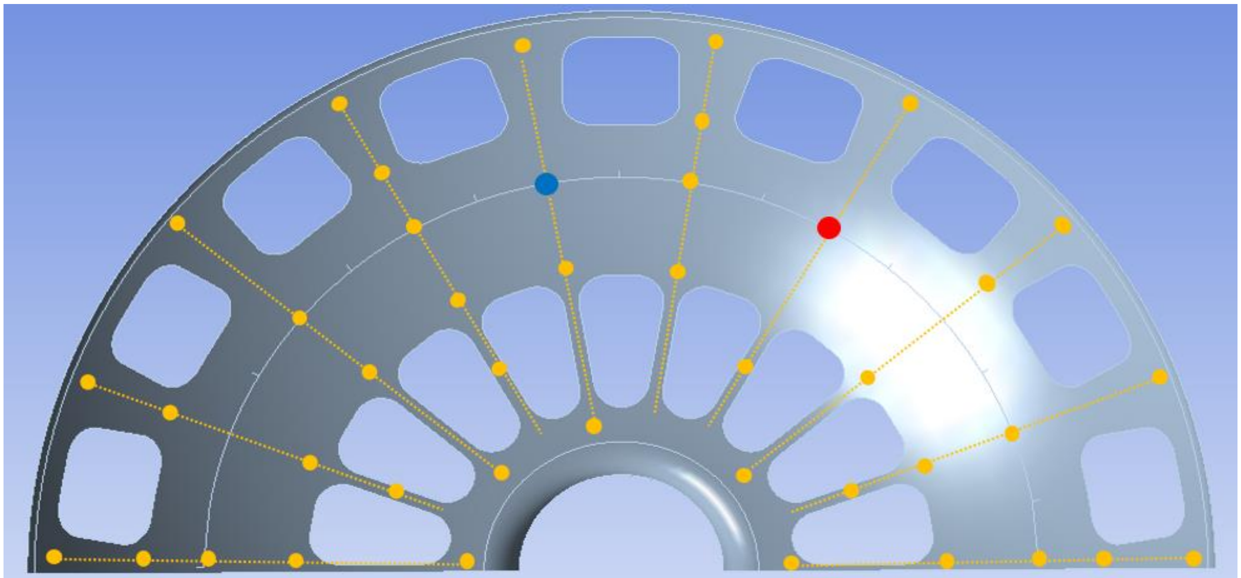

Figure 4.17 Mixed-diameter support configuration adopted for the sensitivity assessment.

The change in support diameter reduced the total support-member cross-sectional area. In the reference configuration, all 80 support members had a diameter of 20 mm, giving a total cross-sectional area of 25132.8 mm². In the mixed-diameter configuration, 15 support members were kept at 20 mm diameter and the remaining 65 support members were reduced to 10 mm diameter, giving a total cross-sectional area of 9817.5 mm². This corresponds to a 60.94% reduction in total support-member cross-sectional area.

Table 4.20 Total support-member cross-sectional area in the reference and mixed-diameter configurations.

Configuration	20 mm supports	10 mm supports	Total support-member cross-sectional area
Reference configuration	80	0	25132.8 mm²
Mixed-diameter configuration	15	65	9817.5 mm²

The comparison between the reference and mixed-diameter configurations is summarized in Table 4.20 for the main structural response quantities.

Table 4.21 Comparison between the reference and mixed-diameter support configurations.

Load case	Quantity	Reference configuration	Mixed-diameter configuration
Gravity	Cylindrical THS max. absolute vertical displacement	5.3877 mm	5.3909 mm
Gravity	Dome THS max. absolute vertical displacement	5.1703 mm	5.1835 mm
Gravity	Top-cover THS max. absolute vertical displacement	0.8154 mm	0.8334 mm
Gravity	Cylindrical THS max. equivalent stress	88.629 MPa	88.49 MPa
Gravity	Dome THS max. equivalent stress	99.496 MPa	99.643 MPa
Gravity	Top-cover THS max. equivalent stress	8.5226 MPa	8.8042 MPa
Gravity	Maximum support direct stress	+1.7959 MPa	+7.1313 MPa
Gravity	Maximum support combined stress	+234.11 MPa	+233.95 MPa
Gravity	Minimum support combined stress	−233.45 MPa	−233.3 MPa
Thermal	Cylindrical THS max. total deformation	18.91 mm	18.91 mm
Thermal	Dome THS max. total deformation	23.581 mm	23.58 mm
Thermal	Top-cover THS max. total deformation	3.0127 mm	3.0155 mm
Thermal	Cylindrical THS max. equivalent stress	1.4018 MPa	1.4015 MPa
Thermal	Dome THS max. equivalent stress	24.933 MPa	24.734 MPa
Thermal	Top-cover THS max. equivalent stress	3.9434 MPa	2.781 MPa
Thermal	Maximum support direct stress	+0.8441 MPa	+3.3421 MPa
Thermal	Maximum support combined stress	+17.869 MPa	+10.669 MPa
Thermal	Minimum support combined stress	−18.489 MPa	−11.882 MPa
Combined	Cylindrical THS max. total deformation	22.222 mm	22.226 mm
Combined	Dome THS max. total deformation	26.691 mm	26.682 mm
Combined	Top-cover THS max. total deformation	2.9054 mm	2.9013 mm
Combined	Cylindrical THS max. equivalent stress	93.64 MPa	93.501 MPa
Combined	Dome THS max. equivalent stress	96.993 MPa	97.124 MPa
Combined	Top-cover THS max. equivalent stress	11.123 MPa	9.9631 MPa
Combined	Maximum support direct stress	+1.6086 MPa	+6.4052 MPa
Combined	Maximum support combined stress	+236.49 MPa	+236.32 MPa
Combined	Minimum support combined stress	−236.2 MPa	−236.15 MPa

The mixed-diameter configuration produced nearly the same deformation pattern as the reference configuration. Under gravity loading, all thermal shield regions remained below the 10 mm deformation check. Under thermal and combined loading, the maximum total deformation values changed only slightly.

The support-member combined stresses changed only marginally relative to the reference configuration. Under gravity loading, the maximum combined stress changed from +234.11 MPa in the reference configuration to +233.95 MPa in the mixed-diameter configuration, while the minimum combined stress changed from −233.45 MPa to −233.3 MPa. Under combined gravity and thermal loading, the maximum combined stress changed from +236.49 MPa to +236.32 MPa, while the minimum combined stress changed from −236.2 MPa to −236.15 MPa. These differences are small, and the locations of maximum combined stress remained the same as in the reference configuration. This behavior indicates that, in the analyzed model, the maximum combined stresses were still governed mainly by the 20 mm supports kept at the most loaded locations. The reduced-diameter members showed a higher maximum direct stress, reaching +7.1313 MPa under gravity loading, because of their smaller cross-sectional area. However, they did not control the governing combined-stress response.

The largest shell stress in the mixed-diameter configuration was 99.643 MPa in the dome thermal shield under gravity loading. Under combined loading, the cylindrical thermal shield stress was practically unchanged compared with the reference configuration, changing from 93.64 MPa to 93.501 MPa. These values were lower than the selected 316LN reference strength used for the shell-stress check.

The gap-result comparison is summarized in Table 4.21. The initial gap fields are the same as those used for the reference configuration.

Table 4.22 Gap-result comparison for the mixed-diameter support configuration.

Load case	Cylindrical THS gap range	Dome THS gap range	Top-cover THS gap range
Initial	−142.58 to −300 mm	−91.349 to −170 mm	−92.176 to −102.27 mm
Gravity	−140.34 to −300 mm	−87.159 to −170 mm	−92.293 to −102.28 mm
Thermal	−142.48 to −300 mm	−96.577 to −170 mm	−94.476 to −104.72 mm
Combined	−140.53 to −300 mm	−92.902 to −170 mm	−94.589 to −104.73 mm

The gap-result fields did not show loss of insulation clearance in the mixed-diameter configuration. The first relevant positive gravity-prestressed eigenvalue buckling multiplier was 5.2835, compared with 5.2172 for the reference configuration. Under the same nonlinear-based perturbation interpretation used for the reference case, this corresponds to an estimated total buckling load state of approximately 6.28 times the gravity load. Therefore, the diameter reduction did not reduce the gravity-prestressed linear buckling estimate.

Overall, reducing the selected support diameters had little effect on the global structural response. The mixed-diameter configuration remained comparable to the reference case in deformation, combined beam stress, gap behavior, and eigenvalue buckling, while reducing the total support-member cross-sectional area by 60.94%. Based on the analyzed loading cases and the modeling assumptions adopted in this work, the mixed-diameter configuration can be considered structurally acceptable at the global model level.

Chapter 5

Conclusions and Future Work

5.1 Summary of the Work

This thesis assessed the global structural response of the DTT cryostat thermal shield support system using a finite element shell-and-beam model. The cryostat body and thermal shields were modeled with shell elements, while the G10-CR support members were represented by beam elements connected through bonded, joint-based, and no-separation interface definitions.

A reference configuration with 80 support members of 20 mm diameter was analyzed under gravity loading, prescribed thermal loading, and combined gravity and thermal loading. The assessment considered shell stress, support-member stress, deformation, insulation-gap preservation, and linear eigenvalue buckling.

A mixed-diameter configuration was then studied as a sensitivity case. In this configuration, 15 support members were kept at 20 mm diameter and 65 were reduced to 10 mm diameter, reducing the total support-member cross-sectional area by 60.94%.

5.2 Main Findings

The support-member stresses were governed mainly by gravity-induced bending. In the reference configuration, the largest combined stress occurred under combined gravity and thermal loading, reaching +236.49 MPa, with a corresponding minimum of −236.2 MPa. Direct axial stresses remained below 2 MPa, confirming that axial loading was not the controlling contribution.

Thermal loading mainly affected the displacement field. The thermal loading case produced larger deformations than the gravity loading case, especially in the cylindrical and dome thermal shields, but the associated shell and support-member stresses remained lower than the gravity and combined-loading values. Thus, thermal contraction influenced the overall deformation more than the governing stress levels.

The 10 mm gravity-only vertical deformation check was met for all thermal shield regions in the reference configuration. The maximum absolute vertical displacement was 5.3877 mm in the cylindrical thermal shield, 5.1703 mm in the dome thermal shield, and 0.8154 mm in the top-cover thermal shield.

The maximum shell stresses in the reference configuration were lower than the selected 316LN reference strength used for comparison. The highest shell stress occurred in the dome thermal shield under gravity loading, with a value of 99.496 MPa. The cylindrical thermal shield reached 93.64 MPa under combined gravity and thermal loading. The shell stress maxima were generally localized near the support connection regions where the main support reactions were introduced into the thin shell structures, particularly near the more restrained bonded connections.

The gap assessment did not suggest any loss of insulation clearance in the analyzed loading cases. The deformed gap fields remained close to the corresponding initial gap fields for the cylindrical, dome, and top-cover thermal shields.

The eigenvalue buckling assessment indicated that elastic buckling was not the governing limitation for the reference configuration within the adopted linear perturbation framework. The gravity-prestressed case corresponded to an estimated total buckling load state of approximately 6.22 times the reference gravity load. Supplementary thermal-perturbation checks also produced very high positive multipliers, supporting the conclusion that thermal-perturbation-driven elastic buckling was not close to the operating condition.

The mixed-diameter configuration gave results comparable to the reference case in terms of deformation, support-member combined stress, gap behavior, and eigenvalue buckling response. Under combined gravity and thermal loading, the maximum support-member combined stress changed only from +236.49 MPa to +236.32 MPa. Direct stresses increased in some reduced-diameter members because of their smaller cross-sectional area, but they remained much lower than the governing combined beam stresses. The first relevant positive gravity-prestressed eigenvalue buckling multiplier of the mixed-diameter configuration was 5.2835, showing no reduction relative to the reference value. Under the same nonlinear-based interpretation, this corresponds to an estimated total buckling load state of approximately 6.28 times the reference gravity load.

Under the modeling assumptions adopted in this work, both the reference and mixed-diameter configurations met the structural checks considered in the thesis. The mixed-diameter configuration therefore provides a substantial reduction in support-member cross-sectional area without significantly degrading the global structural behavior.

5.3 Limitations of the Study

The final support configuration was developed through engineering judgement and finite element assessment, not through a formal optimization procedure. Therefore, it should be considered an engineering-refined configuration, not a globally optimized support distribution.

The finite element model was developed to evaluate the global structural behavior of the cryostat thermal shield support system. It was not intended to provide detailed local verification of the support attachments. The support members were represented using beam elements connected to shell surfaces, and detailed bolted-joint geometry, washers, pads, local contact-pressure distributions, and attachment-region stresses were not explicitly modeled.

The finite element model was not formally validated against experimental measurements or an official benchmark model. The simplified hand calculation reported in Appendix A was used only as a preliminary sizing estimate and analytical cross-check for the cylindrical thermal shield gravity-deformation magnitude. Although the hand-calculated displacement was close to the corresponding finite element result, this comparison should not be interpreted as formal validation of the complete model. In addition, a formal mesh-convergence study was not performed; therefore, local peak stresses and contact-related quantities may be mesh-sensitive. The results are consequently most reliable for comparing the investigated configurations and identifying critical regions within the adopted global modeling assumptions.

The G10-CR support members were represented using an equivalent linear elastic beam material definition. The full orthotropic material behavior, laminate orientation, and detailed composite failure criteria were not included. For this reason, the stress analysis in the support members was interpreted as a beam-level strength comparison, rather than as a complete laminate-level failure verification.

The thermal loading was applied by prescribing temperatures directly in the structural model. A separate steady-state or transient heat-transfer analysis was not performed. Therefore, the thermal results represent the structural effect of the imposed temperature field, not the result of a coupled thermal analysis.

The buckling assessment was limited to linear eigenvalue buckling. The reported multipliers were interpreted within the nonlinear-based linear perturbation framework used by ANSYS. Therefore, the gravity-prestressed multiplier was treated as a multiplier of the retained gravity perturbation load, while the thermal-only and combined gravity–thermal restart results were treated as multipliers of an imposed unit thermal perturbation. These results should not be interpreted as nonlinear collapse loads, complete post-buckling safety factors, or direct critical-temperature predictions. Geometric imperfections, contact-status changes during buckling, material nonlinearity, and nonlinear post-buckling behavior were not included.

5.4 Future Work

Future work should first include a formal parametric or topology-optimization study of the support locations, support diameters, and support orientations to identify globally optimized configurations under gravity, thermal, combined loading, and buckling constraints.

The local behavior of the support attachments could also be investigated. A detailed solid or sub-modeling approach could include the actual attachment geometry, local contact regions, and load-transfer paths between the support members and the shell structures. This would allow the stress fields at the support connection regions to be assessed with higher local resolution.

The representation of the G10-CR support members could also be improved by introducing orthotropic elastic properties, material orientation, and laminate-level failure criteria. This would extend the support assessment beyond the equivalent beam-level stress comparison used in this thesis.

Future work should include a formal numerical verification and validation procedure. This should include a mesh-convergence study for the main displacement, stress, contact-gap, and support-force quantities, followed by comparison with experimental measurements, detailed sub-models, or official benchmark results if available. Such work would allow the global shell-and-beam model to be upgraded from a comparative design-assessment model to a more fully verified design-support model.

Future work should extend the stability assessment through nonlinear geometric buckling analyses including representative geometric imperfections and possible contact-status changes. Such analyses would provide a more realistic estimate of post-buckling behavior and collapse margins than the linear eigenvalue buckling checks used in the present work.

A further development would be the inclusion of steady-state or transient heat-transfer analysis. A coupled or sequential thermo-mechanical approach would allow the structural response to be evaluated using temperature fields obtained from a thermal model instead of prescribed uniform temperatures.

Finally, the same modeling strategy could be applied to future fusion reactor thermal shield support systems, including DEMO-class concepts, where the balance between structural stiffness, thermal contraction accommodation, support cross-section, and insulation-gap preservation remains a central design issue.

5.5 Final Conclusion

The finite element analyses showed that the global shell-and-beam model provides a suitable basis for assessing the main structural response of the DTT cryostat thermal shield support system. The reference configuration met the deformation, stress, gap, and linear buckling checks considered in this work. The mixed-diameter configuration produced comparable global behavior while reducing the total support-member cross-sectional area by approximately 61%. Within the analyzed loading cases and the assumptions of the global shell-and-beam model, the mixed-diameter configuration can therefore be considered a structurally promising alternative for further detailed verification.

Appendix A:

Preliminary Sizing Estimate for Cylindrical Thermal Shield Supports

A preliminary hand calculation was performed to estimate the number of weight-bearing support members required for the cylindrical thermal shield. The purpose of this calculation was not to provide final strength verification, but to obtain an initial support configuration for the finite element model.

In this estimate, the cylindrical thermal shield weight was assumed to be distributed equally among the candidate vertical support locations. Each support member was idealized as a cantilever-type member subjected to the corresponding transverse load. The calculation did not include shell flexibility, contact behavior, joint constraints, local support-interface effects, or interaction between neighboring supports. These effects were evaluated later using the finite element model. The input quantities used in the preliminary estimate are summarized in Table A.1.

Table A.1 Input quantities used for the preliminary sizing estimate of the cylindrical thermal shield supports.

Quantity	Symbol	Value
Cylindrical thermal shield mass	m	1392.7 kg
Gravitational acceleration	g	9.81 m/s²
Cylindrical thermal shield weight	W	13662.4 N
Number of candidate support locations	n	13
Load per support	F = W/n	1050.95 N
Support length	L	147.5 mm
Support diameter	d	20 mm
Cross-sectional area	A	314.16 mm²
Second moment of area	I	7853.98 mm⁴
Young's modulus of G10-CR used in the estimate	E	28000 MPa

For a circular support member, the cross-sectional area and second moment of area were calculated as:

$$A = \frac{\pi d^2}{4}$$

$$I = \frac{\pi d^4}{64}$$

The maximum bending moment was estimated from:

$$M = FL$$

Using the load per support and the support length, the resulting moment was:

$$M = 1050.95 \times 147.5 = 155015\ \mathrm{N \cdot mm} = 155.02\ \mathrm{N \cdot m}$$

The maximum bending stress was estimated from:

$$\sigma_b = \frac{Mc}{I}$$

where $c = \frac{d}{2}$. This gave:

$$\sigma_b = 197.47\ \mathrm{MPa}$$

The maximum shear stress for the circular section was estimated using:

$$\tau_{max} = \frac{4F}{3A}$$

which gave:

$$\tau_{max} = 4.46\ \mathrm{MPa}$$

The tip displacement of the idealized support member was estimated as:

$$\delta = \frac{FL^3}{3EI}$$

which gave:

$$\delta = 5.11\ \mathrm{mm}$$

The calculated results are summarized in Table A.2.

Table A.2 Preliminary hand-calculation results for the cylindrical thermal shield supports.

Calculated quantity	Symbol	Value
Load per support	F	1050.95 N
Maximum bending moment	M	155.02 N·m
Maximum bending stress	σ_b	197.47 MPa
Maximum shear stress	τ_{max}	4.46 MPa
Estimated tip displacement	δ	5.11 mm

The estimated displacement was below the 10 mm gravity-only deformation check used in this work. Therefore, the preliminary calculation indicated that 13 weight-supporting locations with 20 mm diameter support members could be used as an initial configuration for the finite element model. The final support reactions, stresses, deformations, and gap behavior were not taken from this hand calculation. They were obtained from the finite element analyses presented in Chapter 4.

The calculated displacement was later compared with the finite element gravity-deformation result for the cylindrical thermal shield, as discussed in Section 4.6.3. This comparison was used only as an analytical cross-check of the deformation magnitude and was not treated as formal validation of the finite element model.

Appendix B:

Initial Gap Fields Used for the Insulation-Gap Assessment

The insulation-gap assessment in this work was based on a comparison between the initial and deformed gap fields. Before applying the structural loads, the initial gap field was extracted from the frictionless contact interfaces defined between the cryostat body and the thermal shields. These initial fields were then used as reference distributions for the gravity, thermal, and combined loading cases. The initial gap fields are shown in Figure B.1.

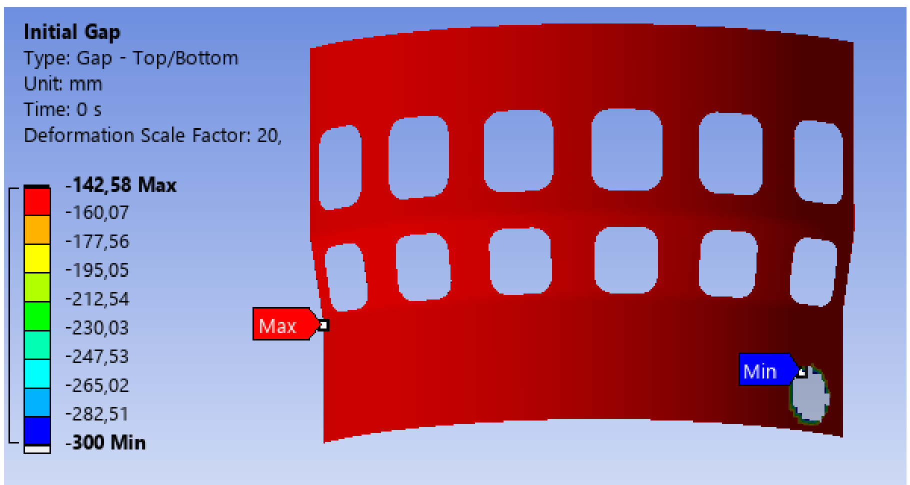

(a)

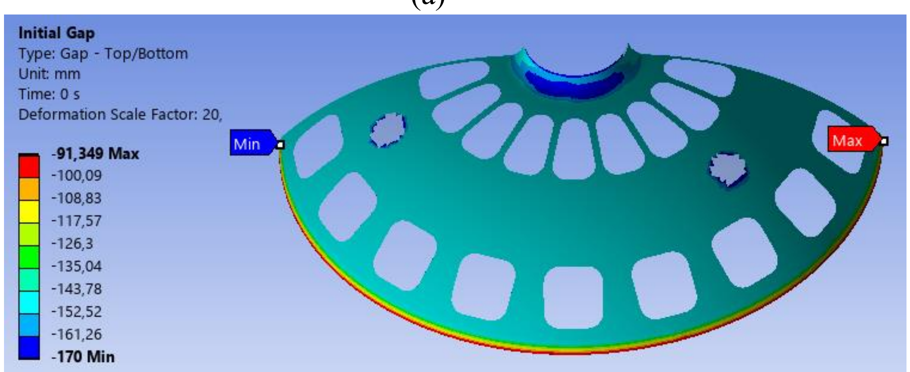

(b)

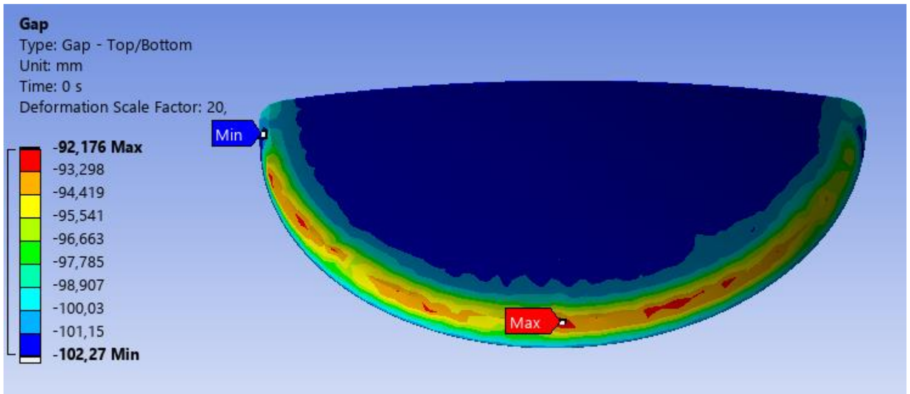

(c)

Figure B.1 Initial gap fields used as reference for the insulation-gap assessment: (a) cylindrical thermal shield, (b) dome thermal shield, and (c) top-cover thermal shield.

The corresponding initial gap-result ranges are summarized in Table B.1.

Table B.1 Initial gap-result ranges used for the insulation-gap assessment.

Thermal shield region	**Initial gap-result range**
Cylindrical thermal shield	−142.58 to −300 mm
Dome thermal shield	−91.349 to −170 mm
Top-cover thermal shield	−92.176 to −102.27 mm

These initial gap-result fields were not reduced to a single average clearance value. Instead, the deformed gap field from each loading case was compared with the corresponding initial field in order to evaluate the change in available clearance over the modeled contact regions.

Bibliography

[1] M. Shimada *et al.*, “Chapter 1: Overview and summary,” *Nuclear Fusion*, vol. 47, no. 6, pp. S1–S17, Jun. 2007, doi: 10.1088/0029-5515/47/6/S01.

[2] S. Nakamura *et al.*, “Design and manufacturing of thermal shield for JT-60SA,” *Fusion Engineering and Design*, vol. 146, pp. 2375–2378, 2019, doi: 10.1016/j.fusengdes.2019.03.194.

[3] G. Barone, S. Roccella, E. Martelli, and E. Visca, “DTT Thermal Shield: Preliminary thermal analysis,” *Fusion Engineering and Design*, vol. 158, p. 111725, 2020, doi: 10.1016/j.fusengdes.2020.111725.

[4] C. H. Noh *et al.*, “Final design of ITER vacuum vessel thermal shield,” *Fusion Engineering and Design*, vol. 88, no. 9–10, pp. 1896–1899, 2013, doi: 10.1016/j.fusengdes.2013.02.063.

[5] X. Han and L. Ziying, “Design and Analysis of the Thermal Shield of EAST Tokamak,” *Plasma Science and Technology*, vol. 10, no. 2, p. 227, 2008, doi: 10.1088/1009-0630/10/2/18.

[6] M. Nagel, S. Freundt, and H. Posselt, “Thermal and mechanical analysis of Wendelstein 7-X thermal shield,” *Fusion Engineering and Design*, vol. 86, no. 9–11, pp. 1830–1833, 2011, doi: 10.1016/j.fusengdes.2011.01.017.

[7] G. H. Kim *et al.*, “KSTAR thermal shield,” *Fusion Engineering and Design*, vol. 84, no. 2–6, pp. 1043–1048, Jun. 2009, doi: 10.1016/J.FUSENGDES.2008.11.047.

[8] R. Ambrosino, “DTT - Divertor Tokamak Test facility: A testbed for DEMO,” *Fusion Engineering and Design*, vol. 167, 2021, doi: 10.1016/j.fusengdes.2021.112330.

[9] R. Martone, R. Albanese, F. Crisanti, P. Martin, and A. Pizzuto, “DTT. Divertor Tokamak Test facility. Interim Design Report,” 2019, *ENEA, Frascati, Italy*.

[10] F. Maviglia, R. De Luca, S. Roccella, G. Maddaluno, G. Ramogida, and E. Visca, “Thermal-hydraulic analysis for first wall and thermal shield of Divertor Tokamak test facility,” *Fusion Engineering and Design*, vol. 146, pp. 2222–2226, 2019, doi: 10.1016/j.fusengdes.2019.03.157.

[11] V. Bykov *et al.*, “The ITER thermal shields for the magnet system: Design evolution and analysis,” *Fusion Engineering and Design*, vol. 75–79, no. SUPPL., pp. 155–162, Nov. 2005, doi: 10.1016/J.FUSENGDES.2005.08.013.

[12] Y. Krasikov *et al.*, "The ITER thermal shields for the magnet system: specific design, assembly and structural issues," *Fusion Engineering and Design*, vol. 66–68, pp. 1049–1054, 2003, doi: 10.1016/s0920-3796(03)00271-0.

[13] B. Končar, O. Costa Garrido, M. Draksler, R. Brown, and M. Coleman, "Initial optimization of DEMO fusion reactor thermal shields by thermal analysis of its integrated systems," *Fusion Engineering and Design*, vol. 125, pp. 38–49, 2017, doi: 10.1016/j.fusengdes.2017.10.017.

[14] B. Končar, M. Draksler, R. Brown, and C. Bachmann, "Heat Loads and Design Temperature Optimization of DEMO Thermal Shields," EUROfusion project reference: WPPMI-CPR (17) 17578, 2017.

[15] S. Garitta *et al.*, "Thermal and structural analysis of JT-60SA actively cooled divertor target submitted to high heat flux," *Fusion Engineering and Design*, vol. 199, p. 114133, Feb. 2024, doi: 10.1016/J.FUSENGDES.2023.114133.

[16] M. Zhang, H. Zhong, Y. Ren, D. Wang, and X. Gao, "Thermal analysis of the EAST tokamak," *Fusion Engineering and Design*, vol. 168, p. 112352, Jul. 2021, doi: 10.1016/J.FUSENGDES.2021.112352.

[17] S. Del Nero, M. Fulici, G. Barone, R. Bonifetto, M. Dalla Palma, and P. Fanelli, "Thermo-mechanical analysis of DTT Vacuum Vessel Thermal Shield," *Fusion Engineering and Design*, vol. 216, 2025, doi: 10.1016/j.fusengdes.2025.115090.

[18] E. Pompa *et al.*, "Validation of vacuum vessel thermal shield deformation via finite elements and morphing techniques based analysis," *Fusion Engineering and Design*, vol. 215, p. 114937, Jun. 2025, doi: 10.1016/J.FUSENGDES.2025.114937.

[19] C. H. Noh *et al.*, "Structural Analysis of the ITER Thermal Shield for Final Design Verification," *IEEE Transactions on Plasma Science*, vol. 42, no. 6, pp. 1770–1774, 2014, doi: 10.1109/TPS.2014.2321173.

[20] V. Bykov *et al.*, "The thermal shields for the ITER magnet system: thermal, structural and assembly aspects," *Fusion Engineering and Design*, vol. 58–59, pp. 177–182, Nov. 2001, doi: 10.1016/S0920-3796(01)00427-6.

[21] K. Nam *et al.*, "Thermal analysis on detailed 3D models of ITER thermal shield," *Fusion Engineering and Design*, vol. 89, no. 7–8, pp. 1843–1847, Oct. 2014, doi: 10.1016/J.FUSENGDES.2014.02.060.

[22] N. Her *et al.*, "Progress of the ITER Thermal Shields," *Fusion Engineering and Design*, vol. 109–111, pp. 937–941, Nov. 2016, doi: 10.1016/J.FUSENGDES.2016.01.050.

[23] M. B. Kasen, G. R. MacDonald, D. H. Beekman, Jr., and R. E. Schramm, "Mechanical, electrical, and thermal characterization of G-10CR and G-11CR glass-cloth/epoxy laminates between room temperature and 4 K," in *Advances in Cryogenic Engineering Materials*, R. P. Reed and A. F. Clark, Eds., Boston, MA, USA: Springer, 1980, pp. 235–244. doi: 10.1007/978-1-4613-9859-2_24.

[24] ITER Organization, "Appendix A: Materials Design Limit Data," ITER Structural Design Criteria for In-Vessel Components (SDC-IC), Version 3.3, External Ref. G 74 MA 8 01-05-28 W0.2, Saint-Paul-lez-Durance, France, 2013.

[25] J. Sas, K.-P. Weiss, and A. Jung, "The Mechanical and material properties of 316LN austenitic stainless steel for the fusion application in cryogenic temperatures," *IOP Conf. Ser. Mater. Sci. Eng.*, vol. 102, p. 012003, Dec. 2015, doi: 10.1088/1757-899X/102/1/012003.

[26] J. H. Kim and J. Feng, "The 4 K mechanical properties of modified SS316LN for jacket materials in superconducting fusion magnets," *AIP Conf. Proc.*, vol. 986, no. 1, pp. 92–99, Mar. 2008, doi: 10.1063/1.2900401.

[27] L. F. Li, Y. T. Zhang, and Y. Y. Li, "Chapter 210 - Development of cryogenic structural materials," in *Proceedings of the Twentieth International Cryogenic Engineering Conference (ICEC20)*, L. Zhang, L. Lin, and G. Chen, Eds., Oxford: Elsevier Science, 2005, pp. 885–894. doi: 10.1016/B978-008044559-5/50213-1.

[28] Y. Shindo, K. Horiguchi, and R. Wang, "Cryomechanics and Short-Beam Interlaminar Shear Strength of G-10CR Glass-Cloth/Epoxy Laminates," 2000, pp. 167–174. doi: 10.1007/978-1-4615-4293-3_21.

[29] ANSYS, Inc., "SHELL181," Ansys Mechanical APDL Element Reference, Release 2025 R2. [Online]. Available: https://ansyshelp.ansys.com/public/Views/Secured/corp/v252/en/ans_elem/Hlp_E_SHELL181.html. Accessed: Jun. 20, 2026.

[30] E. Oñate, *Structural Analysis with the Finite Element Method: Linear Statics: Beams, Plates and Shells*, vol. 2. Dordrecht: Springer, 2013.

[31] ANSYS, Inc., "BEAM188," Ansys Mechanical APDL Element Reference, Release 2025 R2. [Online]. Available:

https://ansyshelp.ansys.com/public/Views/Secured/corp/v252/en/ans_elem/Hlp_E_BEAM188.html. Accessed: Jun. 20, 2026.

[32] G. Zavarise, P. Wriggers, and U. Nackenhorst, *A Guide for Engineers to Computational Contact Mechanics*. Hannover: The TCN Series on Simulation Based Engineering and Science, 2006.

[33] O. C. Zienkiewicz and R. L. Taylor, *The Finite Element Method: Solid Mechanics*, 5th ed., vol. 2. Oxford: Butterworth-Heinemann, 2000.

[34] Acculam, "Acculam® Epoxyglas G10 / CR," product data sheet, n.d. [Online]. Available: https://acculam.com/images/ecommerce/Product/Files/Acculam-Epoxyglas-G10-CR-Data-Sheet.pdf. Accessed: Jun. 10, 2026.

[35] ANSYS, Inc., "Eigenvalue Buckling Analysis," Ansys Mechanical User's Guide, Release 2025 R2. [Online]. Available: https://ansyshelp.ansys.com/public/Views/Secured/corp/v252/en/wb_sim/ds_buckling_analysis_type.html. Accessed: Jun. 20, 2026.

[36] ANSYS, Inc., "Considerations for Load Generation and Controls," Ansys Mechanical APDL Structural Analysis Guide, Release 2025 R2. [Online]. Available: https://ansyshelp.ansys.com/public/Views/Secured/corp/v252/en/ans_str/strlinpertload.html. Accessed: Jun. 20, 2026.

[37] V. Birman, "Plates and Shells," 2010. doi: 10.1002/9780470686652.eae141.